UNCLASSIFIED

AD NUMBER
AD881994
LIMITATION CHANGES

TO:

Approved for public release; distribution is unlimited.

FROM:

Distribution authorized to U.S. Gov't. agencies and their contractors; Critical Technology; JAN 1971. Other requests shall be referred to Air Force Rocket Propulsion Laboratory, Attn: DOG/STINFO, Edwards, GA 93523. This document contains export-controlled technical data.

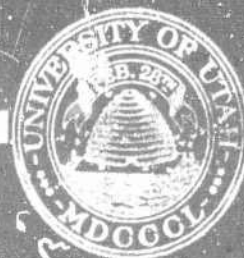| AUTHORITY |
| --- |
| afrpl ltr, 1 feb 1973 |

THIS PAGE IS UNCLASSIFIED

THE STUDY OF CRACK CRITICALITY

IN

SOLID ROCKET MOTORS

Final Report
Submitted to the

Air Force Rocket Propulsion Laboratory
Contract #FO 4611-70-C-0006

AFRPL TR 71-21
January 1971   UTEC DO 71-041

COLLEGE OF ENGINEERING

UNIVERSITY OF UTAH

SALT LAKE CITY, UTAH 84112.

THE STUDY OF CRACK CRITICALITY

IN

SOLID ROCKET MOTORS

Final Report
Submitted to the

Air Force Rocket Propulsion Laboratory
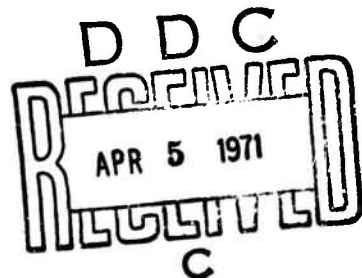Contract #FO 4611-70-C-0006 *NEW*

January 1971

AFRPL TR 71-21
UTEC DO 71-041

Principal Investigators
M. L. Williams
H. R. Jacobs

Associate Investigators
G. A. Flandro
R. J. Nuismer

Graduate Research Assistant
T. C. Derbidge

TABLE OF CONTENTS

I. INTRODUCTION

The existence of flaws in solid propellant grains is a problem that has plagued the solid rocket motor industry for a considerable time.[1,2,3] Flaws may exist in the grain due to unsteady processes during casting, difficulties in curing, problems in humidity and temperature control, etc. The surveillance programs that have been under way for several years indicate that flaws may form due to "aging."[4]

The Air Force Rocket Propulsion Laboratory at its own laboratory and through its contractors has carried out numerous investigations[5,6,7] dealing with the problem of initiation of burning within flaws in solid propellant grains. Similar studies have been carried out in Japan[8] and the United Kingdom.[9] The tests conducted by AFRPL and its contractors primarily dealt with ignition times and rates of propagation of the flames into "manufactured cracks" although tests were conducted at Thiokol's Utah Division in which the fracture was obtained by tearing the propellant. The tests conducted in Japan were also conducted with manufactured cracks. The United Kingdom tests conducted at the Explosive Research Development Establishment were tests in small scale rocket motors with manufactured cracks and debonds.

Tests have been conducted at Thiokol, Utah Division[6] and at the Naval Weapons Center, China Lake[10] dealing with debonds. These tests were all conducted utilizing a "half-motor." The "half-motors" were half of a solid propellant motor and a block of plexiglas joined together to allow visual observation of the burning processes. Similar unpublished tests have been conducted by H. R. Jacobs at the University of Utah.[11]

All of the above mentioned tests dealing with burning in cracks and debonds indicated overwhelming statistical evidence that burning would propagate into cracks and debonds and that the propagation rates increased with the external or chamber pressure. In some of the half-motor tests catastrophic failure occurred.[10]

The present study, which was the result of an unsolicited proposal, had as its primary objective the determination of whether the pressures which develop in burning flaws, cracks and debonds are sufficient to cause the defect to propagate due to mechanical failure of the propellant.

The University of Utah in its investigation was directed to assume that the defect surface was ignited. With this assumption, it was further assumed that the size, shape and nature of the initial defect were known.

In order to carry out the proposed study a qualitative investigation of the governing parameters was first conducted. The critical parameters are, in addition to propellant characteristics, main chamber pressure and defect geometry, the main chamber gas velocity, the gas velocity within the defect, the burning rate of the wall, and the fracture propagation velocity.

If the burning rate of the material is greater than the crack propagation velocity, the defect tip will be "burned out" before it can be propagated due to mechanical failure. If the surface burning of the defect area is large compared to its cross-sectional area at its exit plane, then the velocity of the burned gaseous effluent will in general be larger than that external to the defect and there will be no net flow into the defect but only a flow-out. The most important flow is that of the effluent gases, for it is this velocity which determines the pressure field within the flaw. For most solid propellants the combustion rate is pressure dependent. The stress field around the defect is also dependent upon the pressure, and hence, the presence of "cracking" and its propagation speed.

The pressure distribution in a burning defect will vary with time because the defect geometry is being continually changed by burning at the walls. In addition cracking, if it occurs, will alter the geometry and thus change thepressure distribution. Despite these facts, a true transient analysis is not necessary if the geometry change is slow compared to the velocity of the combustion products within the flaw. In general, the propellant burning rate is on the order of 10^{-1} fps while that of the gas velocity is on the order of 10^2 fps; therefore, in regard

-2-

to the burning wall, a quasi-steady analysis is justifiable. The quasi-steady analysis as related to crack propagation speed is reasonable if the crack propagation velocity is either much slower than the gas velocity or if the defect remains stable for a length of time and then propagates to a new stable geometry which is instantaneously ignited. With these facts in mind, the current study has limited the gas phase study to a quasi-steady analysis to determine the instantaneous pressure distribution in a burning defect in a solid propellant grain.

Primarily, the analyses to determine pressure distributions have been limited to one dimensional analyses. These analyses are applicable primarily to flaws with large burning surface area compared to the exit flow area.

A two-dimensional analysis was carried out to determine the effect of two dimensions on triangular cracks with small angles of divergence. The results of this analysis which have been included in Section II justifies the one-dimensional assumption.

A parametric study was conducted to determine the effects of geometry and fuel characteristics on pressures within cracks and debonds (burning on one side of the crack only) and is reported in Section III. Also included in this section is a study indicating typical times required for the pressure at the crack tip to decrease by a factor of two and indications of crack geometry changes with time.

Section IV of the report summarizes the work for cracks in pressurized cylinders conducted to determine criticality conditions by the use of time-dependent stress intensity factors. Methods of determining times to failure for a pressurized crack and means of determining initial crack propagation velocities through the use of a thermodynamic power balance are also included.

Section V compares crack propagation velocity estimates to the propellant burning rate for TPH-1011 and estimates of times to failure, while Section VI summarizes the conclusions of this program.

II. DETERMINATION OF PRESSURE DISTRIBUTION
IN BURNING FLAWS, CRACKS AND DEBONDS

ONE-DIMENSIONAL ANALYSIS INCLUDING FRICTION

The relations governing the state of the flow are independent of geometry and are stated below:

Equation of State	P	$= \rho RT$	(1)
Energy	$h + u^2/2$	$= h_o$	(2)
Heat Capacity	$h - h_r$	$= C_p T$	(3)

In the energy equation it is assumed that the mass addition is accomplished at constant enthalpy and negligible kinetic energy. This a reasonable assumption for a burning surface if the combustion zone is assumed infinitely thin and at the surface. It is also assumed that the flow is adiabatic. The latter is a good assumption for solid propellant grains which release considerable energy and are notably poor conductors. The specific heat and viscosity are assumed constant, implying that no chemical reaction takes place after the gas is added to the stream.

The one-dimensional momentum equation is

$$\frac{1}{2} P \frac{dS}{dx} \frac{dy}{dx} - \frac{d}{dx}(AP) - \tau_{wb} \frac{dS_b}{dx} - \tau_{wn} \frac{dS_n}{dx} = \frac{d}{dx}(\dot{m} u) \qquad (4)$$

The change of y with x, dy/dx, is assumed small to insure one-dimensionality and since normal burning is assumed the x component of momentum of the small mass, $\dot{dm}$, added over the length dx, is negligibly small. The variation of flow area, A, and differential surface area, dS, with x, is of the form

$$A \sim y(x)x^\ell \qquad (5a)$$

$$dS \sim x^\ell dx \qquad (5b)$$

where the exponent ℓ may assume the values 0 or 1.0 depending on how the channel depth varies with x. To elucidate this point consider the conical shaped duct illustrated in Figure 1.

Top-View-   Cross-sectional View
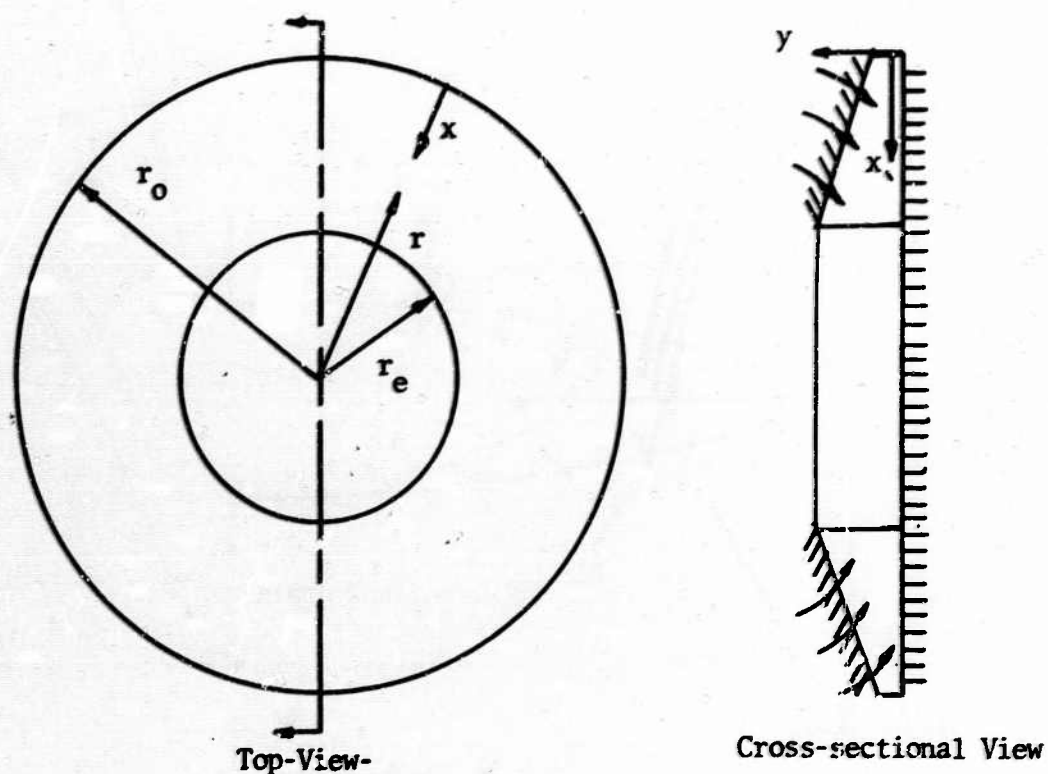
Figure 1. Conical duct

The area at any r, is given by-

$$A = 2\pi y r \qquad (6a)$$

where

$$r = r_o - x \qquad (6b)$$

and; therefore, this geometry corresponds to $\ell = 1$.

Three types of geometries, which appear frequently in application and to which Equation 4 applies are illustrated in Figure 2.

The geometry labeled "crack" represents a one-dimensional model of a deep flaw within the propellant grain itself. The debond geometry is the one-dimensional model of a separation between the propellant grain and the

-5-
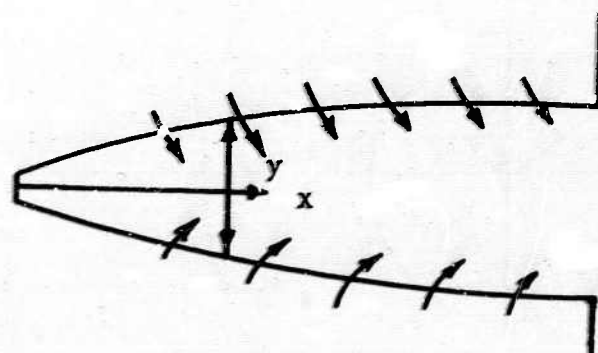
Crack in Propellant Grain
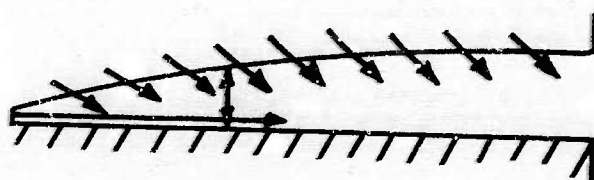
Debond of Grain from Casing
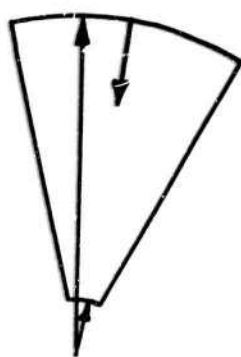
Circular Debond at Grain Head End

Figure 2.   Three flaw types which appear frequently in application

cylindrical portion of the casing, while the circular debond is the model
of a similar separation between the grain and the hemispherical bulkhead of
the casing.

Observation of Figure 2 yields the following specific forms for A and dS

Crack $A = y$

                  $dS_n = 0$

                  $dS_b = 2dx$

Debond $A = y$ (7)

                  $dS_b = dS_n = dx$

Circular Debond $A = 2\pi y(r_o - x)$

                  $dS_b = dS_n = 2\pi(r_o - x)dx$

The fact that surface area, dS, may be directly related to distance along the
flaw, dx, follows from the assumption that dy/dx is small.

The general momentum equation contains wall shear stress terms which
must be related to more readily measurable quantities. Two types of wall
shear stress are encountered; shear at a burning wall, τ_{wb}, and shear at
a non-burning wall, τ_{wn}. Both types of wall shear stress are assumed to
be approximated by a relation of the form

$$\tau_w = \frac{1}{2} f\rho u^2 \tag{8}$$

The friction factor, f, for the non-burning wall is solely a function of
Reynold's number. The friction factor, f_b, for the burning wall is dependent
both on Reynold's number and the mass addition rate since this mass addition
tends to "blow" the boundary layer away from the wall and thus reduce wall
shear stress. Reference 12 has reported a correlation between friction factor
for external flow with pressure gradient and non-dimensional blowing rate,
B_r, where

-7-

$$B_r = \frac{\rho_W V_W}{\rho_s u_s} \sqrt{Re_x} \tag{9}$$

and Re_x is the Reynold's number based upon the distance, x, from the leading edge. In the problem at hand, which more closely resembles pipe flow than boundary layer flow, it is more reasonable to base the Reynold's number on the local hydraulic diameter.

For a parallel slot the characteristic length used is the crack (or debond) height, y.

$$R_e = \frac{2yu\rho}{\mu} \tag{10}$$

Since the problem under consideration is one-dimensional $\rho_W = \rho_s = \rho$ and the normal velocity at the wall, V_W, can be evaluated by considering a differential wall length dx, in which case one has

$$d\dot{m} = \rho V_W \, dx \tag{11}$$

Utilizing the above relation in Equation 9 one obtains

$$B_r = \frac{1}{\rho u} \cdot \frac{d\dot{m}}{dx} \sqrt{R_e} \tag{12}$$

The correlation of Reference 12 may be approximated to obtain a friction factor with mass addition of the form

$$f_b = H f \tag{13a}$$

where

$$H \approx \frac{1}{2} \left[\frac{1}{B_r + 1.0} + \frac{1}{5^{B_r/4}} \right] \tag{13b}$$

Equations 8, 13a, and 13b determine the wall shear stress on both burning and non-burning walls once the functional relationship between the friction

-8-

factor, f, and the Reynolds number, R_e, is obtained This functional relation is of two basic types depending on whether the flow is laminar or turbulent. For laminar flow the relation is

$$f = \frac{96}{R_e} \tag{14a}$$

and for turbulent flow

$$f = \frac{0.316}{R_e^{1/4}} \tag{14b}$$

Substituting Equations 7, 8, and 13a into the general momentum equation, one obtains the specific momentum equations for the geometries of Figure 2 as

$$\text{Crack} \qquad y\frac{dP}{dx} - f\rho u^2 H = \frac{d}{dx}(\dot{m}\,u)\,) \tag{15a}$$

$$\text{Debond} \qquad y\frac{dP}{dx} - f\rho u^2 \frac{1+H}{2} = \frac{d}{dx}(\dot{m}\,u) \tag{15b}$$

$$\begin{array}{l}\text{Circular} \\ \text{Debond}\end{array} \qquad 2\pi r\left[P\frac{dy}{dx} - \frac{d}{dx}(ryP) - f\rho u^2 \frac{1+H}{2}\right] = \frac{d}{dx}(\dot{m}\,u) \tag{15c}$$

where f and H are determined by Equations 12, 13b, 14a and 14b. Notice that the momentum equation for the circular debond Equation 15c reduces to the same equation as that for the debond Equation 15b if one evaluates the limit as, $r \to \infty$.

One other equation determines the motion of the flow; this is the continuity equation

$$\dot{m} = \rho u A \tag{16}$$

For any given geometry there are two equations of motion and three equations of energy and state. These equations are expressed in terms of seven variables h, T, y, u, P, ρ and $\dot{m}$. Since there are five equations and seven variables, it is possible to express any one parameter as a function of any other two.

In general, experimental data are available to describe the burning rate

of the material. Since all mass flow in the flaw is due to the burning
rate which, in general, is dependent on the pressure, and since the original
geometry of the flaw is a known function of x, it is possible to express
P as a function of $\dot{m}$ and y. The simultaneous solution of the governing
equations is initiated by using the perfect gas relation Equation 1, the
property relation Equation 3 and the continuity relation Equation 16 to
eliminate ρ, u, and h from the momentum and energy equation yielding

$$\frac{1}{2}\bar{P}y'\ (S_n' + S_b') - \frac{d}{dx}(A\bar{P}) - \frac{f}{2\bar{P}}\ T\eta^2 R(S_n' + HS_b') = \frac{d}{dx}(\frac{A}{\bar{P}}\ T\eta^2 R) \quad (17a)$$

$$(\gamma - 1)(T\eta^2 R)^2 + (2\bar{P}^2\gamma)(T\eta^2 R) - 2T_o\ \bar{P}^2\gamma\ n^2 R = 0 \quad (17b)$$

(the prime denotes differentiation with respect to x)

where

$$\bar{P} = P/P_r \quad \text{and} \quad \eta = \dot{m}/P_r A.$$

P_r is a referenced pressure and may be picked at any desired value.
Equation (17b) is now solved for $T\eta^2 R$ by the quadratic formula to obtain

$$T\eta^2 R = \frac{-\bar{P}^2\gamma \pm \bar{P}\gamma(\bar{P}^2 + G^2\eta^2)^{\frac{1}{2}}}{\gamma - 1} \quad (18)$$

where $G = 2(\gamma - 1)T_oR/\gamma$ is a constant parameter of the propellant. Price[13]
has shown that of the two alternate signs only the plus sign has physical
meaning since the minus sign corresponds to removal of mass in an unmixing
process which leads to a decrease in entropy. He further defined the radical
as a new variable

$$\zeta = (\bar{P}^2 + G^2\eta^2)^{\frac{1}{2}}$$

Equation 18 is now combined with Equation 17a and rearranged to obtain

$$\frac{d\bar{P}}{dx} = \frac{\gamma\zeta}{A(\zeta - \gamma\bar{P})}\left\{ \frac{(\gamma - 1)\bar{P}}{\gamma}\left[A' - \frac{\gamma}{2}(S_n' + S_b')\right] \right.$$

$$\left. + (\zeta - \bar{P})\left[\frac{f}{2}\ (S_n' + HS_b') + A'\right] + \frac{AG^2\eta\eta'}{\zeta} \right\} \quad (19)$$

-10-

To proceed further a mass addition mechanism must be postulated. If errosive burning is neglected the combustion rate, r_b, of a solid propellant may be assumed to follow the empirical relation

$$r_b = CP^n \tag{20}$$

where r_b is the recession rate of the burning wall and C and n are constants to be determined empirically for a particular fuel. The local differential mass flux is then $d\dot{m} = Dr_b dS_b$, where D is the density of the solid. The local mass flux may now be integrated to obtain

$$\dot{m} = \int_0^{S_b} Dr_b dS_b + \dot{m}_0 \tag{21}$$

The $\dot{m}_0$ indicates the presence of burning on the head end. The value of $\dot{m}_0$ is

$$\dot{m} = DCP_0^n A_0 \tag{22}$$

Combining Equations 21 and 22 with the definition of η, one obtains

$$\eta = \frac{\eta_0}{A} \left(\int_0^{S_b} P^n dS_b + A_0 \right) \tag{23a}$$

$$\eta_0 = DCP_0^{n-1} \tag{23b}$$

Determination of the pressure distribution, or equivalently $\overline{P}$, as a function of x amounts to a simultaneous solution of the differential equation for $\overline{P}$ (Equation 19) and the integral equation for η, Equation 23a. For the three geometries of interest the equations to be solved are

$$\overline{P}' = \frac{\gamma\zeta}{(\zeta - \gamma\overline{P})y} \left\{ (\zeta - \overline{P}) \left[fH + y' \right] + \frac{G^2 \eta}{\zeta} \left[2\eta_0 \overline{P}^n - \eta y' \right] \right\}$$

Crack

$$\tag{25}$$

$$\eta = \frac{\eta_0}{y} \left(2 \int_0^x P^n dx + y_0 \right)$$

$$\overline{P}' = \frac{\gamma\zeta}{(\zeta - \gamma\overline{P})y}\left\{(\zeta - \overline{P})\left[\frac{f}{2}(H + 1) + y'\right] + \frac{G^2 n}{\zeta}\left[n_0 \overline{P}^n - ny'\right]\right\}$$

Debond (26)

$$n = \frac{n_0}{y}\left(\int_0^x \overline{P}^n\, dx + y_0\right)$$

$$\overline{P}' = \frac{\gamma\zeta}{(\zeta - \gamma\overline{P})y}\left\{(\zeta - \overline{P})\left[\frac{f}{2}(1 + H) + y' - \frac{y}{r}\right]\right.$$

Circular
Debond (27)

$$\left. + \frac{G^2 n}{\zeta}\left[n_0 \overline{P}^n - ny'\ \ \frac{ny}{r}\right] + \frac{\overline{P}y}{r}\frac{(\gamma - 1)}{\gamma}\right\}$$

$$n = \frac{n_0}{ry}\left(\int_0^x \overline{P}^n r\, dx + r_0 y_0\right)$$

In order to solve the governing equations, Equations 25, 26, or 27, it is necessary to establish the boundary condition. If the flow is subsonic at the exit plane of the flaw, then the pressure must equal the main chamber pressure, P_{ch}. If the flow chokes at the exit plane, the boundary condition is just Mach number equal to one. Although it is possible for flow in a diverging duct with mass addition to reach supersonic velocities, it is not a normal situation. To ascertain whether the exit Mach number can become greater than one it is necessary to evaluate the derivative of the Mach number as it approaches one.

Since the Mach number is of such prime importance, it should be introduced into the problem formulation. Because a perfect gas equation of state has been assumed as well as constant specific heats, the standard relationships developed in Reference 14 are applicable for Mach numbers.

The term $\dot{m}/P_r A$ which was given the symbol n can be written in terms of temperature and velocity

$$n = \frac{2u}{RT} \tag{28}$$

-12-

The temperature may be eliminated in Equation 28 utilizing the adiabatic expansion relationship

$$\frac{T_o}{T} = 1 + \frac{\gamma - 1}{2} M^2 \tag{29}$$

and the velocity u may be eliminated using the definition of Mach number and the perfect gas formulation for the speed of sound.

After rearranging the terms there is obtained

$$M^2 = \frac{(\pm [\overline{P}^2 + G^2{}_n{}^2]^{\frac{1}{2}} - \overline{P})}{\overline{P}(\gamma - 1)} \tag{30}$$

Utilizing the previously introduced notation

$$\zeta = [\overline{P}^2 + G^2{}_n{}^2]^{\frac{1}{2}} \quad ,$$

Equation 30 simplifies to

$$M^2 = \frac{(\pm \zeta - \overline{P})}{\overline{P}(\gamma - 1)} \tag{31}$$

In reality, only the plus sign in Equation 31 has significance as has been pointed out by Price[13].

The solution of the simultaneous governing equations (Equations 25, 26, or 27) may now be determined with the restrictions placed on the boundary exit plane of either

(a) Subsonic flow $P_e = P_{ch}$

(b) Choked flow $M_e = 1.0$

or

(c) Supersonic when $\lim\limits_{M \to 1} \frac{dM^2}{dx} \Big|$ is positive.

The condition (c) may be evaluated utilizing a general relationship developed by Shapiro.[14] Application of Shapiro's general formulation

-13-

to determine $\left.\dfrac{dM^2}{dx}\right|_{M=1}$ for the present problems yields

$$\lim \left.\frac{dM^2}{dx}\right|_{M \to 1} = \lim_{M \to 1} \frac{G(x)}{1 - M^2} \tag{32}$$

where

$$G(x) = M^2(1 + \frac{\gamma - 1}{2} M^2 \quad \frac{1}{A}$$

$$\left[2 \frac{dA}{dx} + \gamma f M^2 (S_\eta' + HS_b') + \frac{2(1 + \gamma M^2)}{\eta} \frac{d(A_\eta)}{dx} \right] \tag{33}$$

From Equation 33 it is clear that whether the local Mach number increases or decreases depends on whether the local Mach number is greater or less than unity and also whether the $G(x)$ is positive or negative. Since in the case under consideration the Mach number increases from practically zero at the crack tip, the sign of G determines whether local Mach number increases. The value of G is primarily dependent on the area and mass addition functions and, therefore, the sign of G is determined by the crack geometry and fuel-burning properties. For typical fuels and geometries, G is always positive. The Mach number, therefore, increases toward unity and unless G happens to decrease to zero precisely as $M = 1$ (which in general is not true), the flow will choke at this point. When choking occurs, there is a transient period of readjustment in which the tip pressure, P_0, is increased by an amount such that Mach 1 occurs at the exit plane, the pressure there is greater than the external pressure and expansion waves form at the flaw exit and extend into the rocket chamber.

The complicated nature of the governing equations together with the pressure dependence of the empirical burning laws for solid propellants, in general, allow for only numerical solutions of the stated problem. Appendix A describes the numerical procedures which were used to generate solutions to the problem of mass addition with friction in variable area ducts.

APPROXIMATE ANALYTICAL SOLUTION WITHOUT FRICTION FOR SPECIAL MASS FLUX DISTRIBUTIONS

An analytical solution may be obtained for the pressure distribution in a crack or debond if one neglects the effects of wall shear and the mass flux, η, varies as x^{k-q} where k and q are constants depending upon the geometry and fuel characteristics.

Equation 19 with the friction factor, f, equal to zero reduces to

$$\bar{P}' = \frac{\gamma\zeta}{(\zeta - \gamma\bar{p})} \left((\zeta - \bar{p}) \frac{y'}{y} + \frac{G^2 \eta\dot{\eta}'}{\zeta} \right) \tag{34}$$

for cases where the geometry is such that $\ell = 0$.

The form of Equation 34 is such that the relationship between $G\eta$, $\bar{P}$ and ζ corresponds to the sides of the triangle shown in Figure 3.
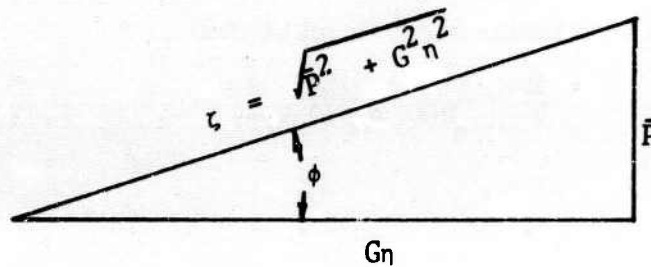
Figure 3. Relationship of $G\eta$, $\bar{P}$ and ζ.

As can be seen from Figure 3, ζ, $\bar{P}$ and $\bar{P}'$ can be expressed in terms $G\eta$ and an angle ϕ.

$$\zeta = \frac{G\eta}{\cos\phi} \tag{35}$$

$$\bar{P} = G\eta \tan \tag{36}$$

$$\bar{P}' = \frac{G\eta}{\cos^2\phi} \phi' + \tan\phi \, G' \tag{37}$$

Substituting Equations 35, 36 and 37 into Equation 34 and simplifying, there is obtained

$$\phi' = \frac{\cos\phi}{1 - \gamma \sin\phi}\left(\gamma(1 - \sin\phi)\frac{y'}{y} + (\gamma - \sin\phi)\frac{n'}{n}\right) \tag{38}$$

If $y'/y \sim n'/n$, from which it follows $y'/y \sim \dot{m}'/\dot{m}$, and if y and $\dot{m}$ are known functions of x, the possibility exists for separation of variables. A particular form for which this is true is

$$\dot{m} \sim x^k \tag{39}$$

$$y \sim x^q \tag{40}$$

In reality, $\dot{m}$ is given by the integral equation, Equation 21. However, under particular situations $\dot{m}$ can be approximately fitted by a power function such as Equation 39.

Substituting Equations 39 and 40 into Equation 38 yields

$$\phi' = \frac{\cos\phi}{x(1 - \gamma \sin\phi)} \cdot \left[\gamma k - (q(\gamma - 1) + k)\sin\phi\right] \tag{41}$$

Upon separation of variables there is obtained

$$\frac{dx}{x} = \frac{(1 - \gamma \sin\phi)\, d\phi}{B(k, q, \phi)\cos\phi} \tag{42}$$

where

$$B(k, q, \phi) = \gamma k - (q(\gamma - 1) + k)\sin\phi \tag{43}$$

Equation 42 falls into one of three distinct types, depending on the relationship of k to q. The three types are as follows:

1. $k = q$, therefore, $B(k, q, \phi) = \gamma k(1 - \sin\phi)$

2. $k = -q \frac{(\gamma - 1)}{(\gamma + 1)}$, therefore, $B(k, q, \phi) = \gamma k(1 + \sin\phi)$

3. $k \neq m$ and $k \neq -q \frac{(\gamma - 1)}{(\gamma + 1)}$

If the relation between k and q is of Type 1 or 2, then upon integration of Equation 42 one obtains

$$x \sim \tan\left(\frac{\pi}{4} + \frac{\phi}{2}\right)^{\frac{1 \mp \gamma}{2\gamma q}} \exp\left[\pm \frac{1 \mp \gamma}{2\gamma q\,(1 \mp \sin\phi)}\right] \tag{44}$$

where $+\sin\phi$ corresponds to $k = -q \frac{(\gamma - 1)}{(\gamma + 1)}$ and $-\sin\phi$ to $k = q$. If the relation between k and q is of Type 3, then Equation 43 integrates to

$$x \sim \left\{ \left(\tan\left(\frac{\pi}{4} + \frac{\phi}{2}\right) \right)^q \left(\frac{B(k,q,\phi)}{\cos\phi}\right)^{(\gamma - 1)k-q} \right\}^{\frac{1}{[k(\gamma+1) + q(\gamma-1)] \, (q-k)}} \quad (45)$$

In order to determine what values of ϕ are relevant in Equation 44 and 45, one must consider the Mach number. Applying the transforms of Equations 35, 36 and 37 to the Mach number relation, Equation 31, the following is obtained.

$$M^2 = \frac{1 - \sin\phi}{\sin\phi \, (\gamma - 1)} \quad (46)$$

From Equation 46 it can be seen that values of ϕ less than $\sin^{-1} 1/\gamma$ correspond to $M > 1.0$ and values of ϕ greater than $\sin^{-1} 1/\gamma$ to $M < 1.0$. Since the governing equation was derived assuming $M \leq 1.0$, it is apparent that ϕ must be greater than or equal to $\sin^{-1} 1/\gamma$.

Considering Figure 3, it can be seen that since both G_η and $\mathcal{P}$ are positive quantities, ϕ must be less than or equal to $\pi/2$. Now again considering Equation 45, notice that the term on the far right may take on imaginary values if $B(k, q, \phi)$ becomes negative. The possibility of $B(k, q, \phi)$ taking on negative values depends upon the relationship of k to q and upon the values which ϕ is allowed to assume. Setting $\phi = \pi/2$ and $B(k, q, \phi) = 0$ and solving for k in terms of q, one obtains $k = q$. Therefore, if k is greater than q, the term $B(k, q, \phi)$ does not become negative and the upper limit on ϕ is $\pi/2$. If k is less than q, the term $B(k, q, \phi)$ may become negative and in this case the upper limit on ϕ is that value of ϕ at which $B(k, q, \phi) = 0$. As was pointed out before, the smallest value which ϕ may assume is $\sin^{-1} 1/\gamma$ at which point $M = 1.0$; therefore, setting $\phi = \sin^{-1} 1/\gamma$ and $B(k, q, \phi) = 0$ and solving for k, one obtains $k = q/(\gamma + 1)$. This last result indicates that k must be greater than or equal to $q/(\gamma + 1)$ for the equation to yield a realistic flow. It is apparent that the $+\sin\phi$ choice in Equation 44 has no physical meaning since it corresponds to a flow which is choked at $\phi = 0$. All of the above results are summarized in Figure 4.

$k > q$	$\sin^{-1}\dfrac{1}{\gamma} \le \phi \le \pi/2$
$k < q$	$\sin^{-1}\dfrac{1}{\gamma} \le \phi \le \sin^{-1}\dfrac{\gamma k}{k + q(\gamma - 1)}$
$k \le \dfrac{q}{\gamma + 1}$	flow choked

Figure 4. Dependency of relevant ϕ range on the relationship of k to q.

For the relevant range of ϕ enumerated in Figure 4, one may consider the relationship between ϕ and x. Notice in Equation 45 that if $k > q$, then $[k(\gamma + 1) + q(\gamma - 1)](q - k) < 0$ and, therefore, as $\phi \to \pi/2$, $x \to 0$. When $k < q$, $x = 0$ at $\phi = \sin^{-1} k/(k + q(\gamma - 1))$. If $k = q$, Equation 44 describes the relationship of x to ϕ. Letting $\phi \to \pi/2$ in Equation 44, note that $\tan(\pi/4 + \phi/2) \to 2/(1 + \cos\phi - \sin\phi)$. Setting $1 - \sin\phi = w$ and letting $w \to 0$ is equivalent to letting $\phi \to \pi/2$; therefore, making the above substitution in Equation 44, one has as $\phi \to \pi/2$

$$x \to \text{const.}\left(\frac{1}{w}\right)^{\frac{1 + \gamma}{2\gamma q}} e^{\frac{1 - \gamma}{2\gamma q w}}$$

But the above limit is of the form

$$x \to \left\{ \text{const } \frac{e^{\frac{g}{w}}}{w} \right\}^{\frac{1 + \gamma}{2\gamma q}}$$

where

$$g = \frac{1 - \gamma}{1 + \gamma}$$

Expanding $e^{g/w}$ into a series and noting that $g < 0$, one obtains as $\phi \to \pi/2$, $x \to 0$ in Equation 44.

-13-

From the definition of η and the assumed form of y and $\dot{m}$ it is apparent that

$$\eta \sim s^{k-q} \tag{47}$$

Taking both sides of Equation 45 to the $k - q$ power, one can determine that if $k \neq q$

$$\eta \sim \left| \left(\tan \left(\frac{\pi}{4} + \frac{\phi}{2} \right)^{-\gamma q} \left(\frac{B(k, q, \phi)}{\cos\phi} \right) \right)^{q - k(\gamma+1)} \right|^{\frac{1}{k(\gamma + 1) + q(\gamma - 1)}} \tag{48}$$

If $k = q$, however, η is a constant.

The parameter of greatest concern is $\bar{P}$ and the region of greatest concern is the tip region. When $k > q$, it has been shown that $x \to 0$ corresponds to $\phi \to \pi/2$. Equation 48 gives η as a function of ϕ and Equation 36 gives $\bar{P}$ as a function of η and ϕ. Therefore, substituting Equation 48 into Equation 36 gives $\bar{P}$ as a function of ϕ alone

$$\bar{P} \sim \tan\phi \left| \left(\tan \left(\frac{\pi}{4} + \frac{\phi}{2} \right)^{-\gamma q} \left(\frac{B(k, q, \phi)}{\cos\phi} \right) \right)^{q - k(\gamma + 1)} \right|^{\frac{1}{k(\gamma + 1) + q(\gamma - 1)}} \tag{49}$$

Observing Equation 49 as $\phi \to \pi/2$, one may note the following

$$B(k, q, \phi) \to (\gamma - 1)(k - q)$$

therefore, as $\phi \to \pi/2$

$$\bar{P} \to \text{Constant} \frac{\sin\phi}{\cos\phi} \left| \left(\frac{1}{1 + \cos\phi - \sin\phi} \right)^{-\gamma q} \left(\frac{1}{\cos\phi} \right)^{q - k(\gamma+1)} \right|^{\frac{1}{k(\gamma+1)+q(\gamma-1)}}$$

Simplifying and rearranging, one has

$$\bar{P} \to \text{Constant} \left\{ \frac{1 + \cos\phi - \sin\phi}{\cos\phi} \right\}^{\frac{\gamma q}{k(\gamma + 1) + q(\gamma - 1)}}$$

Applying L'Hospital's rule, the above relation yields $\overline{P} \to$ constant. Therefore, if $k > q$ as $x \to 0$, the pressure approaches a constant.

If $k = q$, $x \to 0$ corresponds, again, to $\phi \to \pi/2$; however, since η is constant, $\overline{P} \to \infty$ as $x \to 0$.

If $k < q$, then $k - q < 0$ and $\eta \to \infty$ as $x \to 0$ since $\eta \sim x^{k-q}$. But $x \to 0$ corresponds to $\phi \to \sin^{-1}(\gamma k)/(k + q(\gamma - 1))$; therefore, $\overline{P} \to \infty$.

From Equation 34 one can see that the distribution of $\overline{P}$ with x as $x \to 0$ is determined to a great extent by the behavior of $\eta\eta'$ as $x \to 0$. Since $\eta \sim x^{k-q}$, then $\eta\eta' \sim x^{2(k-q)-1}$ and, therefore,

if $k - q > 1/2$, then $\eta\eta' \to 0$ as $x \to 0$;

if $k - q = 1/2$, then $\eta\eta' =$ constant;

if $k - q < 1/2$, then $\eta\eta' \to \infty$ as $x \to 0$.

Consider, first, $k - q > 1/2$ and examine the limit of $\overline{P}'$ as $x \to 0$. Noting that $\zeta \to \overline{P}$ one has

$$\overline{P}' \to \frac{\gamma}{1-\gamma} [(\zeta - \overline{P}) \, y'/y]$$

applying L'Hospital's rule

$$\overline{P}' \to \frac{\gamma}{1-\gamma} (\zeta' - \overline{P}') \text{ but } \zeta' = \overline{P}\overline{P}'/\zeta + (G^2\eta\eta')/\zeta$$

and, therefore, as $x \to 0$,

$$\zeta' \to \overline{P}' + (G^2\eta\eta')/\overline{P} \text{ and } \overline{P}' \to \gamma/(1-\gamma) \, G\eta\eta' \to 0$$

Next consider the limit of $\overline{P}'$ as $x \to 0$ for $k - q = 1/2$. One still has $\zeta \to \overline{P}$ as $x \to 0$ and, therefore,

$$\overline{P}' \to \frac{\gamma}{1-\gamma} \left[(\zeta' - \overline{P}') + \frac{G^2\eta\eta'}{\overline{P}} \right] \to \text{Constant}$$

Finally consider the limit of $\overline{P}'$ for $k - q < 1/2$. As before $\zeta \to \overline{P}$ as $x \to 0$; however, $\eta\eta' \to \infty$, therefore,

$$\overline{P}' \to \frac{2\gamma}{1-\gamma} \, \frac{G^2\eta\eta'}{\overline{P}} \to \infty$$

as $x \to 0$.

Equation 34 also indicates that no matter what the relation of k to q that $\overline{P}' \to \infty$ as $\zeta \to \not{P}$, or in other words, the slope of the curve for $\overline{P}$ as a function of x is infinite as the flow exit for all choked flows. Figure 5 summarizes all of the above results.
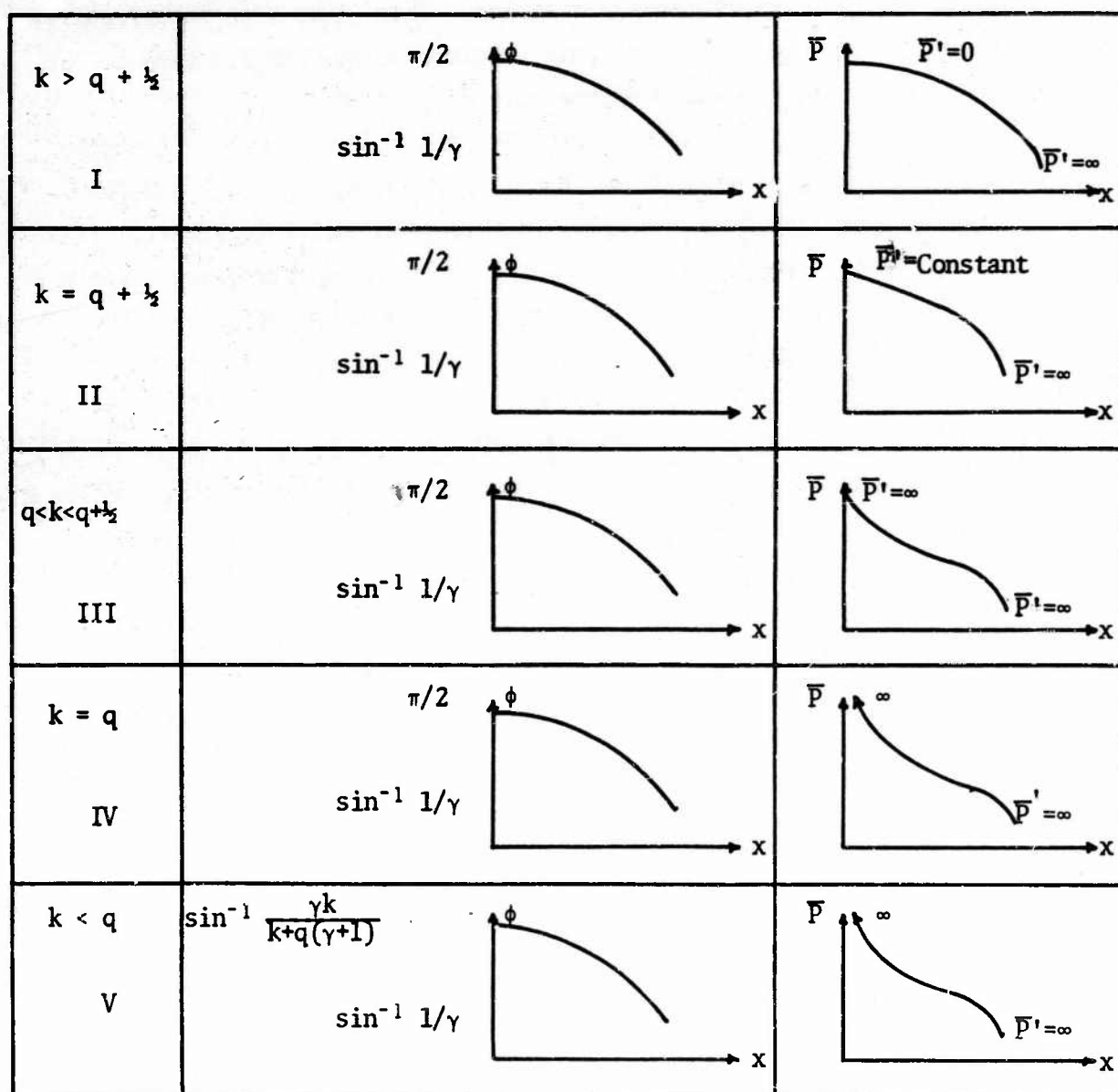

Figure 5. ϕ versus x and $\overline{P}$ versus x for various k and q relations

EFFECT OF FRICTION ON PRESSURES PREDICTION IN CRACKS AND DEBONDS

Analysis of pressure distributions in burning flaws have been investigated previously at ERDE [9] assuming that the combustion gases were incompressible. They determined the pressure distribution assuming the standard pressure drop in a duct due to friction. Although the gases are both viscous and compressible, a degree of satisfaction was obtained when the analysis was compared with limited experimental data from tests in which the cracks were not choked. This gives rise to a requirement to evaluate the effects of both compressibility and friction to see whether either can generally be neglected.

Figures 6 and 7 show the predicted pressure distributions from the analysis of the first portion of this chapter in both a crack and debond of similar geometry for a relatively high burning rate propellant. (The burning rate is higher than for TP H-1011.) The geometry was purposely chosen so that in neither case would the flow be choked to the extent that the exit plane pressure was higher than the chamber pressure. As can be seen, for both the crack and the debond, a considerable error would be introduced by neglecting the friction; however, the major reason for the large over pressures in each flaw was due to compressibility effects.

For the case of the debond with its lower over pressures and lower mass flow the effect of friction did not greatly affect the Mach number. For the crack with its higher mass flow and choked condition, the effects of friction cause a greater rate of change in the Mach number near the exit of the crack.

The results illustrated definitely support the inclusion of both friction and compressibility in evaluating the fluid mechanics of burning in flaws in propellant grains.
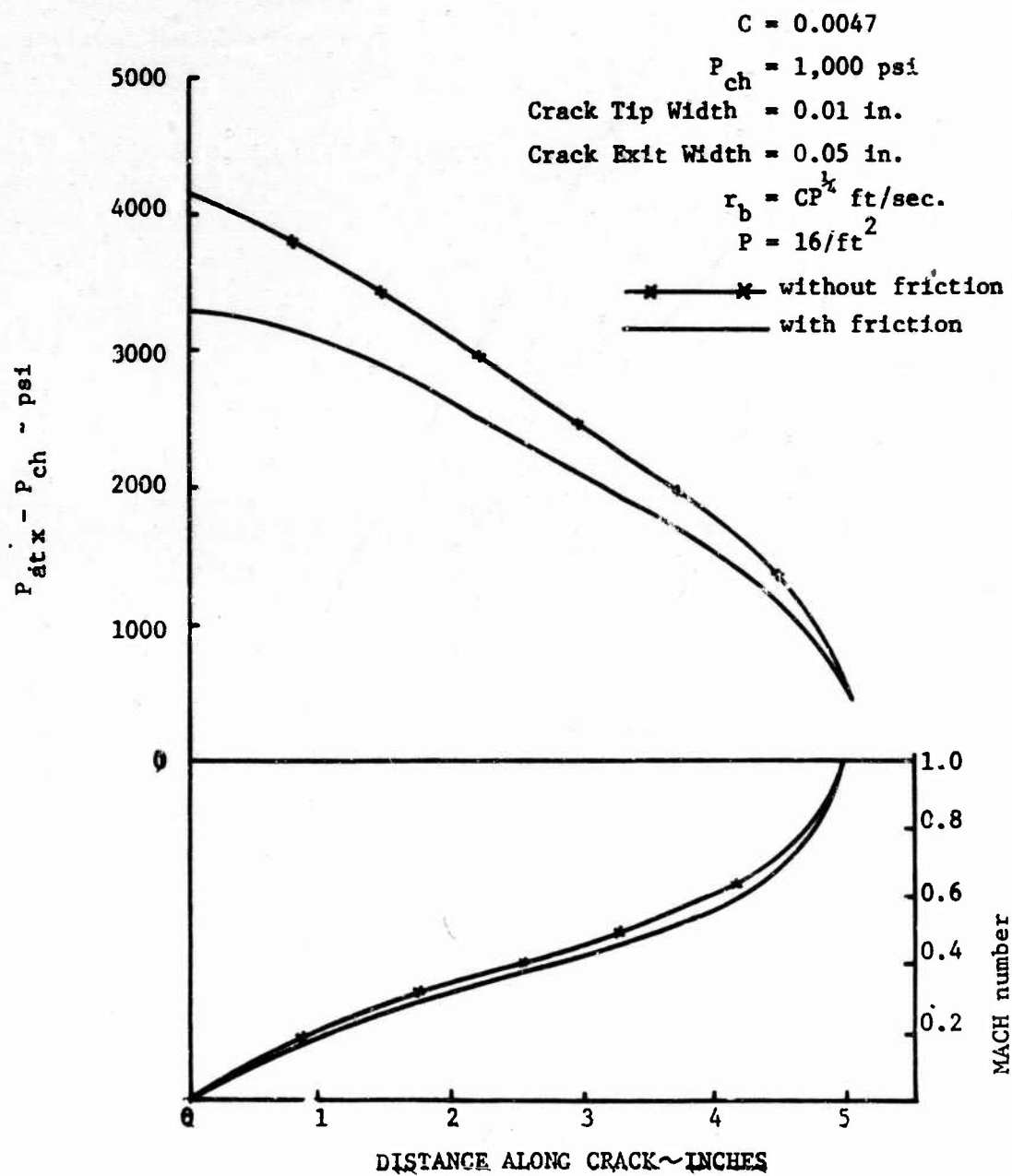
Figure 6. Pressure and Mach number distributions along the length of a constantly diverging crack with and without friction
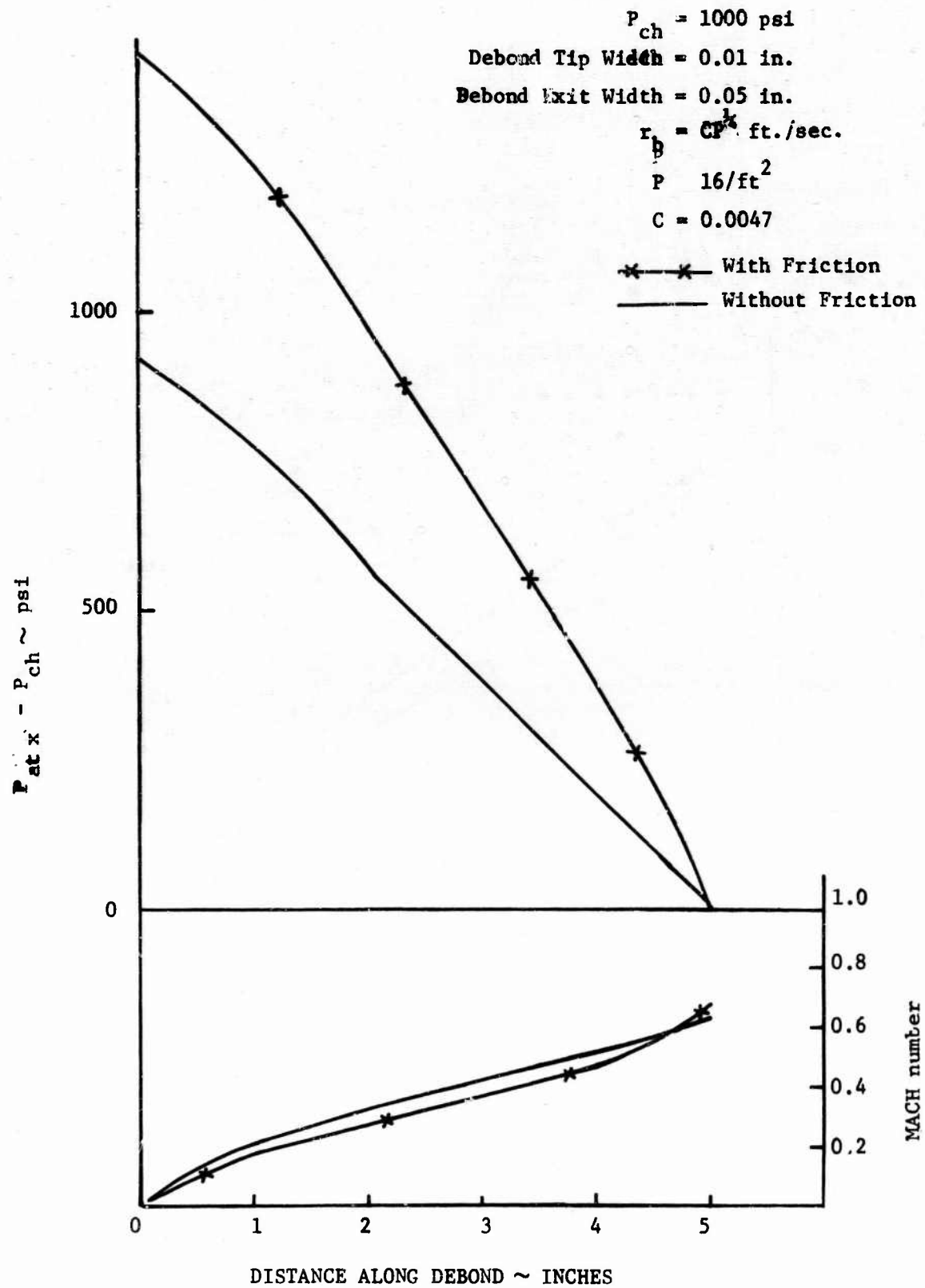
Figure 7. Pressure and Mach number distributions along the length
of a constantly diverging debond with and without friction.

EVALUATION OF TWO-DIMENSIONAL MODELS OF FLOW IN A FISSURE WITH COMBUSTION

Presented in preceding sections was a one-dimensional model for the flow and pressure distribution in a burning fissure. It i: rtant to determine in what limits this one-dimensional representation yields a reliable representation of the actual flow. The following analyses are intended to answer such questions. First, the limiting geometry is determined in which compressibility effects become important. Since flow from the transpiring burning surface is rotational, it is also appropriate as a second problem to determine the effects of vorticity on flow in the burning crack.

Effects of Compressibility

The following is a two-dimensional perturbation solution of the compressible flow field in a sharp crack with arbitrary mass addition at the wall. A basic assumption is that the Mach number of the flow at the transpiring wall is small; the wall Mach number thus serves as a convenient perturbation parameter. Another assumption is that the flow is irrotational and this severely affects the type of boundary conditions which can be satisfied in the solution. In a later section the effects of rotationality are assessed. In particular, the condition of normal effluxe at the wall must be relaxed to secure an irrotational solution. It is readily demonstrated that an irrotational flow in geometrical situations of the present type is only possible with normal mass injection for a special distribution of wall sources. If, for example, the burning is uniform, then the flow cannot be irrotational unless a velocity component parallel to the transpiring wall is allowed.

Figure 8 illustrates the assumed geometry. Angle θ_o is the half angle of the triangular sharp crack. Assuming irrotational flow, the problem may conveniently be represented by a velocity potential ϕ such that

$$\nabla\phi = \bar{u} = u\hat{e}_r + v\hat{e}_\theta \tag{50}$$

where $\bar{u}$ is the flow velocity vector. The governing equation for steady flow is, therefore,

-25-

$$\nabla^2\phi = \nabla\phi\cdot\nabla\left(\frac{\nabla\phi\cdot\nabla\phi}{2}\right) + \left(\frac{\gamma-1}{2}\right)\nabla^2\phi\ (\nabla\phi\cdot\nabla\phi) \tag{51}$$

where all quantities are nondimensionalized by a characteristic length representative of the length of the crack and the stagnation speed of sound of the combustion gases a_o. The boundary condition is that the normal components of flow at the wall is

$$v = \mp vf(r) \quad \text{on } \theta = \pm\theta_o \tag{52}$$

where v is a Mach number representative of the flow at the wall and $f(r)$ is the distribution of sources along the wall.

In the plane polar coordinates, the full problem for compressible irrotational flow is
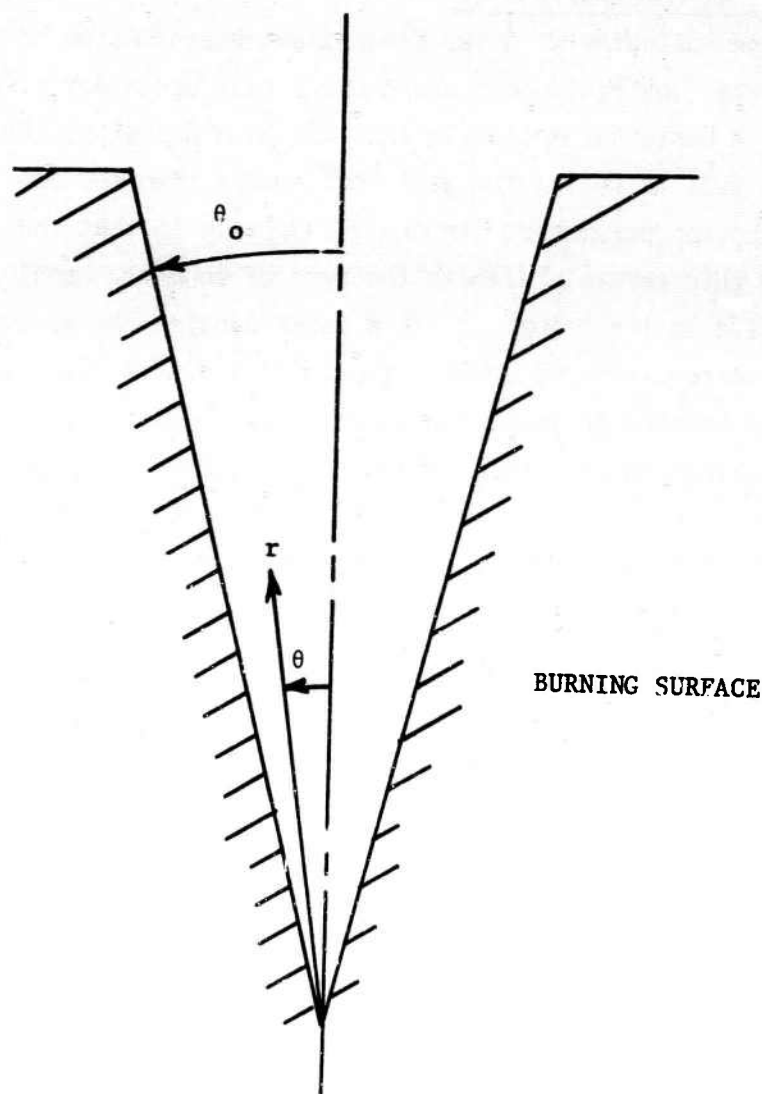

Figure 8. Two-dimensional representation of a sharp crack

-26-

$$\phi_{rr} + \frac{1}{r}\phi_r + \frac{1}{r^2}\phi_{\theta\theta} = \left[\begin{array}{c} \phi_r^2\,\phi_{rr} + \dfrac{\phi_\theta^2\phi_{\theta\theta}}{r^4} + \\[2ex] + \dfrac{\phi_r\phi_\theta^2}{r^3} + 2\,\dfrac{\phi_r\phi_\theta}{r^2}\,\phi_{r\theta} + \\[2ex] + \left(\dfrac{\gamma-1}{2}\right)\left(\phi_r^2 + \dfrac{\phi_\theta^2}{r^2}\right)\left(\phi_{rr} + \dfrac{\phi_r}{r} + \dfrac{\phi_{\theta\theta}}{r^2}\right) \end{array}\right]$$

$$\phi_\theta = \mp \nu[rf(r)] \quad \text{on } \theta = \pm\theta_o \tag{53}$$

The form of the boundary condition suggests a perturbation approach with ν as the small parameter. Put

$$\phi = \nu\phi^{(1)} + \nu^2\phi^{(2)} + \ldots \tag{54}$$

and collect various orders of ν:

$0(\nu)$:

$$\begin{cases} \phi_{rr}^{(1)} + \dfrac{1}{r}\phi_r^{(1)} + \dfrac{1}{r^2}\phi_{\theta\theta}^{(1)} = 0 \\[3ex] \phi_\theta^{(1)} = \mp\, rf(r) \quad \text{on} \quad \theta = \pm\theta_o \end{cases} \tag{55}$$

$0(\nu^2)$:

$$\begin{cases} \phi_{rr}^{(2)} + \dfrac{1}{r}\phi_r^{(2)} + \dfrac{1}{r^2}\phi_{\theta\theta}^{(2)} = 0 \\[3ex] \phi_\theta^{(2)} = 0 \quad \text{on} \quad \theta = \pm\theta_o \end{cases} \tag{56}$$

$0(\nu^3)$:

$$\left\{\begin{array}{l} \phi_{rr}^{(3)} + \dfrac{1}{r}\phi_r^{(3)} + \dfrac{1}{r^2}\phi_{\theta\theta}^{(3)} = \phi_r^{(1)^2}\phi_{rr}^{(1)} + \dfrac{\phi_\theta^{(1)^2}\phi_{\theta\theta}^{(1)}}{r^4} \\[3ex] \phi_\theta^{(2)} = 0 \quad \text{on} \quad \theta = \pm\theta_o \qquad -\dfrac{\phi_r^{(1)} b_\theta^{(1)^2}}{r^3} + \dfrac{2\phi_r^{(1)}\phi_\theta^{(1)}}{r^2}\,\phi_r^{(1)} \end{array}\right\} \tag{57}$$

and so on. Note that the correction for compressibility enters at the third-order term. The second-order solution is trivial. Thus, as long as ν is sufficiently small, the solution will correspond closely to the incompressible case.

Solution of the incompressible problem (Equation 55) is simple. The eigenfunctions corresponding to the Laplace equation in plane polar coordinates are

$$\phi_\kappa^{(1)} = (A_\kappa \sin \kappa\theta + B_\kappa \cos \kappa_\theta)(C_\kappa r^\kappa + D_\kappa r^{-\kappa}) \tag{58}$$

where κ is an integer.

Solution to the present problem may be constructed as an infinite series of these eigenfunctions:

$$\phi^{(1)} = \sum_{\kappa=1}^{\infty} (A_\kappa \sin \kappa\theta + B_\kappa \cos \kappa\theta)(C_\kappa r^\kappa + D_\kappa r^{-\kappa}) \tag{59}$$

The coefficients may be determined by matching the boundary conditions (Equation 55). Note by symmetry, $A_\kappa \equiv 0$, thus

$$\phi_\theta^{(1)} \Big|_{\theta = \pm \theta_o} = \mp rf(r) = \mp \sum_{\kappa=1}^{\infty} \kappa \sin \kappa\theta_o (C_\kappa r^\kappa + D_\kappa r^{-\kappa}) \tag{60}$$

coefficients C_κ, D_κ are readily determined if $f(r)$ can be expanded in a Taylor series. The simplest case is for uniform transpiration, $f(r) = 1$. Then all terms in the series must vanish except for $\kappa = 1$ and $D_\kappa \equiv 0$. Thus

$$r = (\sin \theta_o) C_1 r$$

and

$$C_1 = \frac{1}{\sin \theta_o}$$

The velocity potential for this case is

$$\phi^{(1)} = \left(\frac{\cos \theta}{\sin \theta_o}\right) r \tag{61}$$

and $f(r) = 1$ which shows that the magnitude of the velocity is constant,

$$|\bar{u}| = \frac{v}{\sin \theta_o} + 0(v^3)$$ (62)

and depends only on the wall Mach number and the crack half-angle θ_o. There is a restriction on θ_o. Note if $\theta_o \to 0(v)$, then the perturbation scheme breaks down and compressibility effects are likely to be important. For typical propellants,

$$10^{-3} < v < 10^{-2}$$

so that the present solution is valid for cracks with $\theta_o > 5°$. For narrower cracks, compressibility effects must be represented obviously since the Mach number within the crack approaches unity. The solution implies that the flow may be choked for a sufficiently narrow crack, as already indicated in the one-dimensional solution.

Effects of Vorticity

It is appropriate to question the validity of the one-dimensional analysis in representing the rotational flow generated by burning of the walls of a long crack. As shown in the preceding analysis attempts to construct a two-dimensional solution with the assumption of irrotational flow do not properly satisfy the boundary conditions. Such solutions exhibit a component of velocity parallel to the surface of the burning propellant. The burning process requires that the velocity be normal to the surface. Thus vorticity is generated in the burning process and is transported along the streamlines; the flow is rotational.

Assuming a sufficiently wide crack, the flow may be assumed incompressible as shown in the preceding analysis. Since the flow is rotational, it is convenient to work with the stream function ψ such that

$$\bar{u} = \frac{\partial \psi}{\partial y}, \ \bar{v} = -\frac{\partial \psi}{\partial x} \qquad \bar{u} = \frac{1}{r}\frac{\partial \psi}{\partial \theta} e_r, \ \bar{v} = -\frac{\partial \psi}{\partial r} e_\theta$$ (63)

for cartesian and polar coordinates respectively.

The governing equation is

$$\nabla^2 \psi = -\omega(\psi)$$ (64)

where ω is the vorticity. The vorticity vector is of course perpendicular to the flow since planar flow is assumed.

Solutions are readily determined for the rectangular geometry shown in Figure 9. The boundary value problem becomes

$$\frac{\partial^2 \psi}{\partial x^2} + \frac{\partial^2 \psi}{\partial y^2} = - \omega(\psi) \tag{65}$$

$$\frac{\partial \psi}{\partial y} = \pm \nu f(y) \qquad \text{on } x = \pm a \tag{66}$$

$$\frac{\partial \psi}{\partial x} = 0 \qquad \text{on } x = \pm a \tag{67}$$

where the flow is forced to be normal to the burning surface as required by the combustion process. Solutions may be determined for arbitrary burning rate as reflected by the function $f(y)$. ν is representative of the Mach number of combustion products near the origin at the crack tip. Solutions of the type required here may be found by assuming ω to be proportional to ψ. Put

$$\omega = c^2 \psi \tag{68}$$

where $c = $ constant.

This assumption is valid if dissipation within the flow field is neglected. For uniform burning, $f(y) = 1$, the appropriate solution is simply

$$\psi = -\nu y \sin(\frac{\pi x}{2a}) \tag{69}$$

which assumes no burning at the crack tip. Streamlines for this solution are shown in Figure 9.
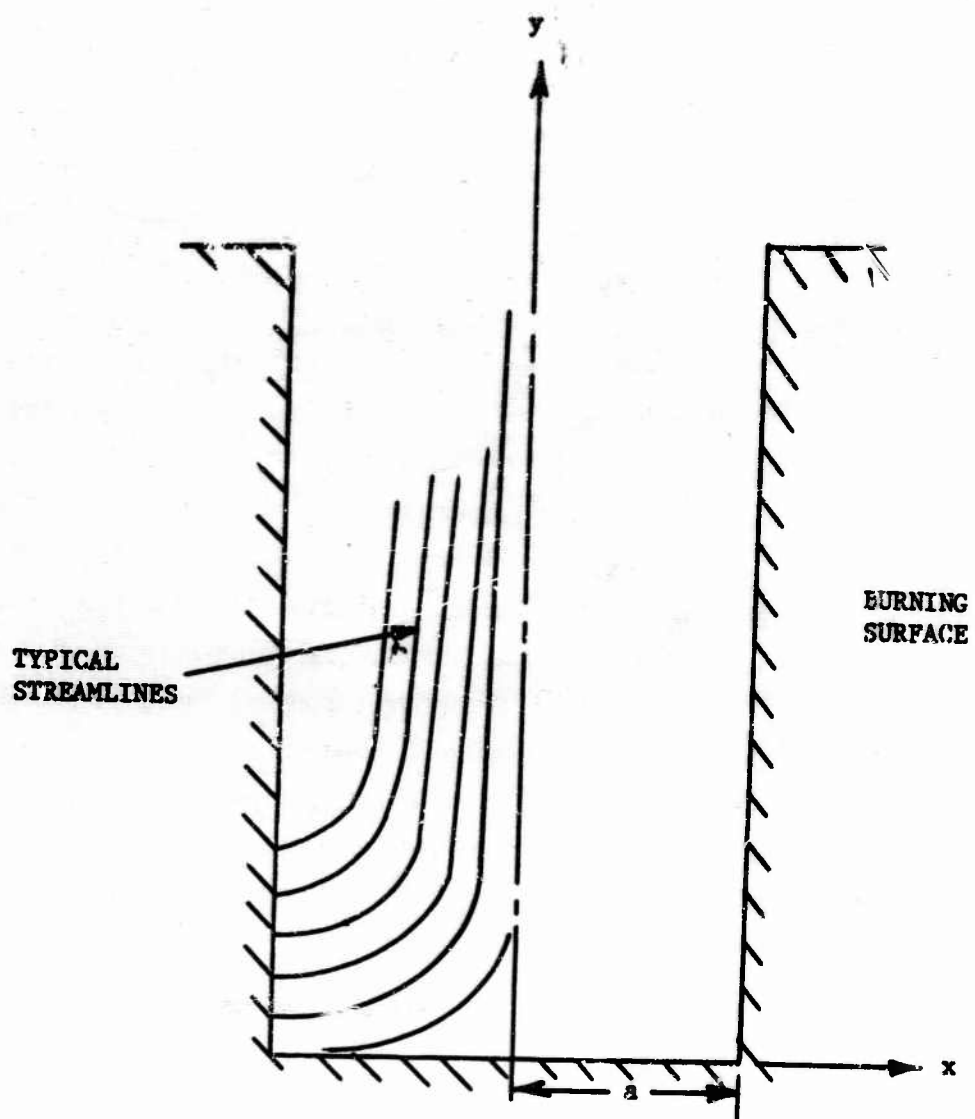
Figure 9. Rotational flow in rectangular crack with combustion

III. PARAMETRIC STUDY OF THE PRESSURE DISTRIBUTIONS
FOR BURNING CRACKS AND DEBONDS

Presented herein is a parametric study of the influence of geometric and propellant characteristics on the pressure distribution in cracks and debonds. The study is carried out primarily for TPH-1011 propellant; however, the effects of higher burning rates are indicated.

EFFECT OF FLAW LENGTH AND EXIT AREA ON CRACK TIP PRESSURE

Although the entire distribution of pressure along the length of a flaw is necessary to calculate the surface energy of the flaw, the pressure most characteristic of the loading is the tip pressure. This is the pressure at the location of propagation and the location of the maximum burning rate as well. Therefore, to illustrate the effects of flaw geometry on the pressures within a burning flaw, the flaw tip pressure is presented as a function of flaw length. Assuming a triangular or uniformly diverging flaw for illustrative purposes, the exit crack width serves to illustrate the effects of exit area.

Figures 10 and 11 indicate the effects of flaw length and exit width for a crack and a debond respectively. The propellant properties used are those of TPH-1011. It is assumed that the main chamber pressure is 1000 psia and that the crack tip width is 0.01 inches.

For both cases it is seen that the flaw tip pressure increases rapidly with increasing length and, further, that the pressure increases with decreasing angle of divergence (decreasing flaw width).

EFFECT OF ASSUMED FLAW TIP DIMENSIONS

Numerical solutions of the governing one-dimensional equations presented in Section II-A for cracks and debonds cannot be obtained if the crack is assumed sharp. In addition, there is no such thing as a truly sharp crack. However, it would appear reasonable to evaluate the effect of the assumed tip geometry numerically as it approaches zero to ascertain the form of the singularity at zero tip area.
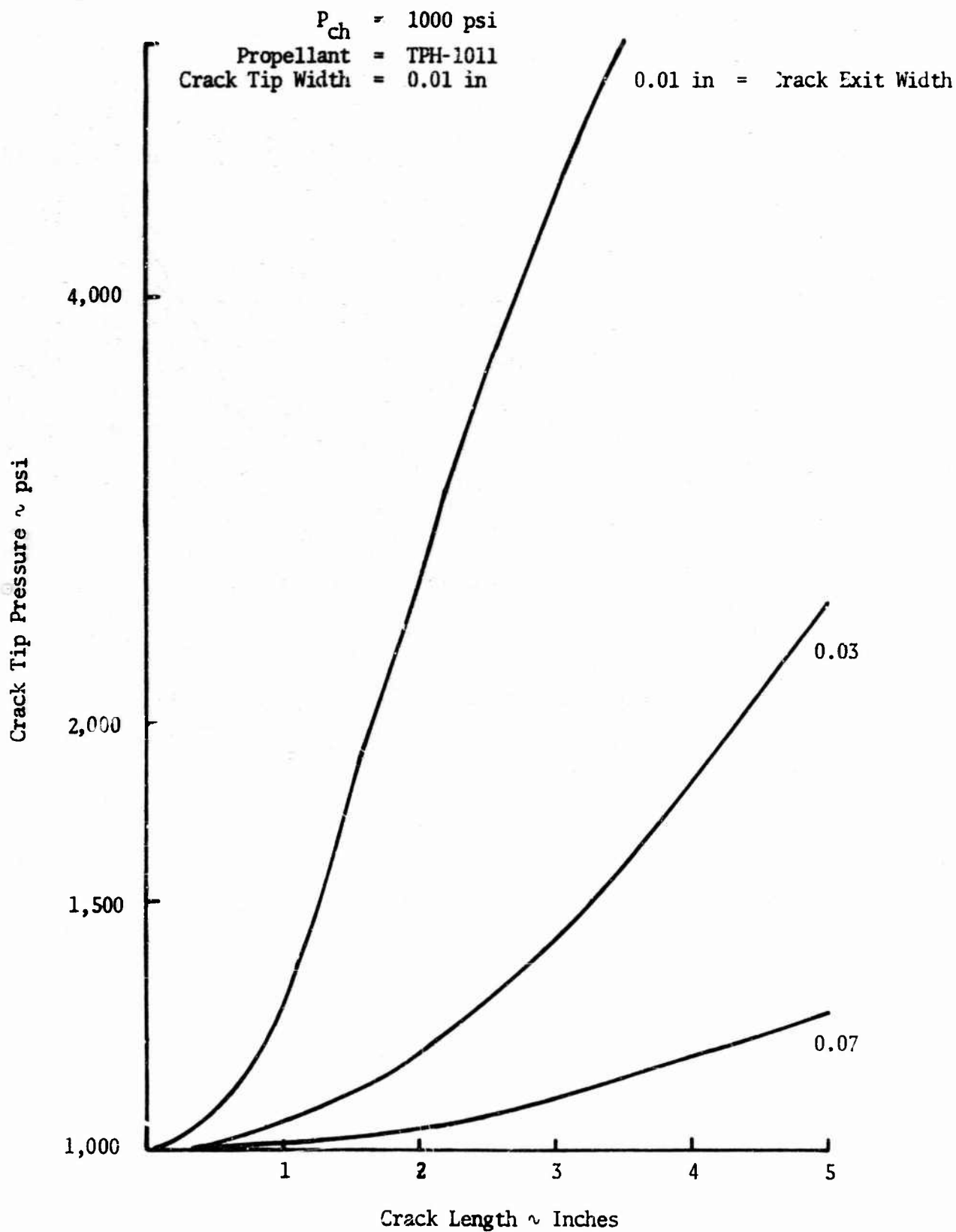
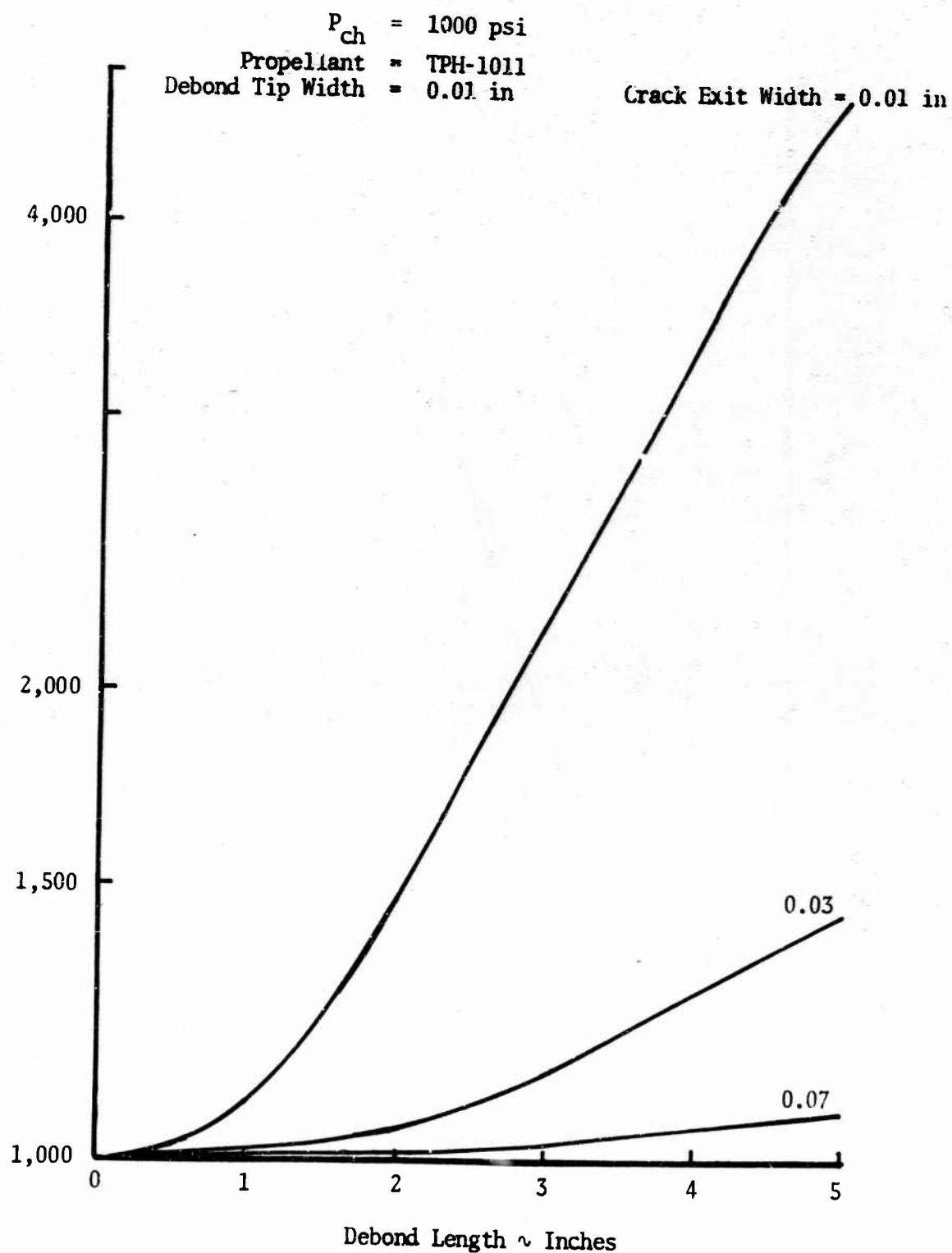Figure 10 Crack tip pressure versus length for several crack geometries

-33-

Figure 11. Debond tip pressure versus length for several debond geometries

Figures 12 and 13 present typical results for both a triangular crack and a triangular debond of otherwise constant geometry. The geometry chosen was a length of two inches and an exit width of 0.05 inches. The propellant was assumed to be TPH-1011 and the chamber pressure 1,000 psia. For both types of flaws there were small changes in tip pressure for a decrease in tip width from 0.01 inches to 0.001 inches. Further decreases in tip width down to 10^{-4} inches caused changes of only 400 psi for the case of the crack (Figure 13) and 200 psi for the debond (Figure 12).

EFFECT OF BURNING RATE LAW

Figures 14 and 15 indicate the effects of propellant burning rate coefficients, GDC, on the flaw tip pressure over a range of flaw lengths. The analysis assumed constant tip and exit plane widths and a constant chamber pressure. $C = 0.0047$ is equivalent to TPH-1011. As can be seen, the propellant burning rate has a strong effect on the resulting pressures. While the lower burning rate propellant, $C = 0.00027$ shows negligible increase in pressure, TPH-1011 and faster burning propellants rapidly reach high over pressures. Thus, all conclusions reached here for TPH-1011 flaw tip pressure would be conservative estimates of what would occur in faster burning propellants such as the double base propellants utilized in some operational systems.

Figures 16 and 17 present plots of exit plane Mach numbers for the propellants of Figures 14 and 15. The higher burning rate propellant reaches choked conditions for flaw lengths considerably less than those considered.

TYPICAL INCREASE IN FLAW LENGTH WITH TIME, ASSUMING NO MECHANICAL PROPAGATION

The computer program described in Appendix B will account for all changes in flaw geometry as a function of time, assuming that the flaw does not propagate mechanically. Typical results for cracks and debonds are presented in Figures 18 and 19 respectively. As can be seen, for the constant initial width flaws assuming TPH-1011 propellant with a chamber pressure of 1,000 psia, the rate of increase in length with time varies directly with initial crack length. This is as would be expected since it correlates directly with the pressure loadings. The crack growth
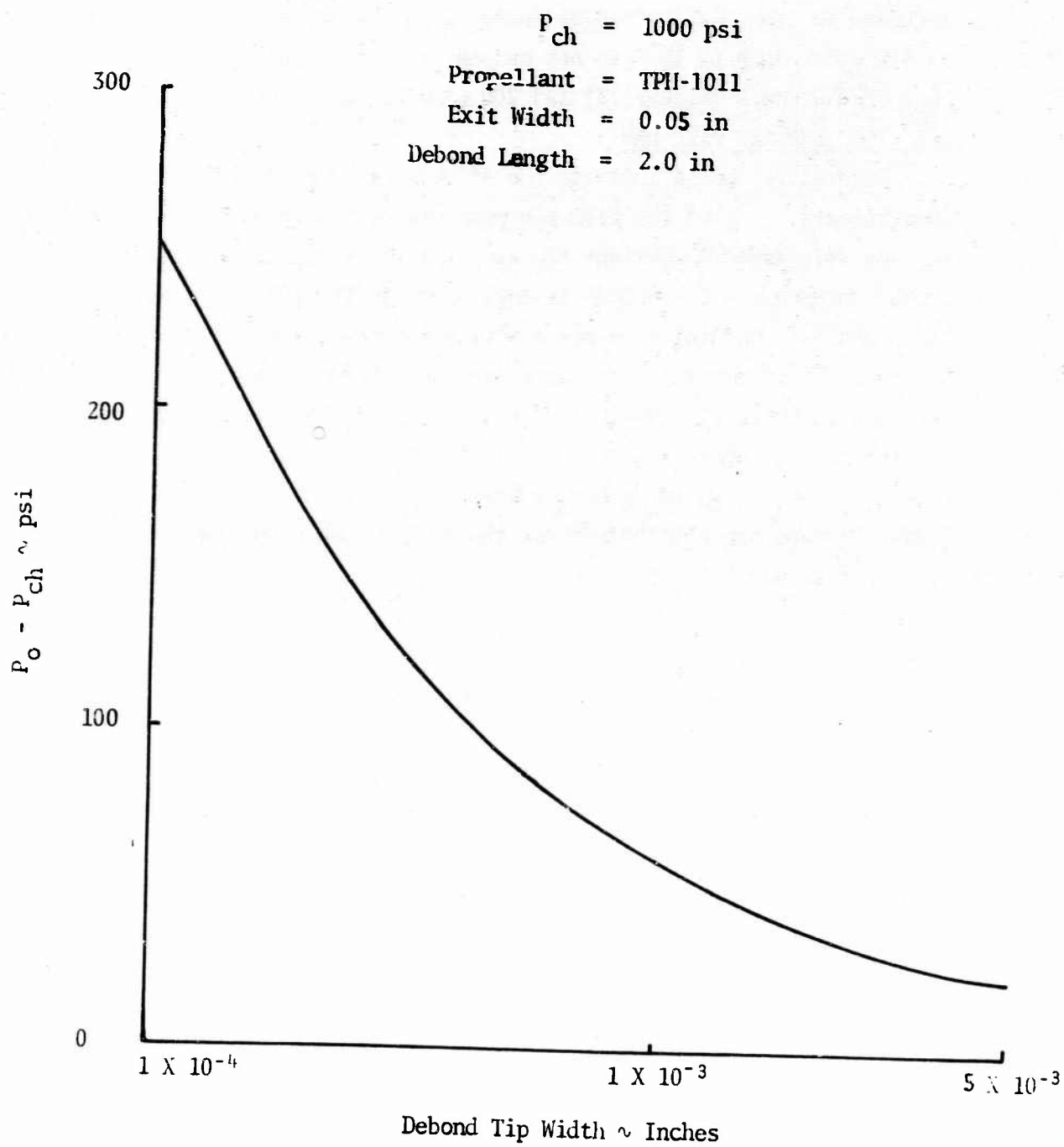
Figure 12. Tip over-pressure, $P_o - P_{ch}$, versus tip width, y_o, for constant exit width and length debond
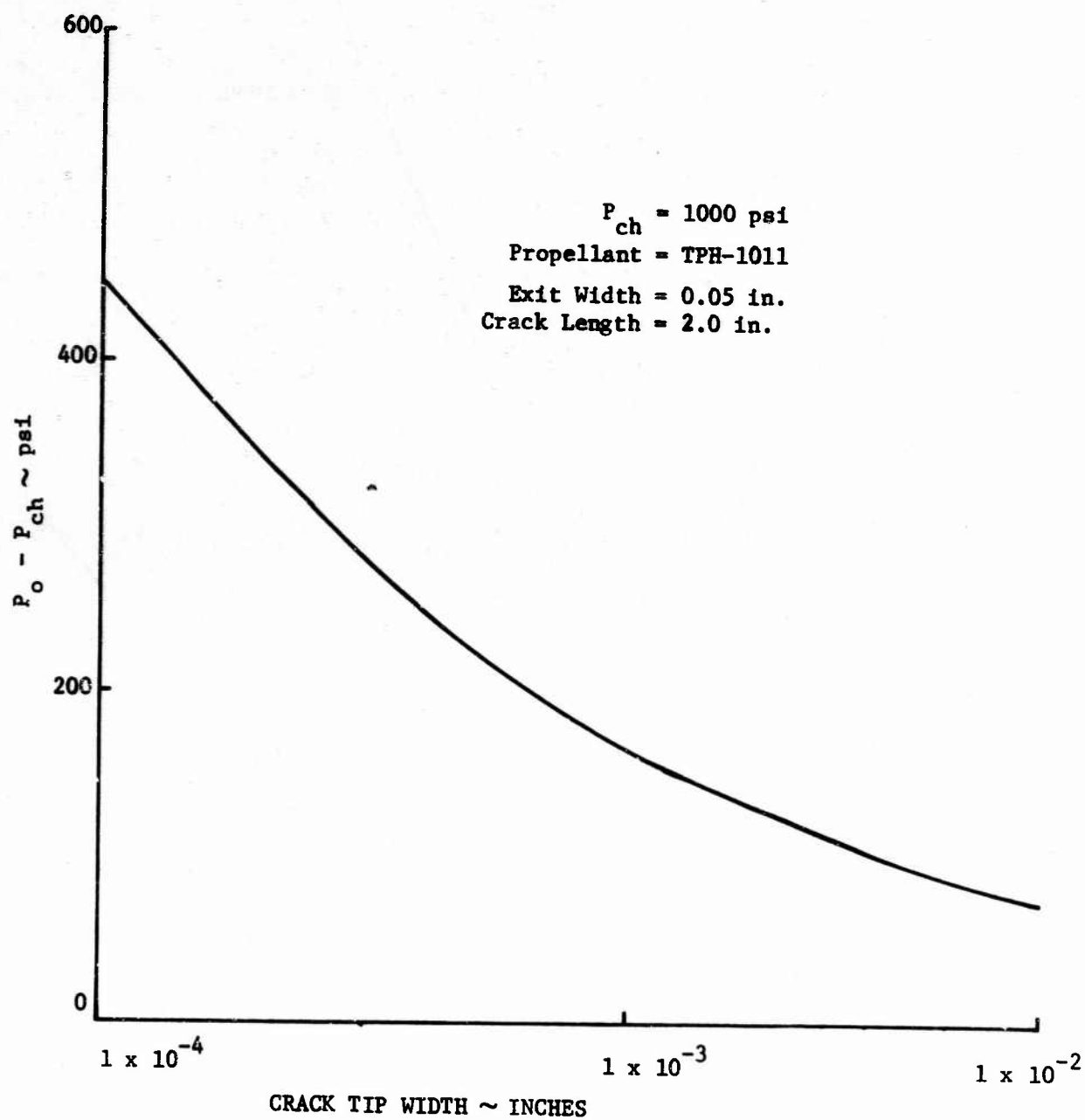
Figure 13. Tip over-pressure, $P_o - P_{ch}$, versus tip width, y_o, for constant exit width and length crack
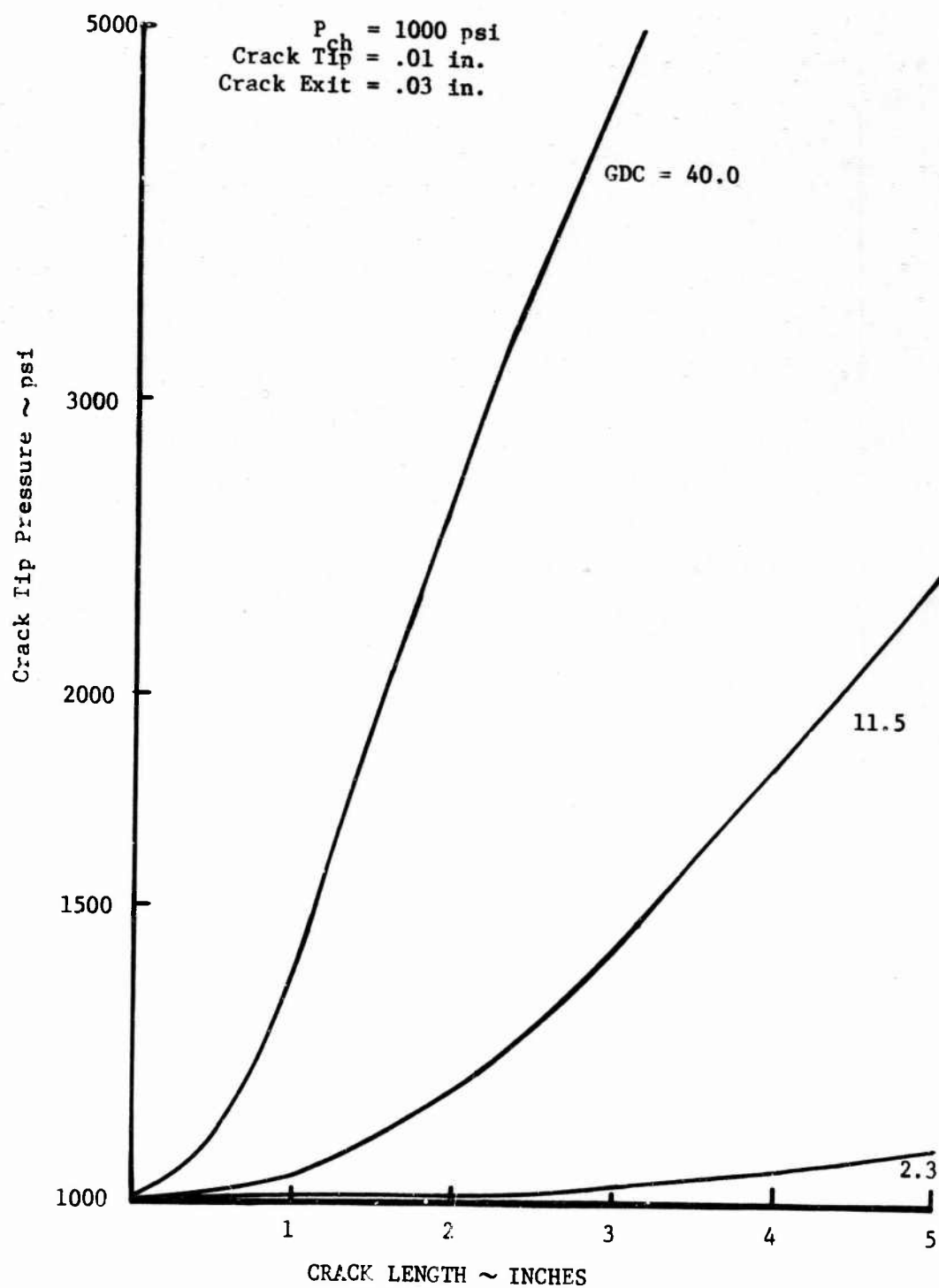
Figure 14. Crack tip pressure versus crack length for several propellants at constant tip and exit width
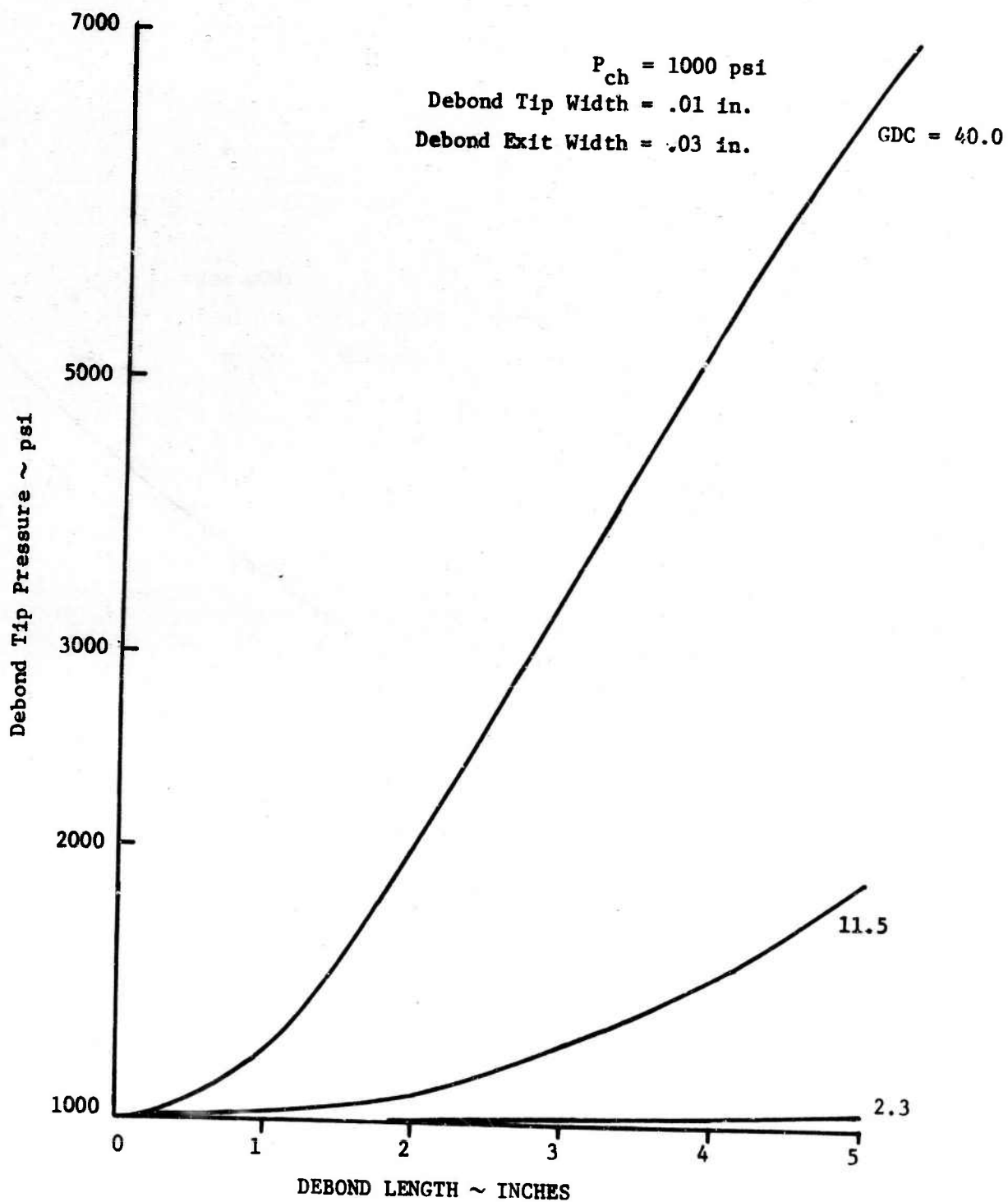
Figure 15. Debond tip pressure versus debond length for several propellants at constant tip and exit width
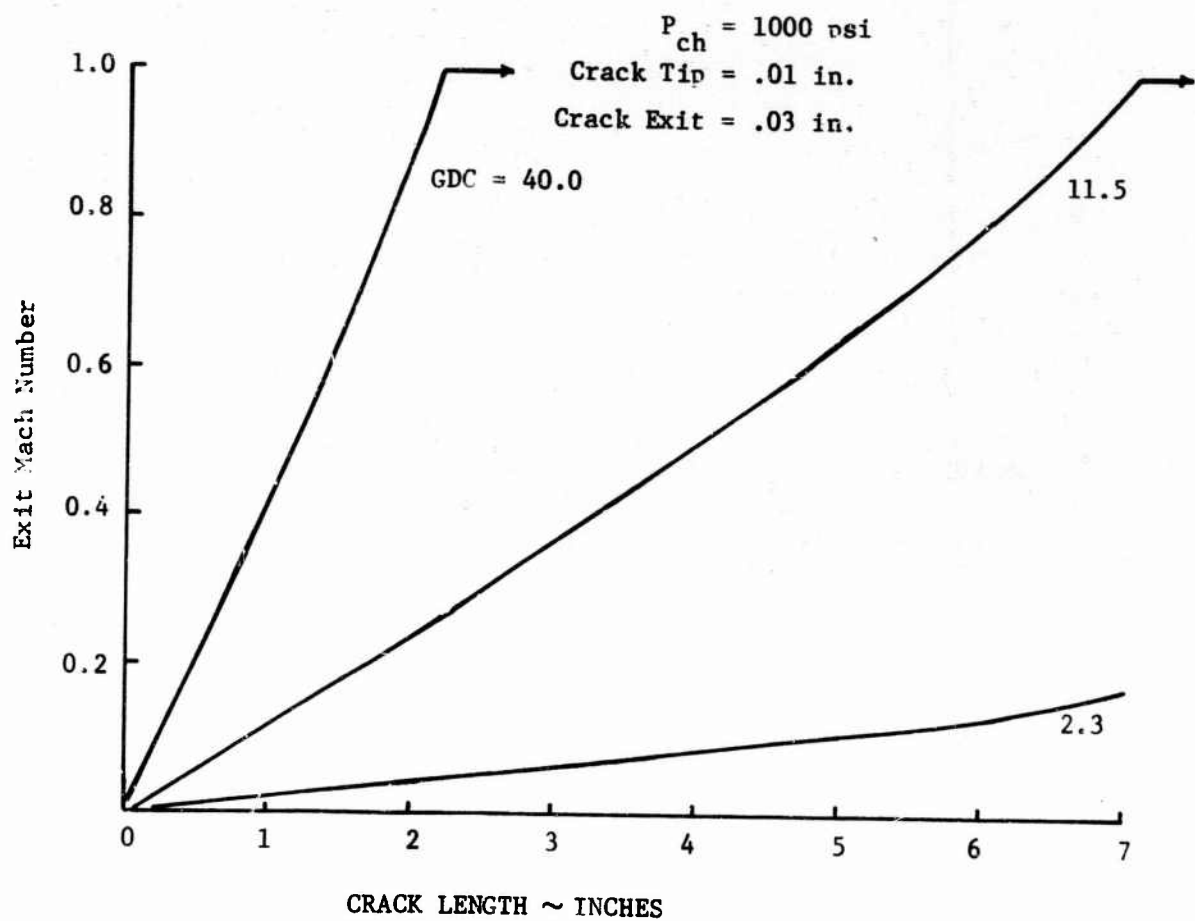
Figure 16. Exit Mach number versus crack length for several propellants
at constant tip and exit width
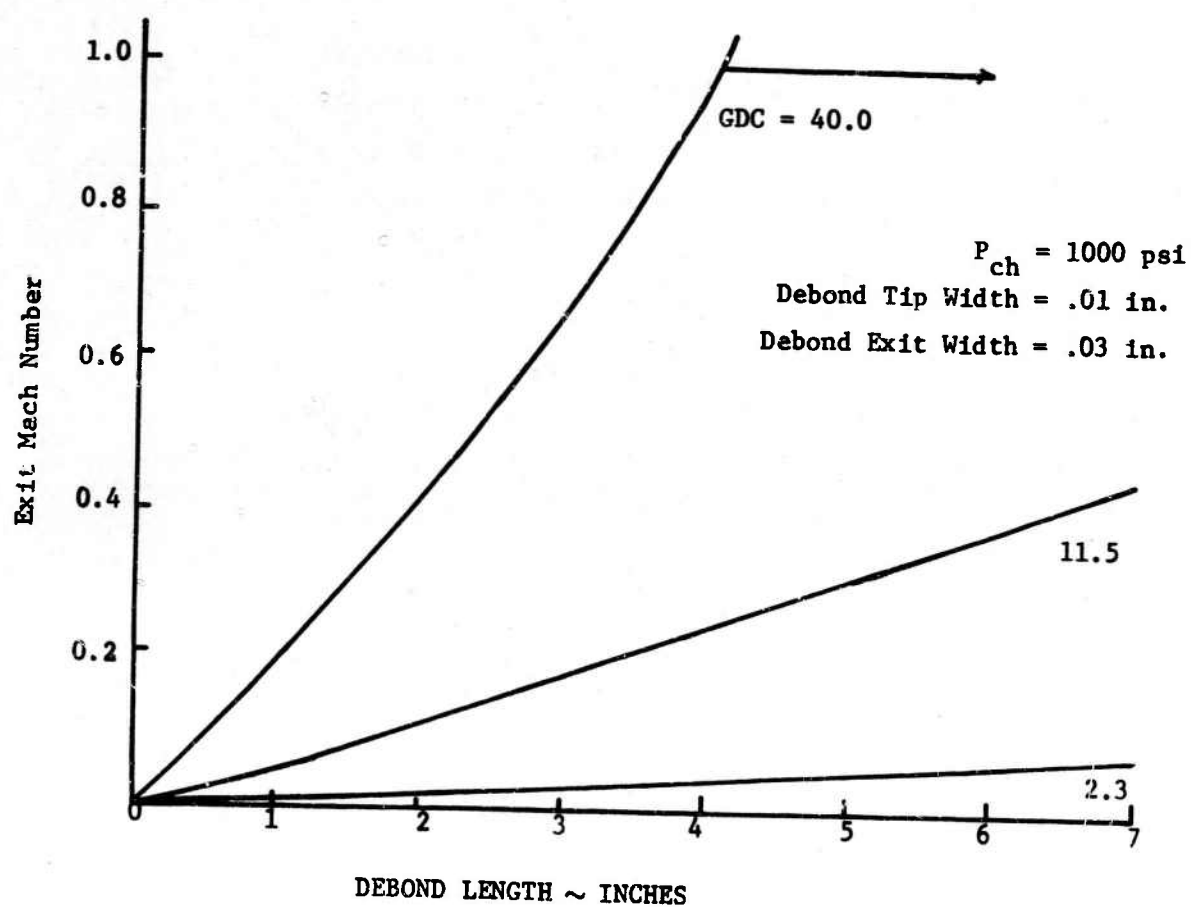
Figure 17. Exit Mach number versus debond length for several propellants at constant tip and exit width.
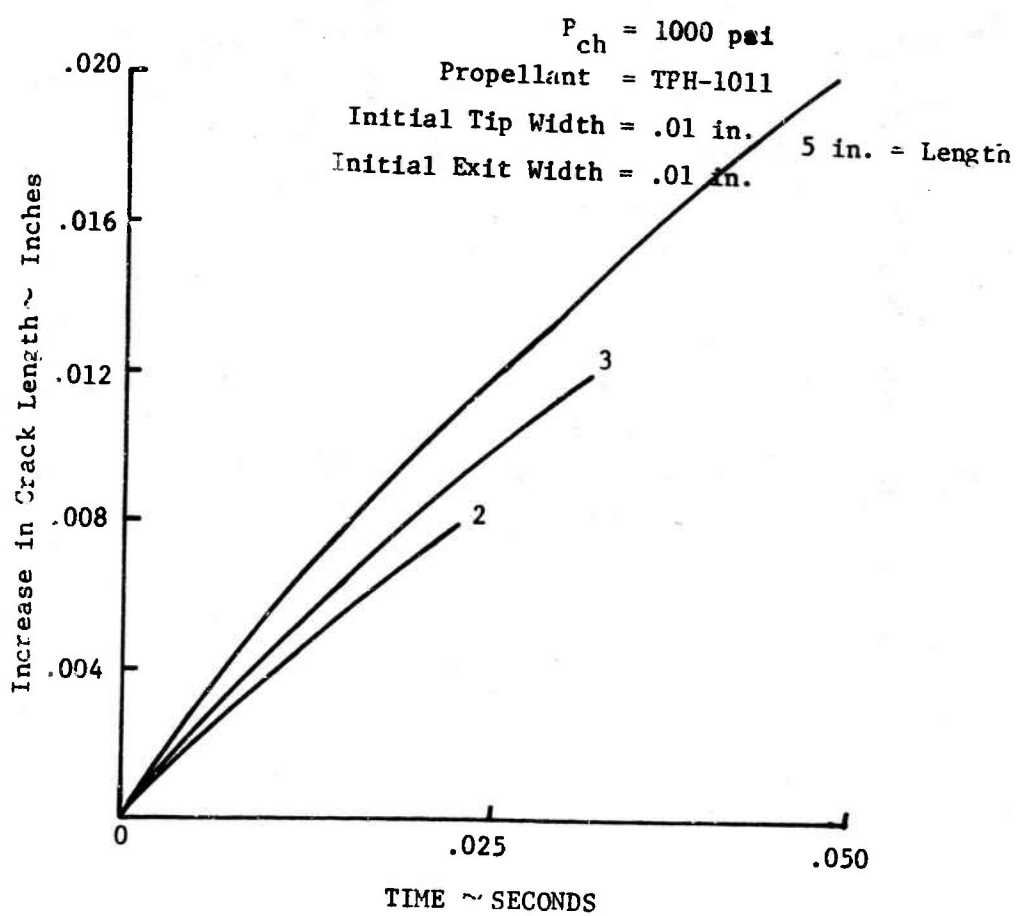
Figure 18. Increase in crack length versus time for several initial lengths.
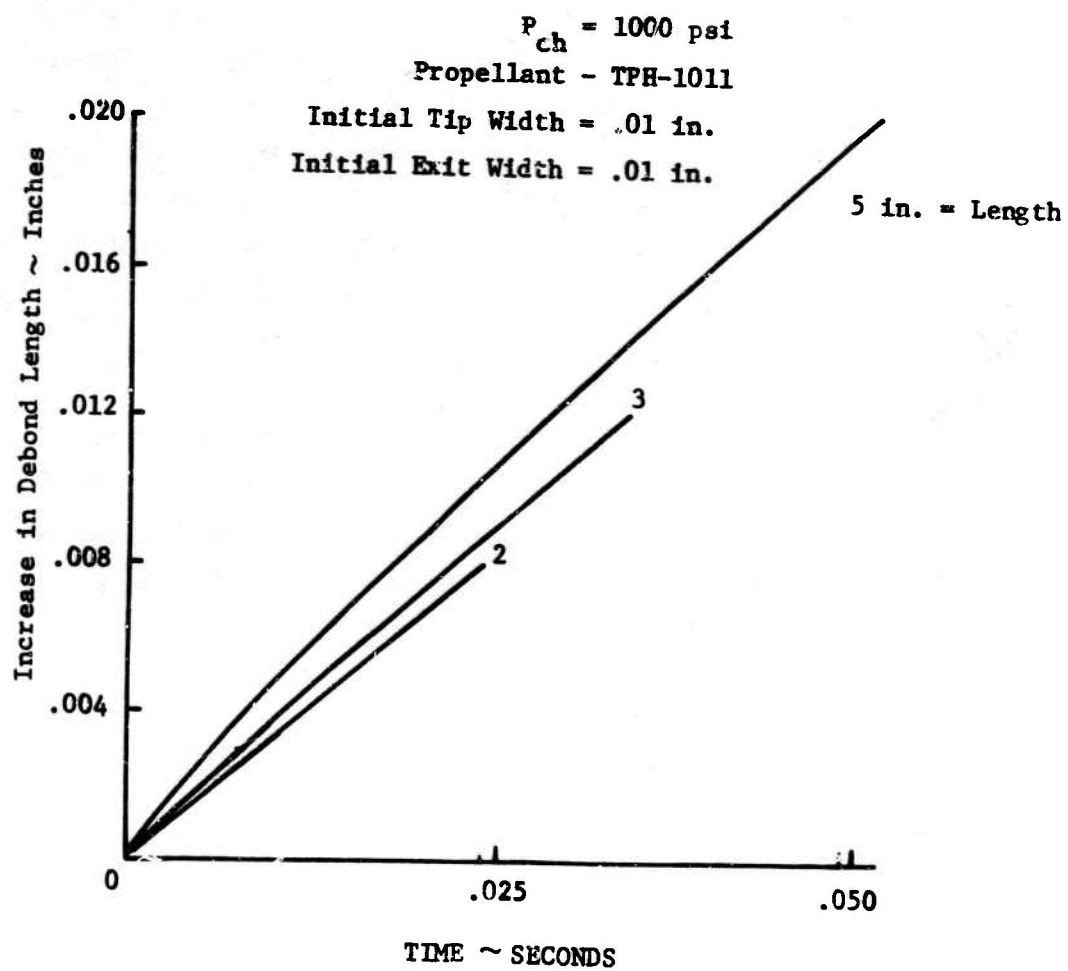
Figure 19. Increase in debond length versus time for several initial lengths.

due to burning alone can safely be said to be sufficiently slow so that it offers no great problem.

HALF-TIME FOR TIP PRESSURE VERSUS BURNING RATE COEFFICIENT

A characteristic of all burning flaws is that the pressure decreases rapidly with time due to the geometrical changes occurring. To illustrate this effect, Figures 20 and 21 indicate the time required to reduce the flaw tip pressure by a factor of two as a function of the coefficient, C, in the burning rate law. The burning rate law is that for TPH-1011 with coefficient changed. As would be expected, the half life drops off at a faster rate for the crack than the debond due to the fact that it is burning on both surfaces. Although extremely high pressures may exist initially in a flaw, the defect geometry changes at a near constant rate due to the small exponent in the burning rate law as can be seen in Figures 18 and 19.

EFFECT OF VARIABLE GEOMETRY, CIRCULAR DEBONDS

Figures 22 and 23 represent the types of situations which might result in a head-end debond around a rocket motor igniter. As can be seen, the smaller the igniter diameter, the greater the difficulty for equally deep debonds.
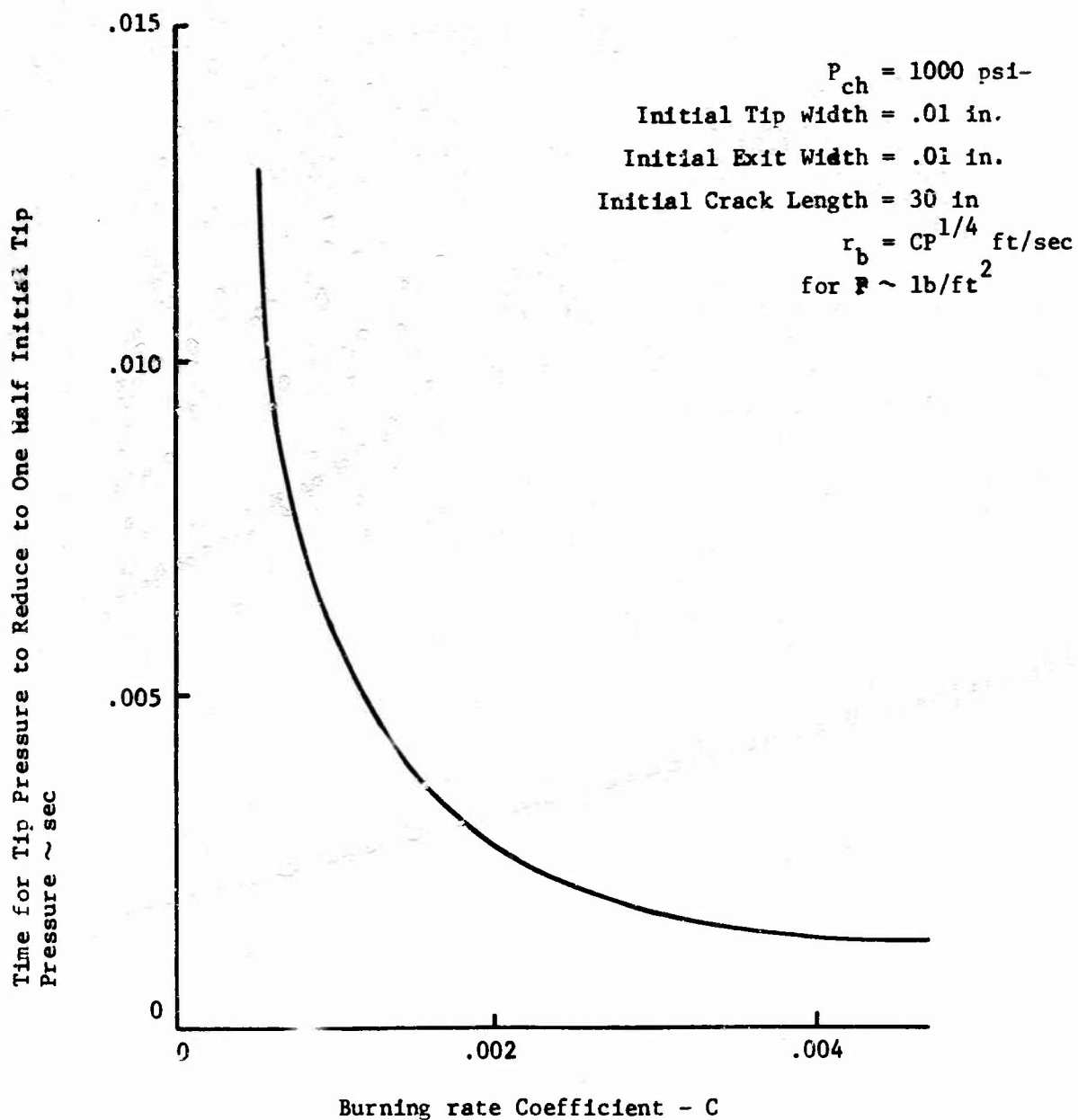
Figure 20. Time for tip pressure to reduce to half initial
pressure versus burning rate coefficient C for a given initial
crack geometry.
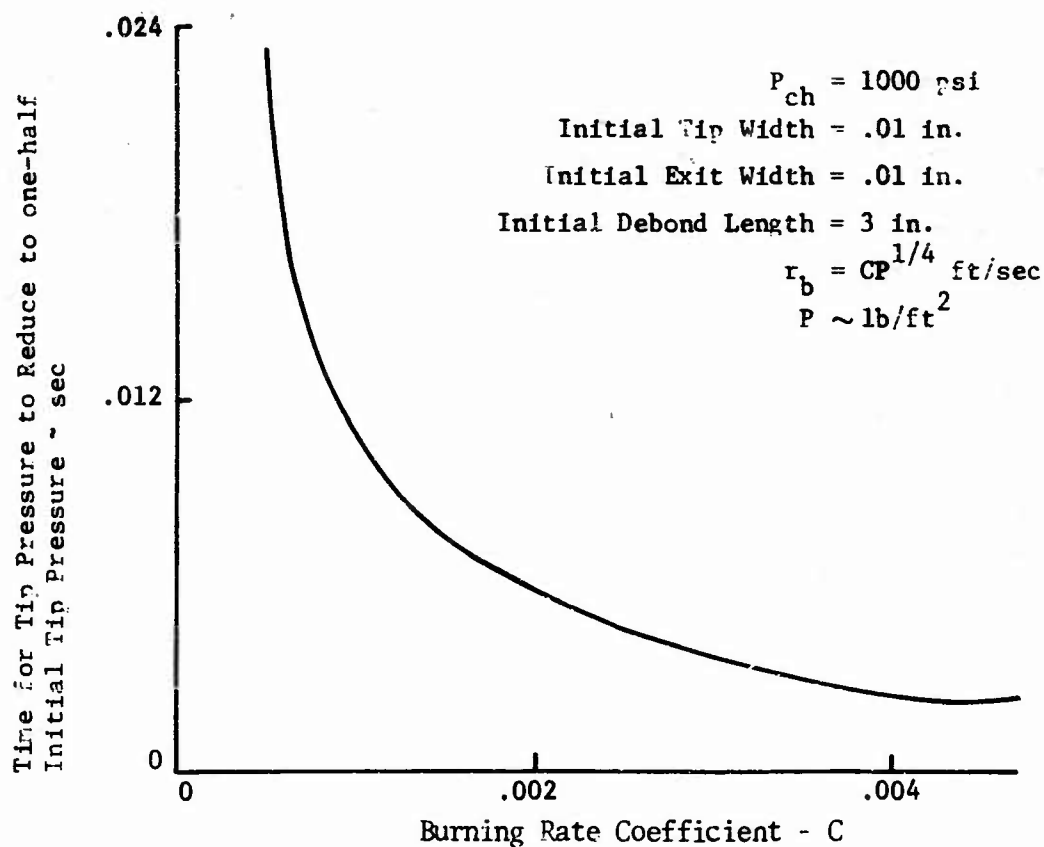
Figure 21. Time for tip pressure to reduce to half initial pressure versus burning rate coefficient C for a given initial debond geometry

The y-axis label: Time for Tip Pressure to Reduce to one-half Initial Tip Pressure ~ sec

The x-axis label: Burning Rate Coefficient - C

Figure annotations:

$P_{ch} = 1000$ psi

Initial Tip Width = .01 in.

Initial Exit Width = .01 in.

Initial Debond Length = 3 in.

$r_b = CP^{1/4}$ ft/sec

$P \sim lb/ft^2$
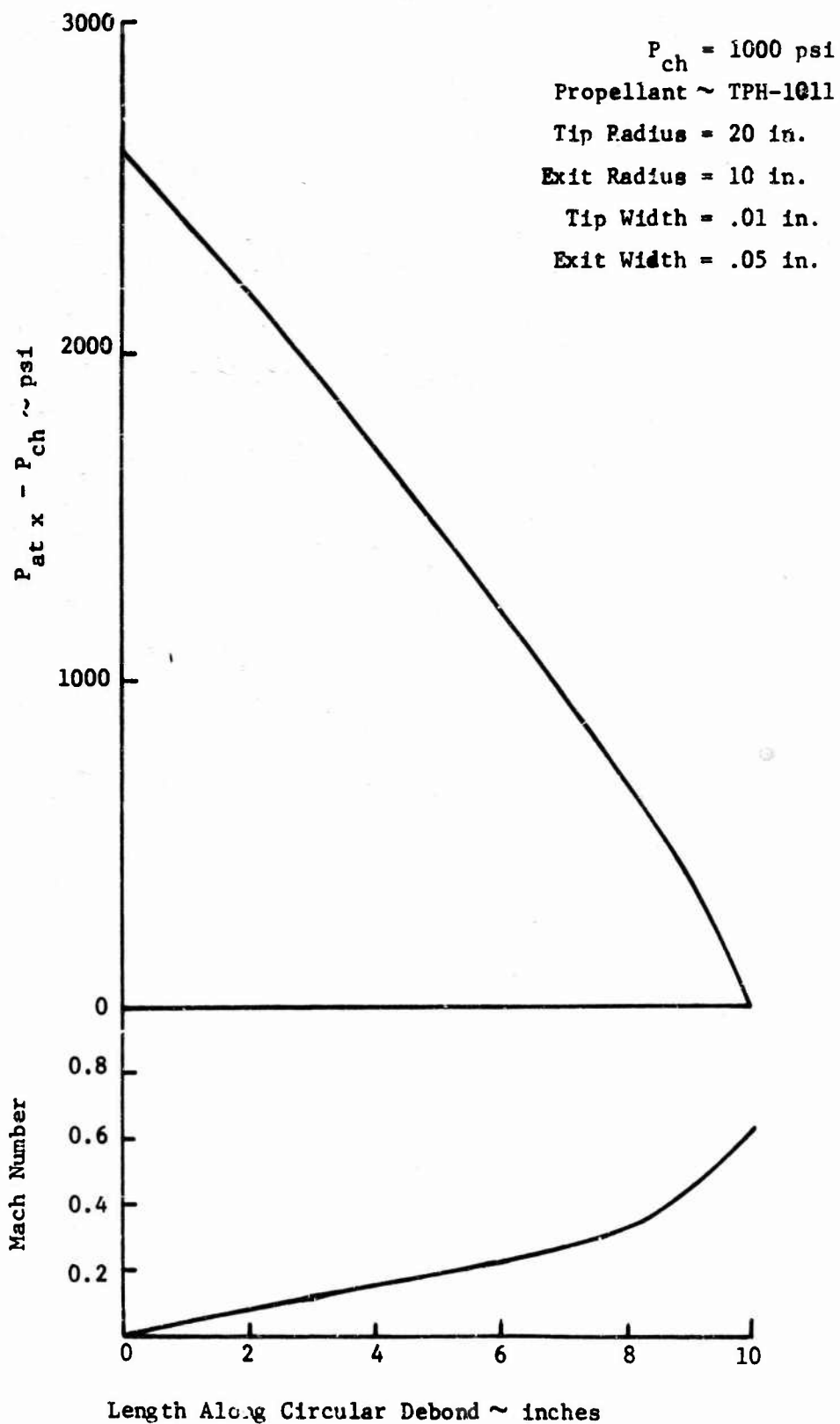
Figure 22. Pressure and Mach number distribution along circular debond
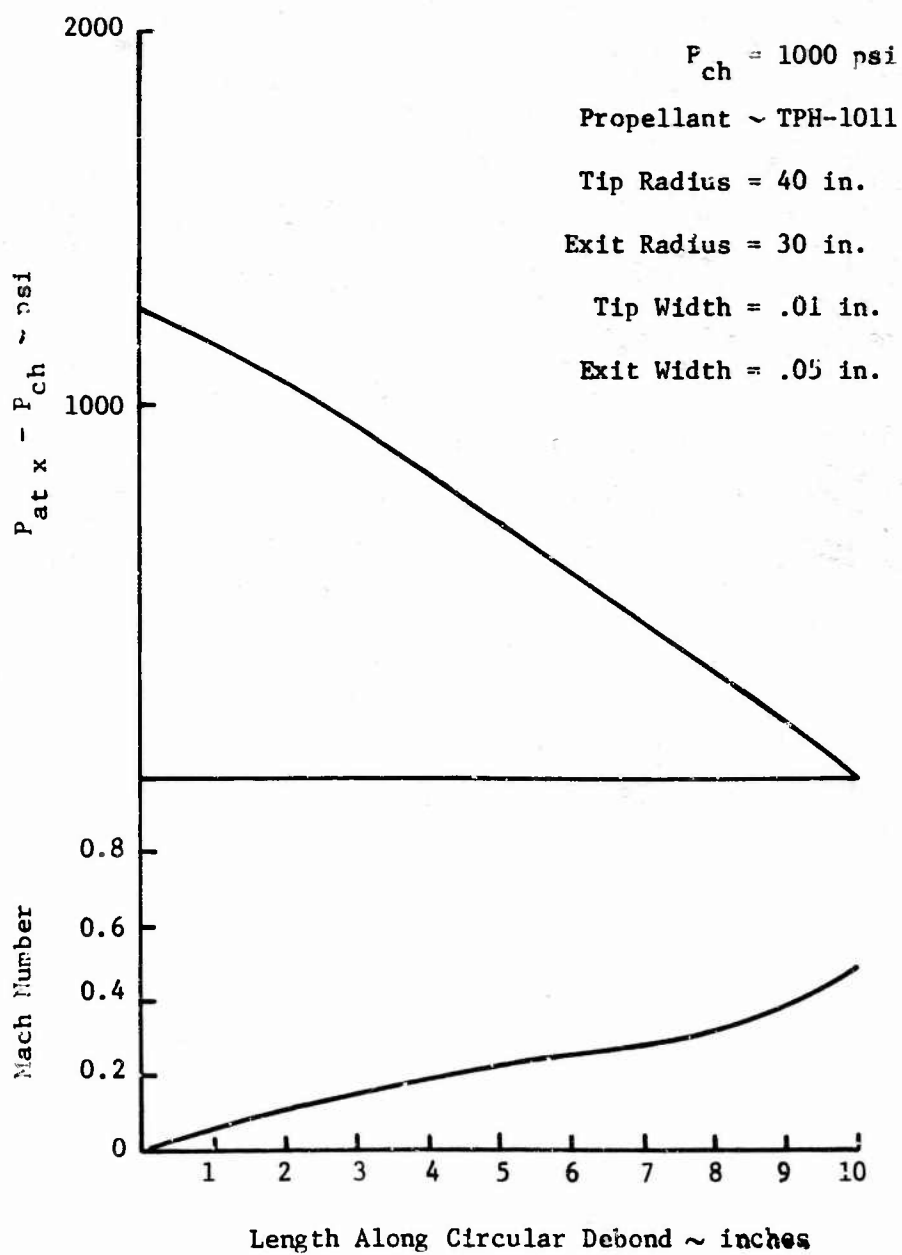
Figure 23. Pressure and Mach number distribution along circular debond

IV. TIME HISTORY OF FRACTURE OR DEBONDING IN VISCOELASTIC MATERIALS

Stated in perhaps its simplest form, the problem to be solved from the solid mechanics point of view is the following: given the geometric configuration of the crack or debond in the rocket grain and the pressure distribution inside this crack or debond, both as known functions of time, determine the instant at which fracture is initiated and, at least for small times, the time-history of the fracture. Stated in such a manner, the problem may appear to be a relatively simple one. Such, unfortunately, is not the case due primarily to the difficulties encountered in mathematically analyzing a body with a general cracked geometry. When the geometry changes with time as in this problem once fracture has been initiated, or the loads are applied to the grain dynamically, inertia effects may become of sufficient importance so that they can no longer be neglected. Thus, a new dimension of difficulty is added to the problem. Finally, it should be noted that the materials one must work with when investigating crack propagation in solid propellant rocket motors must be characterized, at best, as being linearly viscoelastic. Unlike elastic materials in which the stress is a function of strain alone, the rate dependency of viscoelastic materials means that the stress depends upon the entire time-history of the strain. This, of course, complicates the analysis still further.

Fortunately, however, the continuum theory of fracture has received a great deal of attention in this century since its beginnings in the classical work of Griffith [15] and much progress has been made due in large part to the improvement of mathematical techniques and the advent of the high speed computer. This progress has been largely concentrated in the areas of fracture of brittle elastic materials and more recently, of fracture of ductile elastic materials where the effects of plastic deformation in a region surrounding the crack tip are considered. However, with regard to the present study, it should be mentioned that a great deal of work has been done recently on developing methods of analysis for viscoelastic structures of uncracked geometries.

In addition, many of the concepts of fracture mechanics developed for
use with elastic materials are still valid for use with viscoelastic
materials.

Because of the noted lack of information available specifically on visco-
elastic fracture, an approach to the solid mechanics part of this program has
been chosen which is based upon the development and analysis of relatively
simple models capable of describing the important aspects of viscoelastic
fracture and debonding at least insofar as the viscoelastic dependence
is concerned. The information obtained in analyzing these models could
then be used to provide qualitative results in the prediction of fracture.
With these comments in mind, let us consider the progress that has been
made, first, in the field of cohesive fracture and then in the closely
related (from a continuum mechanics point of view) field of adhesive
debonding.

The first work to be mentioned is the investigation by Swanson[16]
of fracture in a linearly viscoelastic tubular rocket propellant grain.
In this study, the cylindrical grain was assumed to be of infinite
length and to have a radial crack at its centerbore running the full
length of the cylinder. Time-dependent critical stress intensity
factors $K_{1C}(t)$ were then used as criticality conditions for the cylinder
subjected to a time-dependent internal pressure loading.

The critical stress intensity factors $K_{1C}(t)$ to be used were
obtained from laboratory tests on specimens of Hercules Incorporated
designated EJC solid propellant. These specimens were in the form of
solid right circular cylinders one inch in diameter by three inches
long with a crack three-sixteenths of an inch deep machined circum-
ferentially around the specimen by knife blade on a lathe. Bonding
these specimens to rigid end plates, they were then subjected to
several constant rate tensile tests at various cross-head speeds. In
addition, a series of tests was also conducted in which the crosshead speed
was changed from one constant value to another during the course of the
test. In each of these tests the time to failure and the failure load
were recorded. From the load at failure, it was a simple matter to
calculate the stress intensity factor at failure from the analysis
given by Bueckner[17] for an elastic cracked cylindrical specimen.
Bueckner's results can be summarized as

$$K_1 = 6_{net}(\pi D)^{\frac{1}{2}} F(d/D) \tag{70}$$

where 6_{net} is the axial force divided by the net area of the notched section, D is the outside diameter of the specimen, d is the diameter of the notched section and $F(d/D)$ is a numerical factor listed in Reference 17. It is clear from Equation 70 and the elastic-viscoelastic correspondence principle that this stress intensity factor applies to the viscoelastic test specimens as well. Hence, plotting K_1 at failure, i.e. K_{1C}, versus the time to failure for the various tests performed, a plot of $K_{1C}(t)$ was obtained for the EJC propellant. This is shown in Figure 24.

Now if a viscoelastic analysis of a particular cracked structure of EJC propellant can be performed so that the time-dependent stress intensity factor $K_1(t)$ can be found, the time to fracture is given by the intersection of the $K_{1C}(t)$ and $K_1(t)$ curves. The difficulty here lies in the fact that since $K_{1C}(t)$ was plotted for constant loading rates, our predictions of time to fracture are necessarily restricted to structures undergoing at least an approximately constant loading rate. Fortunately, however, use of the spherical flaw model (to be discussed later in this section) and laboratory tests have shown the time-dependent critical stress intensity factor approach to be relatively insensitive to a wide range of fast-slow variable loading conditions.

Using a finite-element stress analysis method, a plane-strain elastic analysis was made for a radial crack at the centerbore of a tabular rocket propellant grain. The analysis was made to calculate the strain energy in the propellant for a crack depth one-half panel greater and one-half panel less than the actual crack depth under consideration. Having calculated each of these strain energies, the strain energy release rate with respect to crack surface area G_1 is then calculated from a finite difference approximation to the formula

$$G_1 = \frac{dU}{dA} \tag{71}$$

-51-
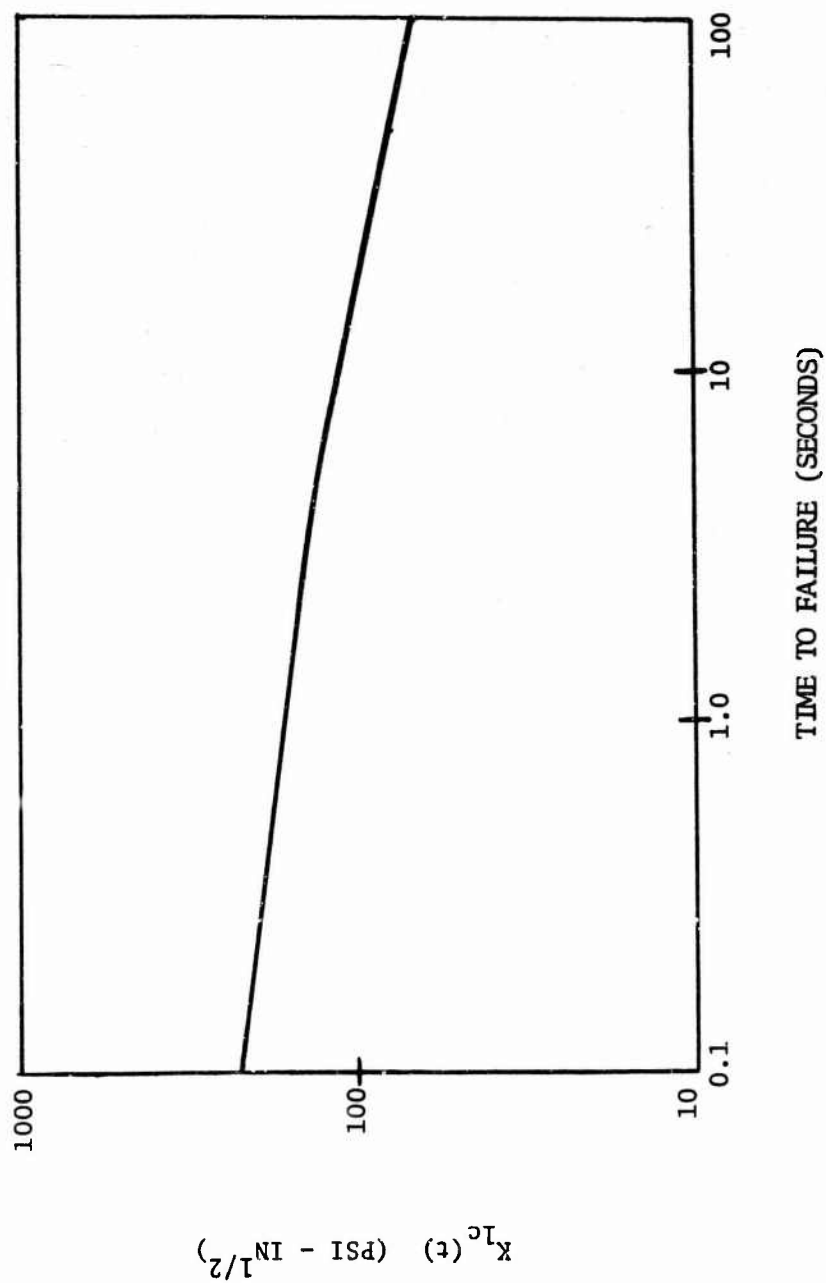
Figure 24. Plot of time-dependent critical stress-intensity factor $K_{Ic}(t)$.

-52-

where U is the strain energy and A is the crack surface area. Having calculated this expression, one can finally obtain the stress intensity factor K_1 as

$$K_1^2 = \frac{EG_1}{1-\nu^2} \qquad (72)$$

where E is Young's modulus and ν is Poisson's ratio.

Once having obtained the stress intensity factor for the elastic problem, it is possible to solve for the time-dependent stress intensity factor $K_1(t)$ for the corresponding viscoelastic problem through the use of Schapery's quasi-elastic approximation [18]. In fact, this results in

$$K_1^2(t) = \left(K_1^2\right) \left(\frac{E_{rel}(t)}{E}\right) \qquad (73)$$

where $E_{rel}(t)$ is the stress relaxation modulus, if the internal pressure is applied as a step function in time. When the pressure does not vary with time in this manner but in some more general way, the fact that we are considering a linear viscoelastic material and that K_1 is a linear function of the applied pressure loading, allows one to use Equation 73 with the Duhamel integral to obtain $K_1(t)$ for this more general time-varying pressure loading. Plotting the resulting $K_1(t)$ for a particular time-varying internal pressure on the same graph with the $K_{1C}(t)$ curve obtained from the laboratory tests on cracked specimens, the time to failure is predicted as the point of intersection of the two curves.

To verify the analytical work, a high-rate hydrotest was conducted on a structural test vehicle (STV) containing a radial crack. Crack propagation was produced during the test and the time of its initiation was obtained from instrumentation recordings of grain deflections and the pressure rate. The measured pressure-time curve was then used in the previously mentioned finite-element analysis of a viscoelastic grain to obtain the time-dependent stress-intensity factor for the STV. This calculated $K_1(t)$ curve was plotted in Figure 25 along with the

experimentally obtained $K_{1C}(t)$ curve. The irregularity in the $K_1(t)$ curve was believed to be caused by entrapped air in the hydraulic system. The intersection of the two curves in Figure 25 is the predicted time to failure and is seen to be within five per cent of the observed time to failure.

Although in the one test conducted the stress intensity factor approach outlined above was quite successful in predicting the time to failure, two limitations of this method do arise. The first is that a uniform pressure distribution was assumed to act within the crack whereas the analysis of Section III shows that the actual pressure distribution in a burning crack is non-uniform. The effects of such a non-uniform pressure distribution on crack instability can be estimated, however, by the results of Appendix C, thus causing no substantial difficulties. A more serious objection is that the critical stress intensity factor approach is not applicable to the second part of our problem; that is, the prediction of initial velocities of propagation. Hence, we have considered a more general approach to the problem based on the thermo-dynamic power balance. This balance can be written as

$$\dot{I} = \dot{F} + 2\dot{D} + \dot{SE} + \dot{K} \tag{74}$$

where $\dot{I}$ is the power input of the applied loading at the boundaries of the system, $\dot{F}$ is the rate of increase of the free (strain) energy, $2\dot{D}$ is the dissipation, $\dot{SE}$ is the rate of increase of the surface energy and $\dot{K}$ is the rate of increase of the kinetic energy. In principle, this power balance can be applied directly to any crack configuration, loading and material of interest. In practice, however, computational difficulties are encountered in the application of the power balance to realistic geometries and materials. This has led us to consider William's model [19] of a spherical flaw which incorporates a simplified crack geometry and the power balance Equation 74 to predict both the

-54-
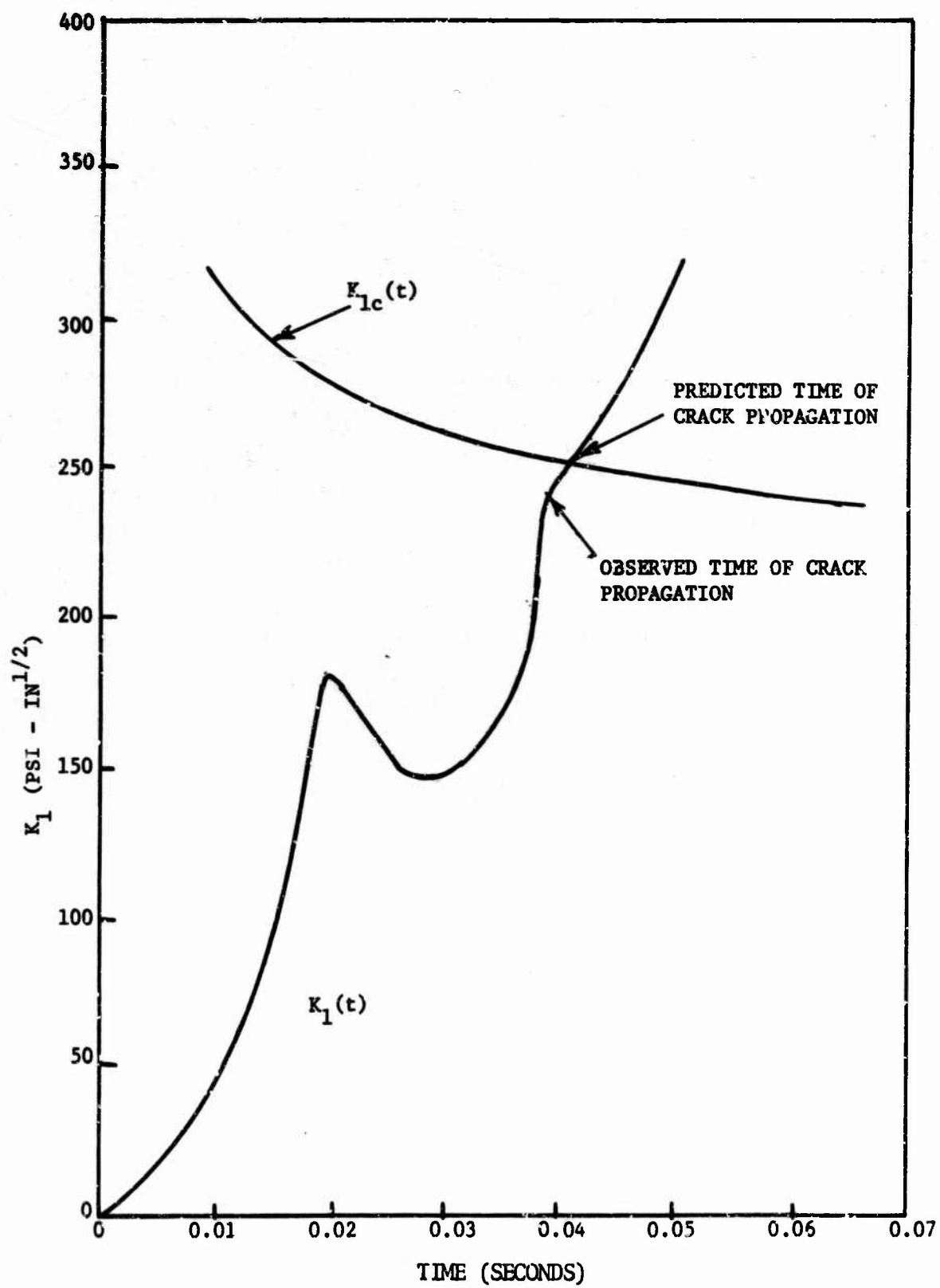
Figure 25. Comparison of predicted and observed crack
propagation in pressure test of STV.

-55-

time to fracture and its initial velocity of propagaticn. Aside from the relative ease with which one can calculate the various terms of the power balance (Equation 74) for this geometry, further motivation for studying the spherical flaw was provided by the fact that the criticality condition for the elastic case is extremely similar to that found for the more realistic crack geometries of Griffith[15] or Sneddon[20]. Since this model has been extensively investigated in the literature, it is sufficient here only to outline its important features as regards this study.

In his original work on the spherical flaw, Williams[19] neglected inertia effects and considered the surface of the flaw to be stress free while subjecting the outer boundary of the hollow sphere to four typical inputs, namely, constant stress or displacement and constant stress or displacement rate. For each of these four loadings he was able to arrive at an expression from which to calculate the time to fracture. However, for this simple model difficulties were encountered in solving the nonlinear integral equation for the time history of the flaw growth. For example, an initial velocity of propagation was found for the case where the outer sphere boundary was subjected to a constant displacement rate, but in the limiting case of instantaneous propagation, that is, time to fracture $t_f = 0$, this initial velocity was discovered to be infinite. This rather unrealistic result was attributed to the fact that inertia effects were neglected in the analysis. Although this omission may cause little error in a highly viscous material subjected to slow loading rates, this will not be the case in more elastic materials or when the applied loading rates become appreciable. This was, in fact, borne out by a subsequent analysis[21] of the spherical flaw in which the kinetic energy contribution to the power balance was included. Here it was shown that, for the case of a constant displacement rate loading at the sphere's outer boundary, the power balance fracture criterion predicted a zero initial velocity of propagation of the flaw when fracture was initiated instantaneously. Thus, the effect of including the kinetic energy in this particular example was to exhibit a smooth transition during the acceleration from zero initial flaw velocity.

-56-

Because of its wide applicability and its ability to predict the time-history of fracture, the energy balance will be applied as the criterion for fracture in our further studies. Thus, the spherical flaw has served several useful purposes toward this end. Namely, it has provided us with a better understanding of the subtleties of applying the power balance; it has given us some qualitative insight into the behavior of crack propagation in linearly viscoelastic materials; it has also provided (see Section V) several useful estimates regarding times to failure and the magnitudes of initial crack propagation velocities in burning rocket grains, All of these will be of benefit as more sophisticated models are developed and solved in the process of obtaining the final desired quantitative results.

Unlike the field of cohesive fracture, little work has been done in the field of adhesive fracture (debonding) from a continuum mechanics approach, even for the case of bonded elastic materials. In fact, it was only recently pointed out that since real adhesive interfaces, like real materials, contain small cracks (debonds) which give rise to stress concentrations, the Griffith approach to cohesive fracture could then be extended to the study of adhesive debonding. Williams[22], for example, showed that when using the power balance as a criterion for crack propagation, the only difference mathematically between the phenomena of cohesive fracture and adhesive debonding is in the interpretation of the energy required to create new free (cohesive or adhesive) surface area.

To this date, continuum mechanics studies of adhesive failure have centered almost entirely on studies of the mathematical singularities which occur at the tip of cracks along an interface of two dissimilar media [23-24] or on methods for the experimental determination of the energy required to create new free adhesive surface area, γ_a [25-26]. These two points are worthy of further discussion.

As for the case of cracks in a homogeneous solid, the stress singularities at the tip of a crack along the interface of two dissimilar media can be found by the linear theory of elasticity. However, in the general case of arbitrary material constants the singularities are not solely of the square root type as they are for

-57-

cracks in homogeneous media, but are found to oscillate rapidly near the
crack tip. For example, the stresses are of the form[27]

$$\delta_y = -\frac{1}{\sqrt{r}} \left[A_0 \cos(\beta \, \ell n \frac{r}{a+r}) - B_0 \sin(\beta \, \ell n \frac{r}{a+r}) \right] + 0(1) \qquad (75a)$$

$$\delta_{xy} = -\frac{1}{\sqrt{r}} \left[A_0 \sin(\beta \, \ell n \frac{r}{a+r}) + B_0 \cos(\beta \, \ell n \frac{r}{a+r}) \right] + 0(1) \qquad (75b)$$

for the case of a bond line subjected to both tension and in-plane shear.
In Equation 75, β is defined by

$$\beta = \frac{1}{2\pi} \, \ell n \left[\frac{\mu_1 + \mu_2(3 - 4\nu_1)}{\mu_2 + \mu_1(3 - 4\nu_2)} \right] \qquad (76)$$

A_0 and B_0 are stress intensity factors, r is the distance from the
crack tip along the interface, a is the crack half length, μ and ν are
the shear modulus and Poisson's ratio, respectively, and the subscripts
one and two refer to the different materials on either side of the debond.
Note that for the special case where the debond occurs at the interface
between a rigid material and an incompressible one, that is $\mu_2 = \infty$ and
$\nu_1 = 0.5$, no oscillations occur. Because of the trig-log behavior of the
stresses in the general material case, one cannot rigorously compute
the strain energy directly. However, as a practical matter, the
oscillating singularity is disregarded [28].

The experimental determination of the energy required to create
new free adhesive surface area, γ_a, has been the subject of much
discussion and several methods have been proposed. Perhaps the best
of these methods, however, from the combined viewpoint of experimental
convenience and ease of mathematical modeling, is Williams'[28] modifica-
tion of a method originally proposed by Dannenberg [26]. In this
"pressurized blister test," a thin disk layer of soft material is cast
and cured upon a relatively rigid base plate except for a central

-58-

circular portion which is prevented from bonding. Pressure is then introduced into this unbonded region causing the thin disk layer to lift up off the base plate in a fashion similar to a blister. The radius of the unbonded region remains constant as the pressure is slowly increased until a certain critical pressure level is reached. At this time the radius enlarges, signifying an adhesive failure (debonding) along the interface of the disk and base plate. Modeling the system mathematically and applying the energy balance results in a relationship between the material properties of the disk, the critical pressure and γ_a. This result, combined with the experimental data, allows one to arrive at a value for γ_a.

Since the experimentally determined values of γ_a are critical to the successful use of the power balance in predicting adhesive debonding, it is imperative that these values be as accurate as possible. This accuracy, however, aside from laboratory techniques, is heavily dependent upon how well the mathematical model of the blister test can be made to conform to the actual experimental setup. Thus, some effort has been expended in developing more sophisticated mathematical models of the blister test to replace the original analysis. In this first analysis [22] the thin, flexible disk layer was modeled by linear elastic plate theory while the base plate was considered to be rigid. Since then two more sophisticated models have been made. The first[29] used non-linear, large deflection plate theory to evaluate the effects of large deflections of the disk layer while the second[30] was concerned with the case of two materials bonded together by a third rather than one being cast directly upon the other. Let us investigate each of these models further.

It can easily be shown using linear elastic plate theory and the power balance equation (again neglecting inertia effects) that the energy required to create new free adhesive surface area in a blister test is given by[29]

$$P_{cr}w_0 = 2\gamma_a \tag{77}$$

where p_{cr} is the pressure needed to initiate the debonding and w_0
is the center deflection of the blister at the time debonding starts.
Thus, values of γ_a can be obtained from laboratory blister tests by
simply recording the pressure and central deflection of the disk at the
time the debond begins propagating. A plot of p_{cr} versus w_0 is shown
in Figure 26 for a test run on polyurethane cast and cured onto a
polished glass plate. It is noted in this plot that for small center
deflections the fracture initiation points fall quite closely along
a hyperbola of parametric value $2\gamma_a$. However, for larger deflections
this is no longer the case due to the inability of linear plate theory
to account for the midplane stretching in the polyurethane specimen.
Performing a membrane analysis and again using the power balance, we find
that if the membrane stresses are such that they overshadow the bending
stresses, γ_a is given as

$$p_{cr}w_0 = 2.4\gamma_a \tag{78}$$

Thus for larger center deflections, the plot of fracture initiation
points in Figure 26 should fall on a hyperbola of parametric value $2.4\gamma_a$.
This is seen to be the case. In the transition between linear plate
theory and membrane theory, an approximate solution by Berger[31] can
be used to include the effects of both plate bending and stretching.
In this case, the use of the power balance results in a complicated
expression from which to find γ_a. This expression must be solved
numerically.

The effects on the experimentally determined values of γ_a due to
the thickness of two materials being bonded together by a third have
been investigated[32] by approximating the interlayer as a Winkler-type
elastic foundation. Using for the analysis the standard blister test
configuration with the addition of the interlayer, an application of
the power balance results in an expression for γ_a which can be written
in the form

$$\gamma_a = \frac{p_{cr}^2 a^4}{128D} [1 + f(\lambda_a)] \tag{79}$$
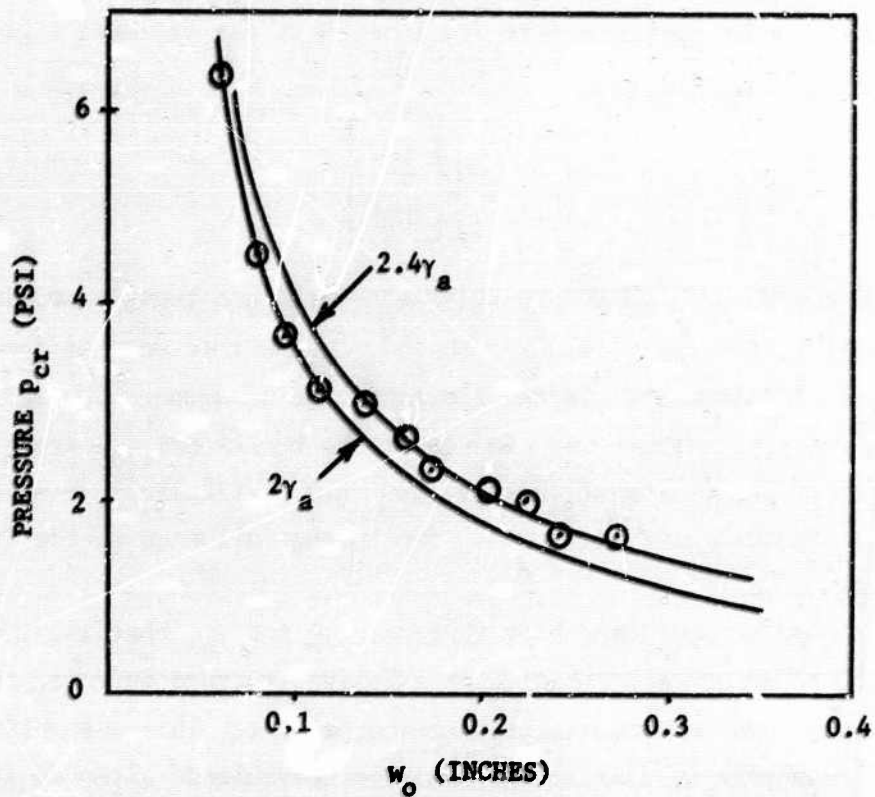
-60-

Figure 26. Plot of critical pressure versus center deflection from a blister test of polyurethane cast and cured on a glass plate.
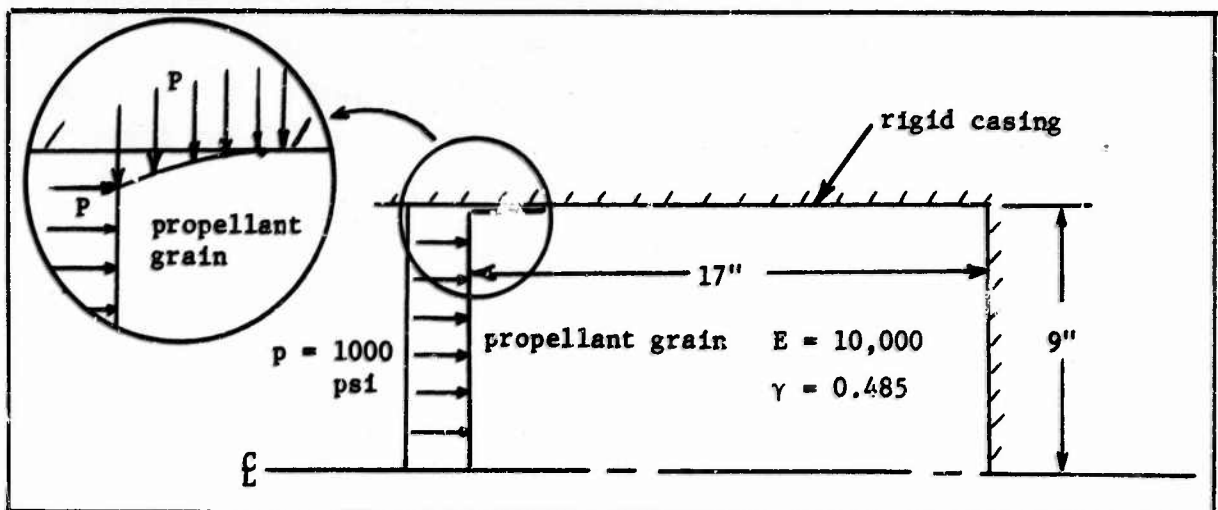
Figure 27. Configuration of end loaded rocket propellant grain debonding axisymmetrically from rigid casing.

where p_{cr} is the pressure at the instant of fracture initiation, a is the radius of the debond before fracture, D is the flexural rigidity of the plate and

$$\lambda^4 = \left[\frac{1 - \nu^1}{(1 - 2\nu^1)(1 + \nu^1)}\right]\left[\frac{E^1}{4Dh^1}\right] \tag{80}$$

In Equation 80, ν^1 and E^1 are Poisson's ratio and Young's modulus, respectively, for the interlayer and h^1 is the thickness of the inter-layer. It is clear that in the limiting case of a vanishing interlayer, i.e. $h^1 \to 0$, we have $\lambda \to \infty$. Values of the function $f(\lambda_a)$ are given in Table I. An inspection of these values (in particular $\lambda_a = \infty$) shows that $f(\lambda_a)$ is the correction to γ_a due to the influence of the interlayer thickness.

It should be mentioned here that both γ_c and γ_a, that is, the energy necessary to create new cohesive or adhesive fracture surface, respectively, have usually been assumed to be time-independent. This assumption was imposed primarily as a matter of analytic convenience although it has been widely recognized that this is not the case [33-34]. The time dependence of γ_a and the slow growth of adhesive fracture observed in the blister tests that have so far been made, suggest that time-dependent dissipative mechanisms take place during fracture. Thus, a further refinement in the mathematical model of the blister test is still necessary in that the thin, flexible disk layer must be modeled as being viscoelastic. Work is proceeding in this direction.

Assuming the same materials and surface preparation as were used in the experimental determination of γ_a, one can use this now known value of γ_a to predict adhesive debonding in a specimen of different geometry under different loading conditions if one can solve this problem for the potential energy release rate with further debonding. For example, a rather idealized problem of adhesive debonding in a case-bonded solid propellant rocket motor has been investigated [29] as an illustration of the approach to be used. The idealization considered is that of a finite length, elastic solid propellant grain debonding in an axially

-62-

symmetric manner from one end of its enclosing rigid case. The end
opposite the finite length debond is considered to be fixed and the grain
is assumed to be solid (100 per cent web fraction grain). The end of the
grain where the debond takes place is subjected to a normal pressure which
also acts in the debonds and the dimensions and material properties are as
shown in Figure 27. If we further assume that the kinetic energy of the
system can be regarded as being negligible, the power balance relation
can be written using Clapeyron's theorem [35] as

$$\frac{\partial U}{\partial A} = \gamma_a \tag{81}$$

where U is the strain energy of the system and A is the surface area of
the debond. Thus, the problem becomes one of finding the variation of
the strain energy with respect to changes in the debond area. For the
geometry shown, this has been accomplished using the finite element
method for each of several debond lengths. The results of the analysis
are shown in Figure 28 where the strain energy is plotted against the
debond area. The inverse square root of the slope of this curve was
then used with Equation 81 to produce the parametric design curve
shown in Figure 29. This curve represents the debonding failure
criterion for end pressure loadings on an axisymmetric elastic rocket
grain bonded to a rigid casing.

Since it is well-known that most solid rocket fuels are at best
linearly viscoelastic, the above analysis would be improved considerably
by assuming the grain to be a linear viscoelastic material. Although
it is again theoretically possible to calculate the quantities necessary
for use with the power balance, the viscoelastic nature of the grain
causes the stress and strain fields to be time-dependent, thereby
complicating the analysis considerably. In this case Equation 81
is no longer applicable. Rather we must employ the more general version
of the power balance as given by Equation 74. If the various terms of
this equation could then be calculated, the use of the power balance as
a criticality condition would result in an expression from which one
could obtain the entire time-history of the debond.
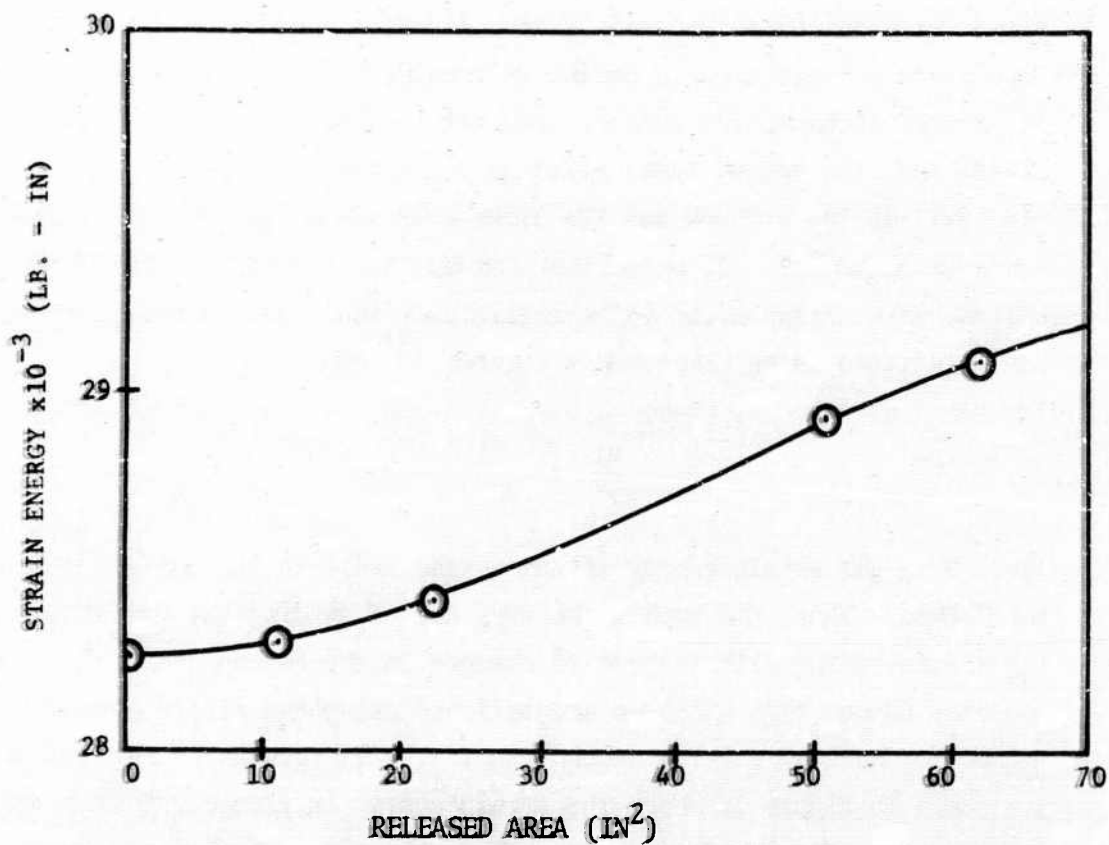
Figure 28. Plot of strain energy versus debond area for end loaded rocket propellant grain debonding axisymmetrically from rigid casing.
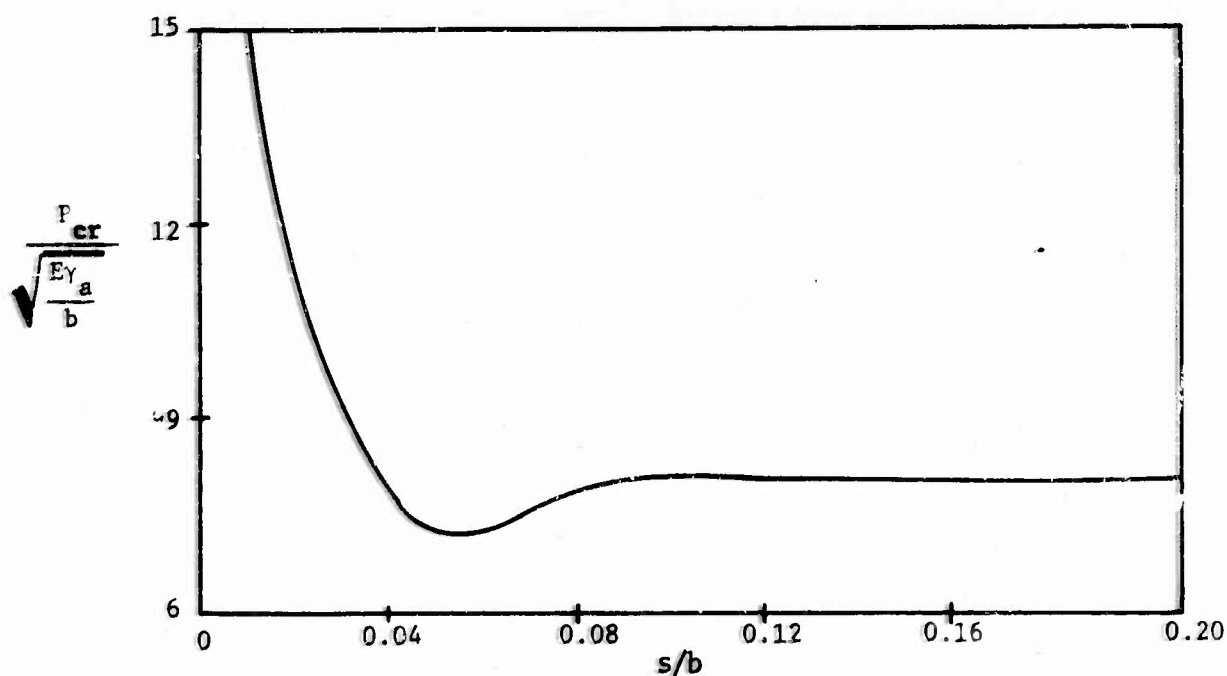
Figure 29. Critical pressure versus crack length for bond failure where s = crack length and b = radius of propellant grain.
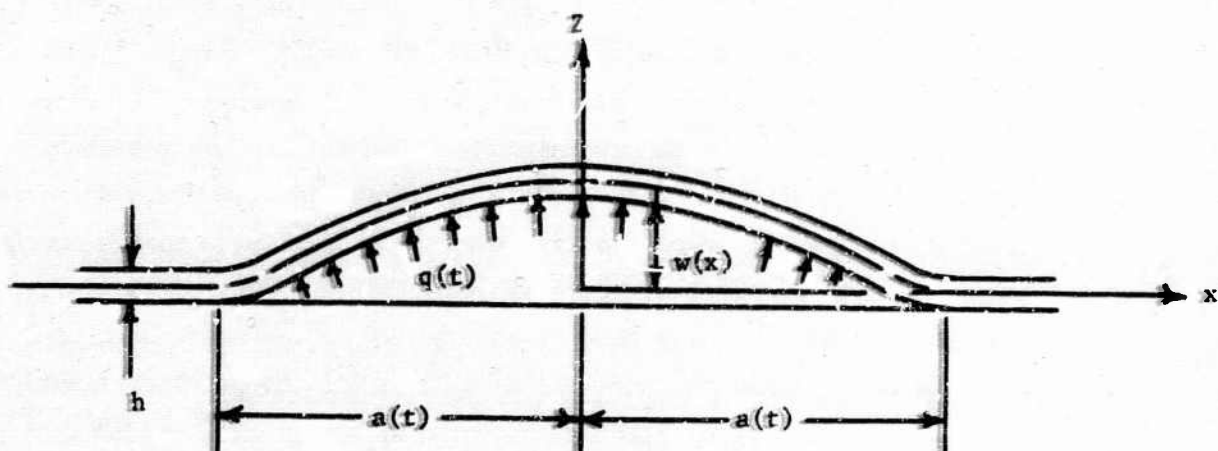
Figure 30. Configuration for simplified debond model.

λa	f(λa)
5.0	0.178
7.5	0.139
10.0	0.107
15.0	0.071
22.5	0.046
∞	0.000

Table 1. Interlayer correction functions.

-65-

Whereas the application of the power balance in predicting the
fracture threshold is reasonably straightforward, the calculations
necessary for its use are often prohibitive for the general debond
geometry. As indicated in the preceding paragraph, this is especially
true when the problem is further complicated by including the effects
of viscous dissipation as one should when considering viscoelastic
materials. Thus, as in the case of the spherical flow model developed
to study cohesive fracture in viscoelastic materials, a simple model
has been devised which, it is felt, leads to at least representative
results for the debonding process insofar as viscoelastic dependence
is concerned. Since the analy... this model demonstrates clearly
many of the principles that ha.... a discussed in this section, it
is appropriate to include the analysis at the present time.

Consider a linear viscoelastic beam of infinite length which is bonded
to a rigid substrate along its entire length with the exception of a
portion of length $2a_0$ which has debonded. A stationary, rectangular
Cartesian coordinate system x, y, z is oriented as shown in Figure 30 so
that the origin is at the center of the debond and the x-axis coincides
with the axis of the beam. At time $t = 0$, a pressure $q(t)$, where
$q(t) \equiv 0$ for $t < 0$, is applied within the debond causing it to propagate
symmetrically at some time $t_f \geq 0$ so that the edges of the debond are
at $|x| = a(t)$ for all times. Clearly for $t \leq t_f$ the relationship
$a(t) = a_0$ is satisfied. Neglecting inertia effects and using beam
theory, it is a simple matter to solve for the beam deflection w and
the stress 6_x and strain ε_x within the beam. Because of the viscoelastic
nature of the beam material, these quantities are functions of time and
are given by

$$w(x, t) = \left[\frac{[x^2 - a^2(t)]^2}{24I_y}\right] \left[L^{-1}(t)\right] \tag{82a}$$

$$6_x(x,t) = \frac{-q(t)\,z}{6I_y}\,[3x^2 - a^2(t)] \tag{82b}$$

$$\varepsilon_x(x, t) = \left[\frac{-z[3x^2 - a^2(t)]}{6I_y}\right] \left[L^{-1}(t)\right] \tag{82c}$$

-66-

where

$$L^{-1}(t) = L^{-1}[\bar{q}(S)\, S\, \bar{D}_{crp}(S)] = q(t)D_g + \int_{0^+}^{t} \frac{\partial D_{crp}(t-\tau)}{\partial(t-\tau)}\, q(\tau)d\tau \qquad (83)$$

and I_{y_1} is the moment of inertia of the beam cross-section about the y-axis and L^{-1} denotes the inverse Laplace transform. In equation (83), the bar over a function denotes the Laplace transform of that function, S is the transform parameter, $D_{crp}(t)$ is the creep compliance of the material and D_g is defined as $D_g \equiv D_{crp}(0^+)$.

As a criterion for debonding of the beam, an application is made of the thermodynamic power balance which, neglecting the kinetic energy, can be written as

$$\dot{I} = \dot{F} + 2D + \dot{SE} \qquad (84)$$

where, for the present problem,

$$\dot{I} = 2\frac{d}{dt}\int_0^{a(t)} dx \int_{-\infty}^{t} q(\tau)\frac{\partial w(x,\tau)}{\partial \tau}\, d\tau \qquad (85a)$$

$$\dot{F} + 2D = 2\frac{d}{dt}\int_{-h/2}^{h/2} dz \int_0^{a(t)} dx \int_{-\infty}^{t} 6_x(x,\tau)\frac{\partial \epsilon_x(x,\tau)}{\partial \tau}\, d\tau \qquad (85b)$$

$$\dot{SE} = 2\frac{d}{dt}\int_0^{a(t)} \gamma_a dx = 2\gamma_a \dot{a}(t) \qquad (85c)$$

In Equations 85 h is the depth of the beam, the dot denotes differentiation with respect to time and γ_a is considered to be constant with respect to time. Also it should be noted in Equations 85a and 85b that it is necessary to integrate with respect to time and debond area or beam volume first and then differentiate with respect to time to take into account the change in debond area and beam volume with time. Substituting from Equation 82a into Equation 85a results in the following expression for the power input at the boundaries

-67-

$$\dot{I} = \frac{1}{12I_y} \frac{d}{dt} \int_0^{a(t)} dx \int_{-\infty}^{t} q(\tau)\frac{\partial}{\partial\tau} \left\{[x^2 - a^2(\tau)]^2 L^{-1}(\tau)\right\} d\tau$$

$$= \frac{1}{12I_y} \dot{a}(t) \int_{-\infty}^{t} q(\tau) \frac{\partial}{\partial\tau} \left\{[a^2(t) - a^2(\tau)]^2 L^{-1}(\tau)\right\} d\tau$$

<div align="right">(86)</div>

$$+ \frac{1}{12I_y} q(t) \int_0^{a(t)} \frac{\partial}{\partial t} \left\{[x^2 - a^2(t)]^2 L^{-1}(t)\right\} dx$$

$$= \frac{2}{9I_y} q(t) a^4(t) \dot{a}(t) L^{-1}(t) + \frac{2}{45I_y} q(t) a^5(t) \frac{\partial^{-1}(t)}{\partial t}$$

$$- \frac{\dot{a}(t)}{12I_y} \int_{-\infty}^{t} \frac{\partial q(\tau)}{\partial\tau} [a^2(t) - a^2(\tau)]^2 L^{-1}(\tau) d\tau$$

Similarly, substituting Equations (82b, c) into equation (85b) results in

$$\dot{F} + 2D = \frac{1}{18I_y} \frac{d}{dt} \int_0^{a(t)} dx \int_{-\infty}^{t} q(\tau)[3x^2 - a^2(\tau)] \frac{\partial}{\partial\tau} \left\{[3x^2 - a^2(\tau)]L^{-1}(\tau)\right\} d\tau$$

$$= \frac{1}{18I_y} \dot{a}(t) \int_{\infty}^{t} q(\tau)[3a^2(t) - a^2(\tau)] \frac{\partial}{\partial\tau} \left\{[3a^2(t) - a^2(\tau)]L^{-1}(\tau)\right\} d\tau$$

<div align="right">(87)</div>

$$+ \frac{1}{18I_y} q(t) \int_0^{a(t)} [3x^2 - a^2(t)] \frac{\partial}{\partial t} \left\{[3x^2 - a^2(t)]L^{-1}(t)\right\} dx$$

$$= \frac{2}{9I_y} q(t) a^4(t) \dot{a}(t) L^{-1}(t) + \frac{2}{45I_y} q(t) a^5(t) \frac{\partial L^{-1}(t)}{\partial t}$$

$$- \frac{1}{18I_y} \dot{a}(t) \int_{-\infty}^{t} \frac{\partial}{\partial\tau} \left\{q(\tau)[3a^2(t) - a^2(\tau)]\right\} [3a^2(t) - a^2(\tau)]L^{-1}(\tau) d\tau$$

It is now a simple matter to substitute the appropriate expressions into
the power balance equation (84) to obtain

$$\dot{a}(t) \left[2 \int_{-\infty}^{t} [3a^2(t) - a^2(\tau)] L^{-1}(\tau) \frac{\partial}{\partial \tau} \left\{ q(\tau) [3a^2(t) - a^2(\tau)] \right\} d\tau \right.$$

$$\left. - 3 \int_{-\infty}^{t} \frac{\partial q(\tau)}{\partial \tau} [a^2(t) - a^2(\tau)]^2 L^{-1}(\tau) d\tau - 72 I_y \gamma_a \right] = 0 \qquad (88)$$

where $L^{-1}(t)$ is given by equation (83). Equation (88) is obviously satisfied if the crack does not run, i.e., if $\dot{a}(t) = 0$. However, setting the bracketed term equal to zero results in an integral relation for $a(t)$ which yields yet another solution. This solution is the time history of the debond growth.

The time required to initiate debonding of the beam for a particular loading $q(t)$ can be obtained from equation (88) by noting that at the time of initiation $a(t) = a_0$. Setting the bracketed term in equation (88) equal to zero and $a(t)$ and $a(\tau)$ in the integrals equal to a_0, results in the expression

$$\int_{-\infty}^{t} L^{-1}(\tau) \frac{\partial q(\tau)}{\partial \tau} d\tau = \frac{9 I_y \gamma_a}{a_0^4} \qquad (89)$$

where again $L^{-1}(\tau)$ is given by equation (83). Solving equation (89) for t yields the time to initiation of debonding as a function of the load $q(t)$ the initial debond length a_0, the material properties and beam geometry, and the energy necessary to create new adhesive fracture surface γ_a.

It is of interest to evaluate equations (88) and (89) for two particular loadings, namely a pressure applied as a step-function in time and a pressure applied linearly with time.

Step-Applied Pressure, $q(t) = q_0 H(t)$:

The substitution of $q(t) = q_0 H(t)$ into equation (83) results in

$$L^{-1}(t) = q_0 D_{crp}(t) \qquad (90)$$

-69-

Substitution of this expression into equation (89) then gives

$$q_0^2 \int_{-\infty}^{t} D_{crp}(\tau)\,\delta(\tau)d\tau = \frac{9I_y\,\gamma_a}{a_0^4} \tag{91}$$

where $\delta(\tau)$ is the Dirac delta function. The sifting property of the delta function and the fact that $D_{crp}(\tau) \equiv 0$ for $\tau < 0$ results in the reduction of equation (91) to

$$q_0^2 = \frac{18I_y\,\gamma_a}{a_0^4\,D_g} \tag{92}$$

for all $t > 0$. Thus, one deduces that debonding is initiated instantly, that is, at $t = 0$, if q_0 is greater than or equal to the q_0 defined by equation (92). If this is the case, then the time-history of the debond for $t > 0$ can be found from equation (88). Substituting the appropriate expressions into this equation and setting the bracketed term equal to zero yields, after a series of manipulations, an integral equation from which one can solve for $a(t)$ for $t > 0$. This integral equation is given by

$$D_g\left\{ 2[3a^2(t) - a_0^2]^2 - 3[a^2(t) - a_0^2]^2 \right\}$$
$$- 8 \int_0^t D_{crp}(\tau)[3a^2(t) - a^2(\tau)]a(\tau)\dot{a}(\tau)d\tau = \frac{144I_y\,\gamma_a}{q_0^2} \tag{93}$$

Since what is of primary interest is the initial velocity of propagation of the debond, equation (93) is differentiated twice with respect to time to arrive at

$$\frac{\dot{a}(t)}{a(t)} = \frac{2\,\dot{D}_{crp}(t)}{15D_g - 10D_{crp}(t)} \tag{94}$$

where it has been assumed that $a(t)$ and $\dot{a}(t)$ are both nonzero quantities for $t > 0$. Thus, since debonding is initiated at $t = 0$, the

-70-

initial velocity of propagation is given by

$$\frac{\dot{a}(0^+)}{a_0} = \frac{2\dot{D}_{crp}(0^+)}{5D_g} \tag{95}$$

Thus, it is seen that the simple beam model proposed does not predict a smooth transition during the acceleration from zero debond velocity at $t = 0^-$ to the initial debond velocity at $t = 0^+$. Also it is noted that Equation 94 is not entirely satisfactory since for larger times the velocity of propagation of the debond could become negative for certain materials.

Constant Pressure Rate, $q(t) = q_0 tH(t)$

Substituting $q(t) = q_0 tH(t)$ into Equation 83 leads to the result

$$L^{-1}(t) = q_0 D_{crp}^{(1)}(t) \tag{96}$$

where

$$D_{crp}^{(1)}(t) = \int_0^t D_{crp}(\tau)d\tau \tag{97}$$

Using Equation 96 with Equation 89, the time to the initiation of debonding can be found by solving the equation

$$D_{crp}^{(2)}(t) = \frac{9I_y \gamma_a}{q_0^2 a_0^4} \tag{98}$$

where

$$D_{crp}^{(2)}(t) = \int_0^t \int_0^\tau D_{crp}(\zeta)d\zeta \, d\tau \tag{99}$$

Letting the solution of Equation 98 be given by $t = t_f$, the time-history of the debond for $t > t_f$ can be found from Equation 88. Substitution of $q(t) = q_0 tH(t)$ and Equation 96 into Equation 88 and subsequent

manipulations leads to the following integral equation for $a(t)$:

$$\int_0^t \left\{ 2[3a^2(t) - a^2(\tau)]^2 - 3[a^2(t) - a^2(\tau)]^2 \right\} D_{crp}^{(1)}(\tau)d\tau$$

$$- 4 \int_0^t [3a^2(t) - a^2(\tau)]\tau a(\tau)\dot{a}(\tau) \, D_{crp}^{(1)}(\tau) \, d\tau = \frac{72 I_y \gamma_a}{q_0^2} \qquad (100)$$

In arriving at Equation 100 which is true for $t > t_f$, the brackets in Equation (88) were set equal to zero since for $t > t_f$, $\dot{a}(t) \neq 0$. Differentiating Equation 100 with respect to time and dividing through by $a(t)$ results in the equation

$$2D_{crp}^{(1)}(t) \, a^2(t)[a(t) - t\dot{a}(t)]$$

$$+ \dot{a}(t)\int_0^t \left\{ 6[3a^2(t) - a^2(\tau)] - 3[a^2(t) - a^2(\tau)] \right\} D_{crp}^{(1)}(\tau)d\tau$$

$$\qquad (101)$$

$$- 6\dot{a}(t) \int_0^t \tau D_{crp}^{(1)}(\tau) \, a(\tau)\dot{a}(\tau)d\tau = 0$$

which upon taking the limit $t \to t_f^+$ yields

$$\frac{\dot{a}(t_f^+)}{a_0} = \frac{D_{crp}^{(1)}(t_f)}{t_f D_{crp}^{(1)}(t_f) - 6D_{crp}^{(2)}(t_f)} \qquad (102)$$

Again, it is seen that the simple beam model does not predict a smooth transition during the acceleration from zero debond velocity at $t = t_f^-$ to the initial debond velocity at $t = t_f^+$. Also, if times to failure are short, Equation 102 may predict negative initial debond velocities whereas it is clear that these values must be positive. For example, taking the limiting case of a glassy material, the time to the initiation of debonding is given by

$$t_f^2 = \frac{18 I_y \gamma_a}{q_0^2 a_0^4 D_g} \qquad (103)$$

-72-

while the initial velocity of propagation of the debond becomes

$$\frac{\dot{a}(t_f)}{a_0} = \frac{q_0 a_0^2}{6} \sqrt{\frac{D_g}{2I_y \gamma_a}} \qquad (104)$$

The rather unsatisfactory nature of the results obtained for the model of a simple beam in which inertia effects have been neglected, has led to the consideration of a model which includes the rate of change of the kinetic energy in the power balance. The analysis of this model is now proceeding. It is thought this will lead to more satisfactory results as it has in the case of the spherical flaw model.

V. ESTIMATES OF TIME TO FAILURE AND INITIAL
PROPAGATION VELOCITIES IN BURNING FLAWS

In order to obtain first order estimates of the time to failure and
initial crack velocity for a burning flaw in a propellant grain, it has
been necessary to depend on existing models for spherical flaws with
slight modifications. For the case of the time to failure, it was assumed
that the increase in radius of a spherical flaw due to burning was linear
in time. This essentially limited the analysis to problems in which the
average pressure in the spherical flaw remains constant. A constant
pressure, as discussed in Section III, is not realistic unless the time
to failure is quite small since the burning out of a flaw decreases the
pressure an order of magnitude in less than 500 milliseconds for typical
flaw geometries and propellants. The analysis to determine initial pro-
pagation velocities are also subject to the assumption of constant pressure.
Discussion of the time to failure and initial velocity are given in
the following sections.

FAILURE TIME FOR BURNING SPHERICAL FLAWS IN PROPELLANT GRAINS

The criticality of a burning spherical flaw is considered. A solu-
tion is obtained by use of Griffith's [15] crack criterion modified for
a linearly increasing radius. The increase in radius is assumed to be
due to burning of the material. The analysis considers the time to failure
assuming that the pressure in the flaw remains constant. This analysis
results from a modification of Griffith's crack criteria by Williams [37]
to include the effects of different geometries and viscoelasticity.
Stated mathematically this modified criteria is

$$a = \frac{K^2 \, E_{rel}(t) \, \gamma_c(t)}{P_c^2}$$

where

a	=	size of critical flaw, i.e., radius for spherical flaw
K	=	geometry factor, i.e., $K = 1.27$ for spherical flaw
$E_{rel}(t)$	=	relaxation modulus, which for a viscoelastic material is a function of time.
$\gamma_c(t)$	=	surface compliance energy, which is also a function of time.
P_c	=	internal pressure

The variation of both $E_{rel}(t)$ and $\gamma_c(t)$ with time can be approximated by relations of the form

$$E_{rel}(t) \doteq Bt^{\gamma} \tag{106}$$

$$\gamma_c(t) \doteq \delta t^{\phi} \tag{107}$$

where B, δ, γ, and ϕ are constants to be determined empirically.

If erosive burning is neglected, the combustion rate, r, of a solid propellant may be assumed to follow the empirical relation

$$r = CP_c^{\alpha} \tag{108}$$

where r is the recession rate of the burning wall and C and α are constants to be determined empirically for a particular fuel. From Equation 108 it can be seen that the assumption of constant burning rate is equivalent to assuming the pressure, P_c, is also constant.

From Equation 108 one can also determine the radius, a, of a flaw at time t, assuming linear burning, as

$$a = a_0 + CP_c^{\alpha}t \tag{109}$$

where a_0 is the initial flaw size at time $t = 0$.

The flaw size, a, can now be eliminated between Equations 105 and 108 to obtain the final result

-75-

$$a_o + CP_c^\alpha t = \frac{K^2 E_{rel}(t) \gamma_c(t)}{P_c^2} \tag{110}$$

Equation 110 may be solved interatively for t by use of Equations 106 and 107 at a given pressure P_c and initial flaw size a_o. Figure 31 is a plot of time to failure versus initial flaw size at various pressures for TP-H1011 propellant.

As can be seen from the attached figure, for all pressures investigated, there occurs rapid propagation to fracture.

INITIAL PROPAGATION VELOCITIES FOR BURNING SPHERICAL FLAWS IN PROPELLANT GRAINS

In the preceding section, we considered the time to the initiation of fracture of a burning spherical flaw. This time, t_o, was plotted versus the initial flow radius, a_o, for several different pressures in the flaw. Again using Williams' [2,19] model of a spherical flaw, the fracture propagation velocity at the instant fracture takes place can be given as a function of the time to failure. This result is

$$\frac{\dot{a}(t_o)}{a_o} = \left(\frac{1}{5t_o}\right) \left(\frac{t_o^{-1} E_{rel}^{(1)}(t_o)}{t_o^{-2} E_{rel}^{(2)}(t_o)}\right) \tag{111}$$

where

$$E_{rel}^{(1)}(t) = \int_0^t E_{rel}(\tau)d\tau \tag{111a}$$

$$E_{rel}^{(2)}(t) = \int_0^t \int_0^\tau E_{rel}(\xi)\,d\xi\,d\tau \tag{111b}$$

Thus, picking the time to failure, t_o, for a particular initial flaw radius, a_o, from the graph in Figure 31, this value of t_o may be used in Equation 111 to obtain the initial fracture velocity $\dot{a}(t_o)$. The results are shown in Figure 32, where a graph of the initial fracture velocity versus the initial flaw size is plotted for two different internal pressures. In Figure 32 are also shown the initial flaw sizes for the two pressures at which the initial fracture velocity exceeds the burning rates. For initial flaw radii greater than these values, fracture is predicted.
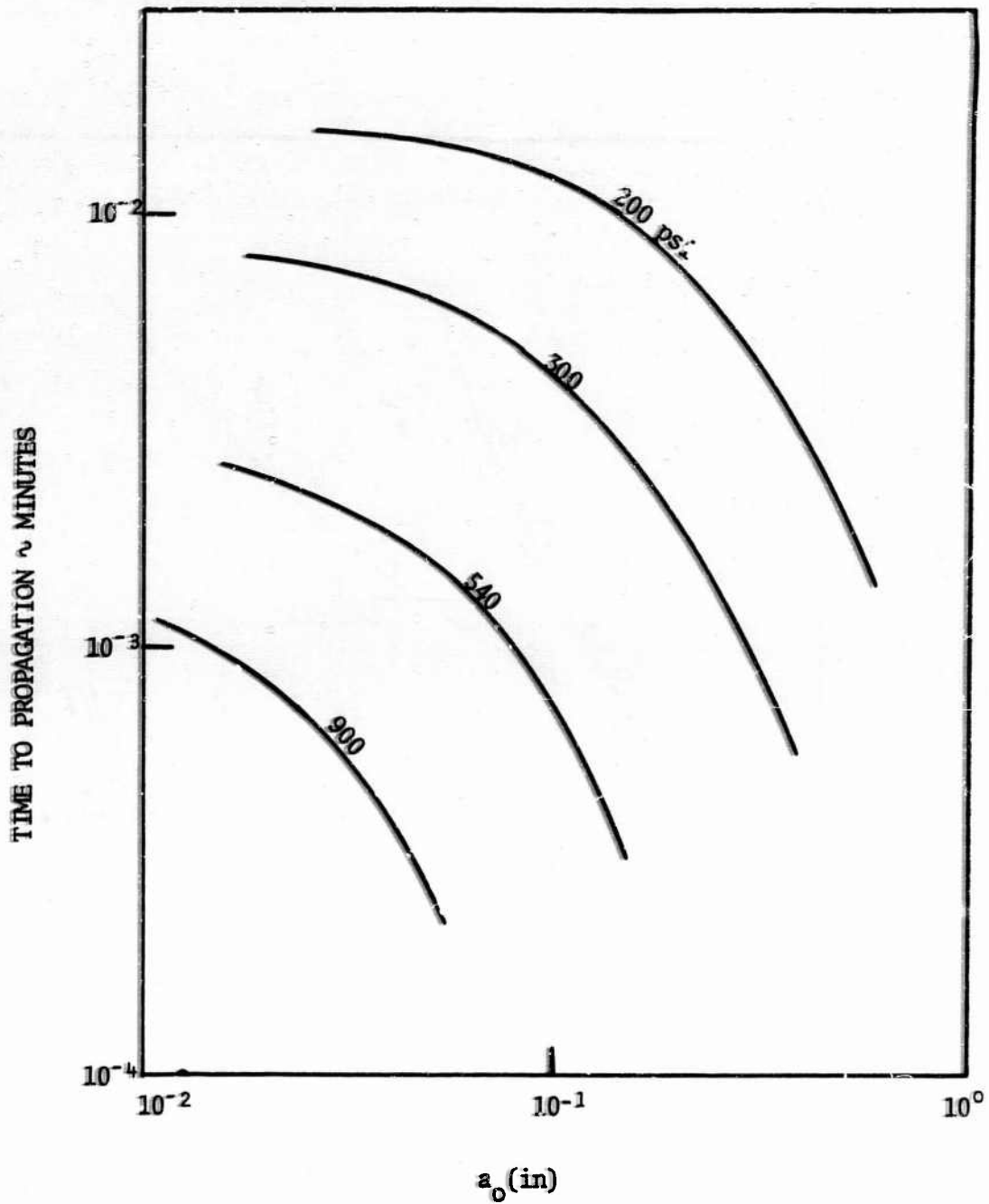
Figure 31 Time to failure versus initial flaw size
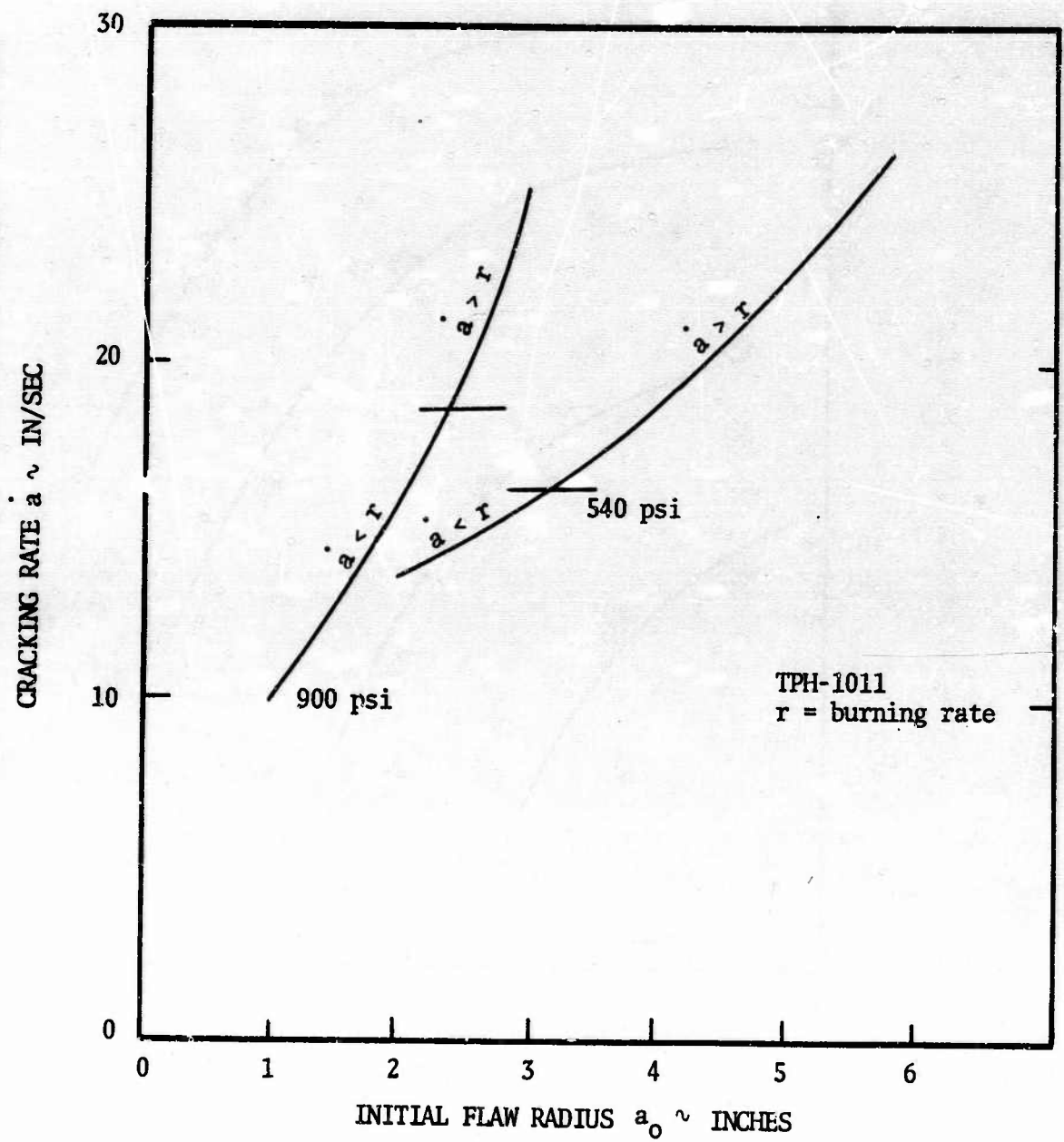
Figure 32 Cracking rate versus initial flaw radius for two pressures

VI. CONCLUSIONS

The results of this study have indicated that extremely high pressures will occur in burning flaws in solid propellant grains. The smaller the ratio of exit flow area to burning surface area, the larger the pressure. Thus, cracks and debonds not detectable by casual visual observation are most likely to propagate and lead to rocket motor failure. The flaws detectable by visual observation will be of equal concern only if they are deep. Debonds such as those occurring in the Polaris A-3 [36] head-end offer some experimental verification of these conclusions. Debonds easily detectable by ultrasonics did not cause motor failure; however, on some motors without detectable flaws failure occurred. The experimental data showed both case burn through and increased specific impulse which could be correlated with the additional burning surface and increased burning rate that would occur in a burning debond.

Typically the critical time for crack propagation is 500 milliseconds. By this time the flaw has burned out sufficiently that the overpressure has dropped by an order of magnitude. Thus, if the crack has not propagated in the first 500 milliseconds, it is doubtful that it ever will.

Limited work was accomplished to determine crack propagation velocities. However, utilization of a spherical flaw model provided an estimate of the initial propagation velocity. This estimate indicated that situations could clearly develop where the propagation velocity exceeded the burning rate in a flaw.

REFERENCES

1. United Tech. Center, "Development of Non-destructive Testing Techniques for Large Solid Propellant Rocket Motors," Contractor Report No. UTC 2015-FR, Air Force Contract AFO 4(611)-8018. Final Report. April 1963.

2. Magnussen, E., (Thiokol Chemical Corporation) "Radiographic Analysis of Defects in Solid Propellant Motors," Proceedings of BuWeps Missile and Rocket Symposium, NAD Concord. April 1961.

3. Hsiao, C. C. and Moghe, S. R., "Stress Field and Fracturing of Solid Propellants during Rocket Firing," AIAA Journal. 1. August 1963.

4. Chappell, R. N., Jensen, F. R. and Burton, R. W., "Statistical Service Life Prediction: Minuteman Third Stage Propellant Grain," AIAA Journal of Spacecraft and Rockets. 5. In No. k. January 1968.

5. Payne, C. L., "Flame Propagation in Propellant Cracks," AFRPL-TR-69-66, Air Force Rocket Propulsion Laboratory. 1969.

6. Personal Communication with John Bennett, Thiokol Chemical Corporation, Utah Division, Brigham City, Utah.

7. Personal Communication with Stan Browning, Hercules Incorporated, Magna, Utah.

8. Godai, T., "Flame Propagation into the Crack of Solid Propellant Grain," AIAA Paper No. 69-561, AIAA 5th Propulsion Specialist Conference. June 1969.

9. Personal Communication with Graham Pierson, Scientific Attache, British Embassy, Washington, D. C.

10. Prentice, J. L., "Flashdown in Solid Propellants," NAVWEPS Report 7964, NOTS TP 3009, China Lake, California. December 1962.

11. Unpublished work conducted under Project THEMIS by H. R. Jacobs at the University of Utah, UTEC-TH 69-075. August 1969.

12. Gross, J. F., Hartnett, J. P., et al, "A Review of Binary Boundary Layer Characteristics," The Rand Corporation, RM 2516. June 1959.

13. Price, E. W., "One-Dimensional Steady Flow with Mass Addition and the Effects of Combustion Chamber Flow on Rocket Thrust," Jet Propulsion. February 1955.

14. Shapiro, A. H., "The Dynamics and Thermodynamics of Compressible Fluid Flow," Vol. I, Chapter 8, New York. The Ronald Press Company. 1953.

15. Griffith, A. A., "The Phenomena of Rupture and Flow in Solids," *Philosophical Transactions of the Royal Society (London)*. A221. 1921.

16. Swanson, S. R., "Crack Propagation in Solid Rocket Propellant Grains Under Ignition Loading." Unpublished Master's Degree Thesis, University of Utah, Salt Lake City, Utah. 1968.

17. Paris, P. C. and Sih, G. C., "Stress Analysis of Cracks," *Fracture Toughness Testing and Its Applications, ASTM STP No. 381.* 1965.

18. Schapery, R. A., "Approximate Methods of Transform Inversion for Viscoelastic Stress Analysis," *Proceedings of the Fourth United States National Congress of Applied Mechanics.* 2. 1965.

19. Williams, M. L., "Initiation and Growth of Viscoelastic Fracture," *International Journal of Fracture Mechanics.* 1. 1965.

20. Sneddon, I. N., "The Distribution of Stress in the Neighborhood of A Crack in an Elastic Solid," *Proceedings of the Royal Society (London).* A187. 1946.

21. Williams, M. L., "The Kinetic Energy Contribution to Fracture Propagation in a Linearly Viscoelastic Material," *International Journal of Fracture Mechanics.* 4. 1968.

22. Williams, M. L., "The Continuum Interpretation for Fracture and Adhesion," *Journal of Applied Polymer Science.* 13. 1969.

23. Williams, M. L., "The Stresses Around a Fault or Crack in Dissimilar Media," *Bulletin of the Seismological Society of America.* 49. 1959.

24. Erdogan, F., "Stress Distribution in Bonded Dissimilar Materials with Cracks," *Journal of Applied Mechanics.* 32. 1965.

25. Jones, W. B., "A Simple Test for Certain Cases of Adhesion," University of Utah, *College of Engineering Report No. UTEC DO-69-088.* 1969.

26. Dannenburg, H., "Measurement of Adhesion by a Blister Method," *Journal of Applied Polymer Science.* 5. 1961.

27. Malyshev, B. M. and Salganik, R. L., "The Strength of Adhesive Joints Using the Theory of Cracks," *International Journal of Fracture Mechanics.* 1. 1965.

28. England, A. H., "A Crack Between Dissimilar Media," *Journal of Applied Mechanics.* 32. 1965.

29. Jones, W. B., "Cohesive and Adhesive Polymer Fracture Investigation." Unpublished Ph.D. dissertation, University of Utah, Salt Lake City, Utah. 1970.

30. Williams, M. L., "The Fracture Threshold for an Adhesive Interlayer," Journal of Applied Polymer Science. 14. 1970.

31. Berger, H. M., "A New Approach to the Analysis of Large Deflection of Plates," Journal of Applied Mechanics. 22. 1955.

32. Burton, J. D., Jones, W. B. and Williams, M. L., "Theoretical and Experimental Treatment of Fracture in an Adhesive Interlayer," University of Utah, College of Engineering Report No. UTEC DO-69-143. 1969.

33. Bennett, S. J., Anderson, G. P. and Williams, M. L., "The Time Dependence of Surface Energy on Cohesive Fracture," Journal of Applied Polymer Science. 14. 1970.

34. Erdogan, F., "Crack-Propagation Theories," Fracture. 2. New York Academic Press. 1968.

35. Sokolnikoff, I. S., Mathematical Theory of Elasticity. New York McGraw-Hill Book Company, Inc. 1956.

36. Personal Communication with Mr. Vern Orr, Lockheed Missile and Space Systems Division, Sunnyvale, California.

37. Williams, M. L. and Schapery, R. A., "Spherical Flaw Instability in Hydrostatic Tension," International Journal of Fracture Mechanics. 1. pp. 64-73. March 1965.

38. Williams, M. L., "On the Stress Distribution at the Base of a Stationary Crack." Journal of Applied Mechanics. 24. 1957,

39. Muskhelishvili, N. I., Some Basic Problems of the Mathematical Theory of Elasticity. P. Noordhoff, Groningen, The Netherlands. 1954.

APPENDIX A

NUMERICAL SOLUTION

The simultaneous solution of Equation 19 and Equation 23 can be approximated numerically. Equation 19 is of the form

$$\bar{P}' = F(\bar{P}, \eta, y) \tag{A-1}$$

and is amenable to approximation by the simple marching method which assumes that the derivative is constant for small changes of the independent variable. With this approximation one can write:

$$\bar{P}_{i+1} = \bar{P}_i + \Delta x \, \bar{P}' \Big|_{\bar{P}_i, \, \eta_i, \, y_i} \tag{A-2}$$

where Δx equals the step size. $\bar{P}$ can be determined at each step by using values determined at the previous step. The only variable which is unknown is η and it can be approximated by numerical integration if $\bar{P}$ is considered to be approximately a constant equal to its average value over the short interval Δx in which case one has for each of the three η integral equations

$$\eta_i = \frac{\eta_0}{y_i} \left(\frac{\Delta x}{2^n} \sum_{j=1}^{i-1} 2(\bar{P}_j + \bar{P}_{j+1})^n + y_0 \right) . \tag{A-3a}$$

$$\eta_i = \frac{\eta_0}{y_i} \left(\frac{\Delta x}{2^n} \sum_{j=1}^{i-1} (\bar{P}_j + \bar{P}_{j+1})^n + y_0 \right) \tag{A-3b}$$

$$\eta_i = \frac{\eta_0}{(r_0 - x_i)y_i} \left(\frac{\Delta x}{2^n} \sum_{j=1}^{i-1} (\bar{P}_j + \bar{P}_{j+1})^n (r_0 - \Delta x + \frac{\Delta x}{2}) + r_0 y_0 \right) \tag{A-3c}$$

Computation is initiated by computing $\bar{P}_2$ from Equation A-1 with $\bar{P}_1'$ determined from Equation 25, 26, or 27 for the geometry under consideration with

A-1

$\bar{P}_1 = 1$, $n_1 = n_0 = DCP_0^{n-1}$ and $y_1 = y_0$ (a function of the given geometry). n_2 is then computed from Equation A-3a, A-3b, or A-3c for the appropriate geometry using $\bar{P}_1$ and the newly computed $\bar{P}_2$. With n_2 now determined, $\bar{P}_3$ is computed and so on. With $\bar{P}_i$ and n_i known at each step and y_i given, other significant parameters of the flow may be determined such as the Mach number and the burning rate.

In a given situation the material properties, flaw geometry and chamber pressure will be known. From these known parameters an initial guess at P_0 is made and the resulting P_e and M_e are determined. If the flow is choked, P_0 is increased and M_e recalculated, this iteration is continued until $M_e = 1.0$. If the flow is not choked, P_0 is corrected and P_e is re-calculated; this iteration continued until $P_e = P_{ch}$.

The difficult portion of the numerical solution lies then in determining an iterative scheme that converges rapidly to the correct P_0. That the iterations converge rapidly is paramount since each guess at P_0 requires that at each step P_i, n_i and M_i be recalculated until P_e and/or M_e satisfy the required boundary condition. In a typical application the number of steps will vary from 100 to 1,000 depending upon the depth of the flaw and the accuracy required. Appendix B contains a complete listing of the computer program and a description of the iterative scheme used.

Because the solution is expressed in terms of the pressure at small discrete steps, it is an easy matter to allow for change in geometry due to burning. This is accomplished as follows:

1. A pressure distribution is determined for the given initial geometry and matched to the boundary conditions as described above.

2. A small-time interval Δt is determined such that the pressure distribution may be considered approximately constant over Δt. A reasonable Δt is the time that it takes y_0 to increase by the step size Δx.

$$\Delta t = \Delta x / r_{bo} = \Delta x / CP_0^n$$

3. For the geometries considered the new y dimension as a function of x is calculated by

$$y_i^{new} = y_i^{old} + r_{bi} \Delta t \tag{A-4}$$

4. A new pressure distribution is calculated for the new geometry and matched to the same boundary conditions as before.

It should be noted that as burning occurs, the assumption that $y' \ll 1$ is no longer valid in the region of the tip, since this region assumes the shape shown in Figure A-1 (if no cracking occurs). It is anticipated, however, that the geometry of Figure A-1 can be approximated by the dotted line.
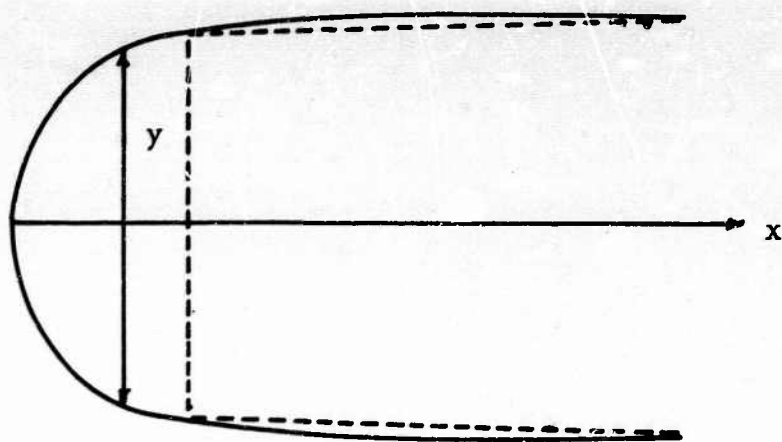
Figure A-1 Tip geometry after burning gas occurred

APPENDIX B

A complete listing of the computer program and a table relating the notation used in the analysis to that used in the program is located at the end of this appendix. Figure 1-B illustrates a simplified flow chart of the program. Notice that there are three main do-loops labeled 1, 2, and 3. Loop 3 serves to determine the number of time iterations undertaken.

Loops 1 and 2 both determine the values of the relevant parameters (i.e. $P(I)$, $V(I)$, etc.) at each $S(I)$ for a given PO. Both loops contain a series of IF statements which direct control out of the loops to a statement which determines a new PO if:

1. $P(I)$ falls below PC before $S(I) = L$.
2. $V(I)$ rises above 1.0 before $S(I) = L$.
3. $Z(I+1)$ becomes negative.

Both loops 1 and 2 are followed by a series of IF statements which determine if a correct boundary condition has been met (i.e. $P(N) = PC$ and $V(N) \leq 1$ or $P(N) > PC$ and $V(N) = 1$) and if so directs control to a PRINT statement and if not to a statement which determines a new PO. Both loops are preceded by an IF statement which determines if the maximum number of allowable iterations has been achieved and if so directs control to a PRINT statement which declares that the iteration is not converging rapidly enough.

The object of having two DO loops which are so similar is that loop 1, in general, differentiates the choked from the non-choked flows, or in other words, loop 1 attempts to match the boundary condition that $P(N) = PC$ and $V(N) \leq 1$. If the flow is either choked or marginal (i.e. "just about" choked) then loop 1 gives a "rough" approximation to PO and control then moves down to loop 2 for final adjustment.

Both the loop 1 and loop 2 PO correction statements are based on the assumption of direct proportioning, or in other words, it is assumed that if a change in PO of ΔPO. produces a change in $P(N)$ or $V(N)$ of $\Delta F(N)$, then

$$\frac{\Delta PO_2}{\Delta PO_1} = \frac{\Delta P(N)_2}{\Delta P(N)_1} = \frac{\Delta V(N)_2}{\Delta V(N)_1} \tag{B-1}$$

B-1

where $\Delta P(N)_2$ or $\Delta V(N)_2$ can be calculated by the boundary condition one is attempting to match. In reality direct proportioning of this kind is not observed and one must reduce the amount of correction ΔPO_2 by dividing it by an abritrary constant which is determined by the boundary condition being met and the size of the correction. For instance exit Mach number, $V(N)$, is more sensitive to PO change than exit pressure, $P(N)$, and therefore if one is attempting to match Mach number the direct proportion correction PO may be divided by 10.0, whereas if pressure is the attempted match the division constant may be as small as 2.0 or 3.0.

The necessary read-in for the program involves three sets of parameters; propellant, geometry, and computer. The propellant and computer parameters are listed at the beginning of the program. The geometry parameters are $Y(I)$, $YP(I)$ and $S(I)$. They may be read-in by either assigning a value of $Y(I)$ and $YP(I)$ to each value of $S(I)$ or by defining a functional relationship between $Y(I)$, $YP(I)$ and $S(I)$. In either case one must keep in mind that the program was developed assuming that $YP(I)$ is small.
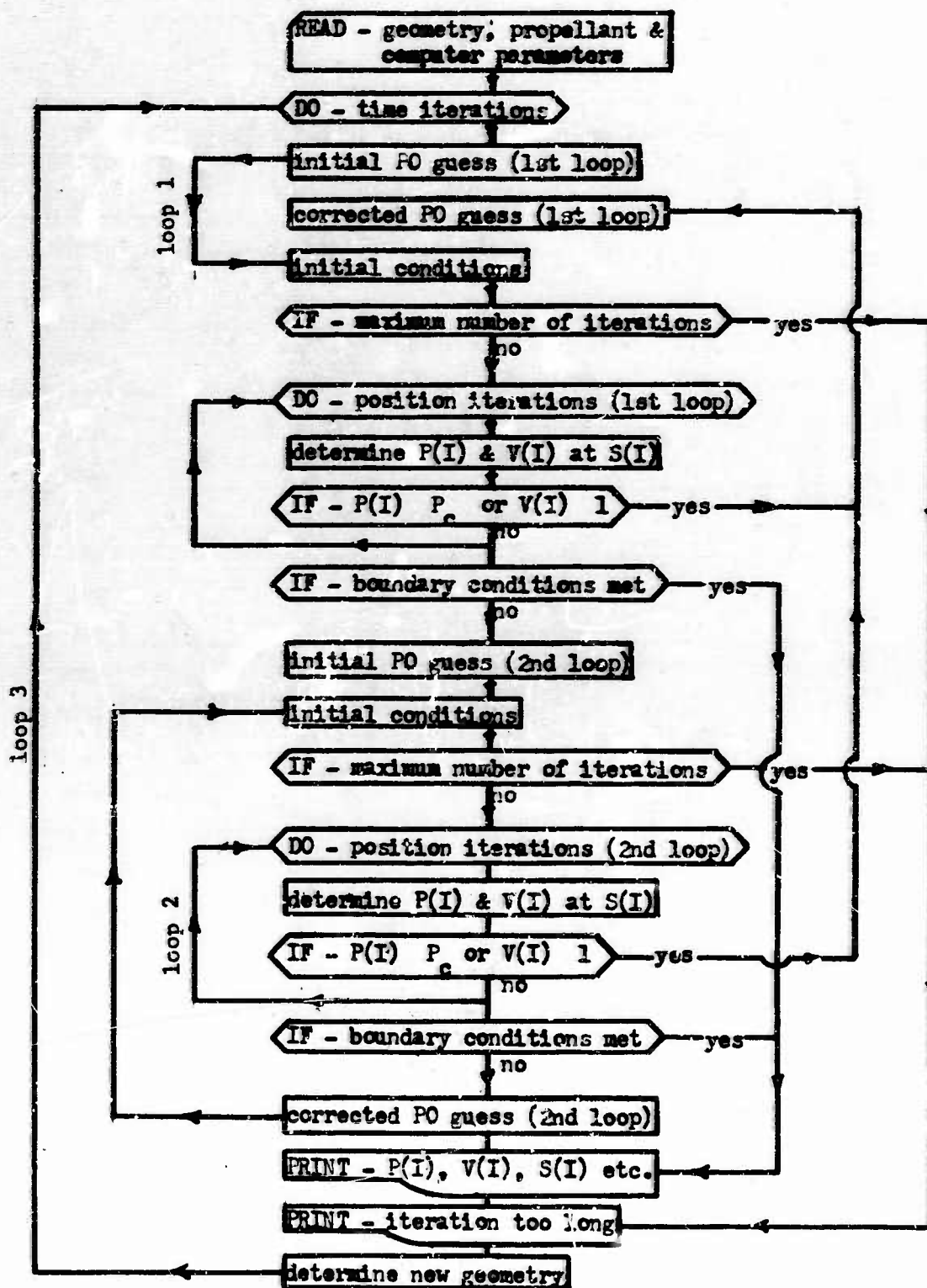
Figure 1-B   Simplified flow chart of numerical
analysis computer program

TABLE B-1

Nomenclature and Units Used in Computer Program

Analysis	Computer	Units
Br	BR(I)	none
C	C	$ft^{2n+1}/sec\text{-}lbf^n$
D	D	lbm/ft^3
f	FC	none
G^2	F	$(sec\text{-}lbf/lbm)^2$
H	HBR	none
M	V(I)	none
n	XP	none
P	P(I)	psi
P_o	PO	psi
Pch	PC	psi
$\bar{P}$	Z(I)	none
$\bar{P}'$	ZP	1/in
k	R	$ft\text{-}lbf/lbm°R$
R_e	RE(I)	none
T_o	TO	°R
Δt	DT	sec
x	S(I)	in
Δx	H	in
γ	Y(I)	in
γ'	YP(I)	none
δ	GM	none
ζ	X(I)	none
μ	U	$lbf\text{-}sec/ft^2$
η	T(I)	none
η_o	THO	none

B-4

```
            DIMENSION Y(2000),YP(2000),S(2000),Z(2000),X(2000),
          *   V(2000)
            DIMENSION P(2000),T(2000),RE(2000),BR(2000),G(2000)
            READ 47,XP,R,TO,U,C,D,GM
         47 FORMAT(10E13.5)
    C PROPELLANT PARAMETERS
    C XP=BURNING RATE EXPONENT,
    C R=GAS CONSTANT   FT LBF/LBM R
    C TO=BURNING TEMPERATURE    R
    C U=VISCOSITY   LBF SEC/FT**2
    C C=BURNING RATE COEFFICIENT   FT**(2XP+1)/SEC LBF**XP
    C D=PROPELLANT DENSITY  LBM/FT**3
    C GM=RATIO OF SPECIFIC HEATS
            READ 48, DIF,ERROR,H,L,MAX,M,N,NA
         48 FORMAT(3E10.5,5I10)
    C COMPUTER PARAMETERS
    C DIF=ALLOWABLE ERROR BETWEEN ACTUAL MACH NO AND MACH 1.0
    C ERROR=ERROR IN PRESSURE BETWEEN CHAMBER AND EXIT
    C H=STEP SIZE IN INCHES
    C L=NO OF STEPS PRINTED IE PRINT EVERY L TH STEP
    C MAX=MAXIMUM NO OF ITERATIONS ALLOWED
    C M=NO OF TIME INCREMENTS TAKEN
    C N=NO OF STEPS TAKEN
    C NA=NO OF STEPS PRINTED - IE NA STEPS
    C INITIALIZE TIME STEP
            DT = 0.
    C THIS LOOP DOES THE TIME STEPS
            DO 34 J = 1, M
    C INITIALIZE ITERATION COUNTER
            NI = 1
    C INITIAL PO GUESS
            PO=PC+1.
            PORS =PC
            SR=0.
            GO TO 26
         24 CONTINUE
            DPOS=PO-PORS
            DS =S(I)-SR
            IF(DS)100,101,100
        101 DS=H
        100 CONTINUE
            SR=S(I)
            PORS=PO
            IF(NI-6)54,54,53
         54 SDIV=2.5
            GO TO 57
         53 SDIV=1.
         57 CONTINUE
    C CORRECTED PO GUESS
            PO=PORS+(DPOS/SDIV)*(S(N)-SR)/DS
         26 CONTINUE
```

B-5

```
      B = U.
      THO = D*C*(PO*144.)**(XP-1.)
      T(1) = D*C*(PO*144.) **(XP-1.).
      Z (1) = 1.
      F= (2.*(GM-1.) * TO * R)/(GM * 32.2)
C UPGRADE ITERATION COUNTER
      NI = NI+1
C CHECK IF MAX ITERATIONS HAVE BEEN REACHED
      IF(NI-MAX)58,58,29
   58 CONTINUE
C THIS LOOP DETERMINES V(I) AND P(I) AT EACH STEP
      DO 35  I = 1, N
      P(I) = PO * Z(I)
      IF(I-N)50,22,22
   50 CONTINUE
C EXIT LOOP IF P(I) FALLS BELOW PC
      IF(P(I)+ERROR-PC)24,22,22
   22 CONTINUE
      X(I)=SQRT(Z(I)*Z(I)+F*T(I)*T(I))
      V(I)=(X(I)-Z(I))/(Z(I)*(GM-1.))
      IF(I-N)51,23,23
   51 CONTINUE
C EXIT LOOP IF V(I) RISES ABOVE 1.0
      IF(V(I)-1.)23,24,24
   23 CONTINUE
      RE(I)=(Y(I)*T(I)*PO*24.)/(U*32.2)
C CHECK IF FLOW IS TURBULENT OF LAMINAR
      IF (RE(I) - 2200.) 20, 20, 21
   20 FC = 96. / RE (I)
      GO TO 27
   21 FC = .316/ RE(I) ** .25
   27 CONTINUE
      BR(I)=THO*Z(I)**XP*SQRT(RE(I))/T(I)
   52 CONTINUE
      IF(N-1)108,108,105
  105 CONTINUE
      HBR=1./(2.*(BR(I)+1.))+1./(2.*5.**(BR(I)/4.))
      B2 = F * T(I) / X(I)
      B4 = (GM* X(I)) / ((X(I) - GM * Z(I)) * Y(I))
C USE THIS B1 CARD FOR A DEBOND
      B1=(X(I)-Z(I))*(FC*(1.+HBR)/2.+YP(I))
C USE THIS B1 CARD FOR A CRACK
      B1=(X(I)-Z(I))*(FC*HBR+YP(I))
C USE THIS B1 CARD FOR A CIRCULAR DEBOND
      B1=(X(I)-Z(I))*(FC*(1.+H)/2.+YP(I)-Y(I)/(RO-S(I)))
```

B-6

```
C USE THIS B3 CARD FOR A DEBOND
      B3=THO*Z(I)**XP-YP(I)*T(I)
C USE THIS B3 CARD FOR A CRACK
      B3=2.* THO*Z(I)**XP-YP(I)*T(I)
C USE THIS B3 CARD FOR A CIRCULAR DEBOND
      B3=THO*Z(I)**XP-YP(I)*T(I)+Y(I)*T(I)/(RO-S(I))
C USE THIS B5 CARD FOR A CIRCULAR DEBOND
      B5=Z(I)*Y(I)/(RO-S(I))*(GM-1.)/GM
C USE THIS ZP CARD FOR A DEBOND
      ZP = B4 *(B1 + B2 * B3)
C USE THIS ZP CARD FOR A CRACK
      ZP = B4 *(B1 + B2 * B3)
C USE THIS ZP CARD FOR A CIRCULAR DEBOND
      ZP=(B1+B5+B2*B3)*B4
      Z(I+1) = Z(I) + H*ZP
      IF(Z(I+1)+Z(I))24,24,25
   25 CONTINUE
C USE THIS B  CARD FOR A DEBOND
      B = (Z(I+1)+ Z(I))** XP + B
C USE THIS B  CARD FOR A CRACK
      B=2.*(Z(I)+Z(I+1))**XP +B
C USE THIS B  CARD FOR A CIRCULAR DEBOND
      B=(Z(I)+Z(I+1))**XP*(RO-H*I+H/2. )+B
C USE THIS T(I+1) CARD FOR A DEBOND
      T(I+1)=(THO/Y(I+1))*(H*B/2.**XP+YO)
C USE THIS T(I+1) CARD FOR A CRACK
      T(I+1)=(THO/Y(I+1))*(H*B/2.**XP+YO)
C USE THIS T(I+1) CARD FOR A CIRCULAR DEBOND
      T(I+1)=THO/(Y(I+1)*(RO-S(I+1)))*(H*B/(2.**XP)+Y(I)*RO)
  108 CONTINUE
      V(I)=SQRT(V(I))
   36 CONTINUE
C THE FOLLOWING 4 IF STATEMENTS DETERMINE IF A CORRECT
C      BOUNDARY
CONDITION HAS BEEN SATISFIED
      IF(V(N)-DIF-1.)60,60,59
   60 IF(P(N)+ERROR-PC)90,56,91
   91 IF(ABS(P(N)-PC)-ERROR)56,56,92
   92 IF(ABS(V(N)-1.)-DIF)56,56,93
C THIS IF STATEMENT DETERMINES WHICH BOUNDARY CONDITION TO
C          ATTEMPT
C TO MATCH
   93 IF(ABS(P(N)-PC)/PC-ABS(1.-V(N)))90,90,88
   59 DPO=PO/100.
      GO TO 89
```

```
   90 DPO=(PC-P(N))/10.
      GO TO 89
   88 DPO= PO/100.
   89 CONTINUE
C CORRECTED PO GUESS
      PO=PO+DPO
      EXDP=DPO/10.
      NV=1
      NP=1
   55 CONTINUE
      VR=V(I)
      PR=P(I)
C UPGRADE ITERATION COUNTER
      NI = NI+1
C CHECK IF MAX ITERATIONS HAVE BEEN REACHED
      IF(NI-  MAX)86,86,29
   86 CONTINUE
      B = 0.
      THO = D*C*(PO*144.)**(XP-1.)
      T(1) = D*C*(PO*144.) **(XP-1.)
      Z (1) = 1.
      F= (2.*(GM-1.) * TO * R)/(GM * 32.2)
C THIS LOOP DETERMINES V(I) AND P(I) AT EACH STEP
      DO 37 I=1,N
      P(I) = PO * Z(I)
      IF(I-N)61,62,62
   61 CONTINUE
C EXIT LOOP IF P(I) FALLS BELOW PC
      IF(P(I)+ERROR-PC)24,62,62
   62 CONTINUE
      X(I)=SQRT(Z(I)*Z(I)+F*T(I)*T(I))
      V(I)=(X(I)-Z(I))/(Z(I)*(GM-1.))
      IF(I-N)63,64,64
   63 CONTINUE
C EXIT LOOP IF V(I) RISES ABOVE 1.0
      IF(V(I)-1.)64,64,24
   64 CONTINUE
      RE(I)=(V(I)*T(I)*PO*24.)/(U*32.2)
C CHECK IF FLOW IS TURBULENT OF LAMINAR
      IF(RE(I)-2200.)65,65,66
   65 FC=96./RE(I)
      GO TO 67
   66 FC=.316/RE(I)***.25
   67 CONTINUE
      BR(I)=THO*Z(I)**XP*SQR (RE(I))/T(I)
```

B-8

```
      HBR=1./(2.*(BR(I)+1.))+1./(2.*5.**(BR(I)/4.))
      IF(N-1)106:106,107
  107 CONTINUE
      B2 = F * T(I) / X(I)
      B4 = (GM* X(I)) / ((X(I) - GM * Z(I)) * Y(I))
C USE THIS. B1 CARD FOR A DEBOND
      B1=(X(I)-Z(I))*(FC*(1.+HBR)/2.+YP(I))
C USE THIS B1 CARD FOR A CRACK
      B1=(X(I)-Z(I))*(FC*HBR+YP(I))
C USE THIS B1 CARD FOR A CIRCULAR DEBOND
      B1=(X(I)-Z(I))*(FC*(1.+H)/2.+YP(I)-Y(I)/(RO-S(I)))
C USE THIS B3 CARD FOR A DEBOND
      B3=THO*Z(I)**XP-YP(I)*T(I)
C USE THIS B3 CARD FOR A CRACK
      B3=2.* THO*Z(I)**XP-YP(I)*T(I)
C USE THIS B3 CARD FOR A CIRCULAR DEBOND
      B3=THO*Z(I)**XP-YP(I)*T(I)+Y(I)*T(I)/(RO-S(I))
C USE THIS B5 CARD FOR A CIRCULAR DEBOND
      B5=Z(I)*Y(I)/(RO-S(I))*(GM-1.)/GM
C USE THIS ZP CARD FOR A DEBOND
      ZP = B4 *(B1 + B2 * B3)
C USE THIS ZP CARD FOR A CRACK
      ZP = B4 *(B1 + B2 * B3)
C USE THIS ZP CARD FOR A CIRCULAR DEBOND
      ZP=(B1+B5+B2+B3)*B4
      Z(I+1) = Z(I) + H*ZP
      IF(Z(I+1)+Z(I))24,69,69
   69 CONTINUE
C USE THIS B  CARD FOR A DEBOND
      B = (Z(I+1)+ Z(I))** XP + B
C USE THIS B  CARD FOR A CRACK
      B=2.*(Z(I)+Z(I+1))**XP +B
C USE THIS B  CARD FOR A CIRCULAR DEBOND
      B=(Z(I)+Z(I+1))**XP*(RO-H*I+H/2. )+B
C USE THIS T(I+1) CARD FOR A DEBOND
      T(I+1)=(THO/Y(I+1))*(H*B/2.**XP+YO)
C USE THIS T(I+1) CARD FOR A CRACK
      T(I+1)=(THO/Y(I+1))*(H*B/2.**XP+YO)
C USE THIS T(I+1) CARD FOR A CIRCULAR DEBOND
      T(I+1)=THO/(Y(I+1)*(RO-S(I+1)))*(H*B/(2.**XP)+Y(I)*RO)
  106 CONTINUE
      V(I)=SQRT(V(I))
   37 CONTINUE
      DP=P(N)-PR
      DV=V(N)-VR
```

```
      DRC=ABS(P(N)-PC)/PC-ABS(1.-V(N))
C THE FOLLOWING 4 IF STATEMENTS DETERMINE IF A CORRECT
C       BOUNDARY
CONDITION HAS BEEN SATISFIED
      IF(P(N)+ERROR-PC)80,81,81
   81 IF(V(N)-DIF-1.)82,56,83
   82 IF(ABS(P(N)-PC)-ERROR)56,56,87
   87 IF(ABS(V(N)-1.)-DIF)56,56,84
C THIS IF STATEMENT DETERMINES WHICH BOUNDARY CONDITION TO
C       ATTEMPT
C TO MATCH
   84 IF(ABS(P(N)-PC)/P(N)-ABS(1.-V(N)))80,80,83
   80 CONTINUE
      NP=NP+1
      CNP=ABS(DP/EXDP )
      IF(NP-2)95,95,94
   95 PDIV=3.
      GO TO 99
   94 PDIV=CNP
   99 CONTINUE
      POR=PO-((P(N)-PC)/PDIV)*DPO/DP
      EXDP=(P(N)-PC)/PDIV
      GO TO 85
   83 CONTINUE
      NV=NV+1
      IF(NV-2)97,97,96
   96 IF(ABS(V(N)-1.)-.3)104,103,103
  104 VDIV=2.
      GO TO 98
   97 IF(ABS(V(N)-1.)-.3)102,103,103
  102 VDIV=3.
      GO TO 98
  103 VDIV=10.0
   98 CONTINUE
      POR=PO-((V(N)-1.)/VDIV)*DPO/DV
   85 CONTINUE
      DPO=POR-PO
      PO=POR
      GO TO 55
   56 CONTINUE
      DR=DR+DT
C PRINT DESIRED PARAMETERS WHICH IDENTIFY INITIAL GEOMETRY,
C       TIME ,
C PROPELLANT, AND PC
C PRINT DESIRED VARIABLES ALONG LENGTH OF FLAW IE V(I),
```

```
C         P(I), Y(I), S(I)
   29 CONTINUE
      DR=DR+DT
C PRINT DESIRED PARAMETERS WHICH IDENTIFY INITIAL GEOMETRY,
C          TIME  ,
C PROPELLANT, AND PC
      PRINT 72
   72 FORMAT(' ','ITERATION UNSTABLE')
   28 CONTINUE
      DT=H/(C*(PO*144.)**XP*12.)
C COMPUTE NEW GEOMETRY
      DO 35  I = 1,N
      Y(I)=Y(I)+H*Z(I)**XP
      Y(I)=Y(I)+H*Z(I)**XP*2.
   35 CONTINUE
      DO 38 I = 1,N
      YP(I) = (Y(I+1)-Y(I))/  H
   38 CONTINUE
   34 CONTINUE
      STOP
```

APPENDIX C

Consider the plane problem of a Griffith crack of length 2a in a thin elastic sheet. If a uniform pressure p_0 acts within the crack, the symmetric stress distribution in the vicinity of the crack tip is given by [38]

$$\sigma_r = \frac{K_1}{4\sqrt{2\pi r}}\left[5\cos\frac{\theta}{2} - \cos\frac{3\theta}{2}\right] \tag{C-1a}$$

$$\sigma_\theta = \frac{K_1}{4\sqrt{2\pi r}}\left[3\cos\frac{\theta}{2} + \cos\frac{3\theta}{2}\right] \tag{C-1b}$$

$$\tau_{r\theta} = \frac{K_1}{4\sqrt{2\pi r}}\left[\sin\frac{\theta}{2} + \sin\frac{3\theta}{2}\right] \tag{C-1c}$$

where r and θ are polar coordinates with origin at the crack tip as shown in Figure C-1, and K_1 is the mode I stress intensity factor which for this problem can be written as

$$K_1 = p_0 \sqrt{\pi a} \tag{C-2}$$

Applying the energy balance as a fracture criterion leads to the criticality condition

$$K_{1_{cr}} = p_{0_{cr}} \sqrt{\pi a} \tag{C-3}$$

This condition can be put into the more familiar but equivalent form

$$P_{0_{cr}} = \sqrt{\frac{2E\gamma}{\pi a}} \tag{C-4}$$

where γ is the cohesive fracture energy, by recognizing that the potential energy release rate with crack extension is directly related to the stress intensity factor K_1 [17].

If the pressure inside the crack were now to be distributed non-uniformly along the length of the crack, it becomes important to assess the effect of this non-uniformity upon crack instability. A convenient

C-1

way of doing so is to compare the fracture threshold for the non-uniform pressure distribution to that which would result if its total (integrated) pressure were distributed along the crack length uniformly. This comparison entails solving for the stress intensity factor for the non-uniform pressure which will be accomplished by using the Green's function obtained by the method of Muskhelishvili [39].

If two oppositely directed concentrated forces each of magnitude P act within and normal to a crack at some distance b from its center, as shown in Figure C-1, the stress intensity factor is given by [17]

$$K_1 = \frac{P}{(\pi a)^{\frac{1}{2}}} \left(\frac{a+b}{a-b}\right)^{\frac{1}{2}} \tag{C-5}$$

Recognizing that Equation (C-5) is a Green's function for the problem of a non-uniform pressure $p(x)$ applied within the crack, the stress intensity factor for this problem is easily obtained in the integral form

$$K_1 = \frac{1}{(\pi a)^{\frac{1}{2}}} \int_{-a}^{a} p(x) \left(\frac{a+x}{a-x}\right)^{\frac{1}{2}} dx \tag{C-6}$$

Approximating the pressure within the crack by

$$p(\xi) = p_0[1 - \lambda(1-\xi^2)^m] \tag{C-7}$$

where $\xi = x/a$ and λ and m are parameters chosen to best fit the actual pressure distribution, one obtains the stress intensity factor for this distribution from Equation (C-6) as

$$K_1 = \frac{p_0 a}{(\pi a)^{\frac{1}{2}}} \int_{-1}^{1} [1 - \lambda(1-\xi^2)^m] \left(\frac{1+\xi}{1-\xi}\right)^{\frac{1}{2}} d\xi$$

$$= p_0(\pi a)^{\frac{1}{2}} \left[1 - \frac{\lambda}{\pi} B\left(m + \frac{1}{2}, \frac{1}{2}\right)\right] \tag{C-8}$$

C-2

In Equation (C-8), $B(\alpha,\beta)$ is the complete Beta function. Upon expressing Equation (C-8) in terms of the average of the applied pressure $\bar{p}$, one finally obtains

$$K_1 = \bar{p}(\pi a) \left[\frac{1 - (\lambda/\pi) \; B(m + \tfrac{1}{2}, \tfrac{1}{2})}{1 - (\lambda/2) \; B(m + 1, \tfrac{1}{2})} \right] \tag{C-9}$$

where

$$\bar{p} = \frac{1}{2} \int_{-1}^{1} p(\xi) d\xi = p_0 \left[1 - \frac{\lambda}{2} B(m+1, \tfrac{1}{2}) \right] \tag{C-10}$$

Note in Equation (C-9) that if $\lambda = 0$, the uniform pressure result is recovered. Hence the term in brackets in Equation (C-9), which is graphed in Figure C-2, expresses the deviation in the stress intensity factor due to deviations of the assumed pressure (C-7) from uniformity. This deviation is expected to be typical of non-uniform pressure distributions in cracks of rather arbitrary geometry.
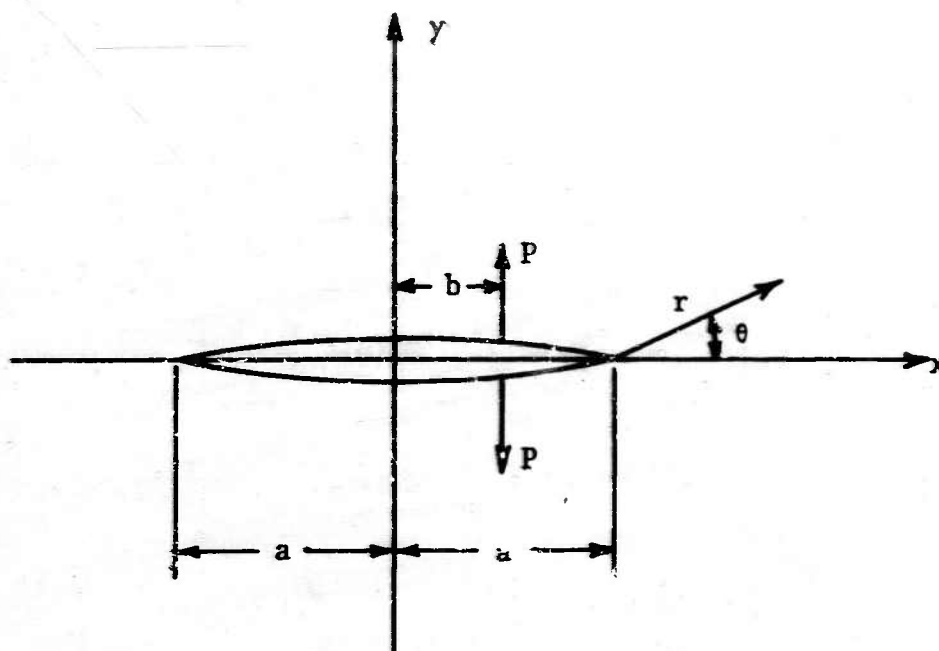
Figure C-1. Finite length crack with self-equilibrating concentrated load system applied normal to crack plane.
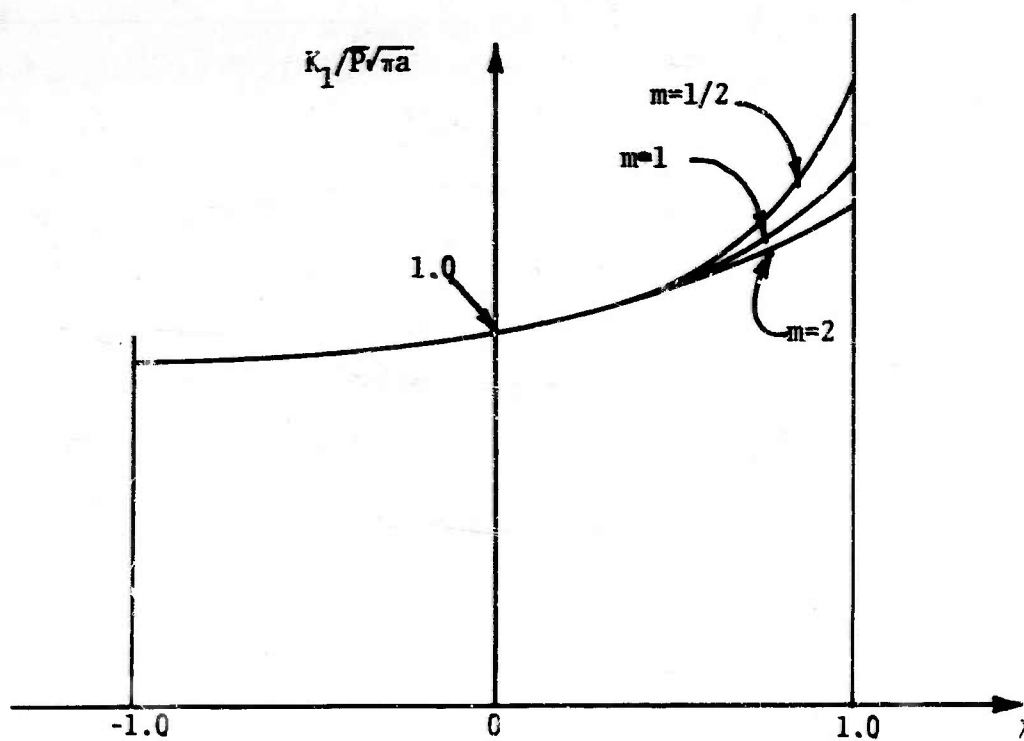

Figure C-2. Stress intensity factors for a finite crack of length 2a subjected to a non-uniform pressure along its length.

DOCUMENT CONTROL DATA - R & D

(Security classification of title, body of abstract and indexing annotation must be entered when the overall report is classified)

1. ORIGINATING ACTIVITY (Corporate author)	2a. REPORT SECURITY CLASSIFICATION
University of Utah College of Engineering Salt Lake City, Utah	
	2b. GROUP

3. REPORT TITLE

The Study of Crack Criticality in Solid Rocket Motors

4. DESCRIPTIVE NOTES (Type of report and inclusive dates)

Final Report--November 3, 1969--January 31, 1971

5. AUTHOR(S) (First name, middle initial, last name)

M. L. Williams, H. R. Jacobs

6. REPORT DATE	7a. TOTAL NO. OF PAGES	7b. NO. OF REFS
January 1971	101	39

8a. CONTRACT OR GRANT NO.	9a. ORIGINATOR'S REPORT NUMBER(S)
FO 4611-70-C-0006	UTEC DO 71-041
b. PROJECT NO.	
c.	9b. OTHER REPORT NO(S) (Any other numbers that may be assigned this report)
d.	

10. DISTRIBUTION STATEMENT

This document is subject to special export controls and each transmittal to foreign government or foreign nationals may be made only with prior approval of AFRPL (DOG/STINFO), Edwards, California 93523

11. SUPPLEMENTARY NOTES	12. SPONSORING MILITARY ACTIVITY
	AFRPL/Edwards Air Force Base, Calif.

13. ABSTRACT

Assuming that burning in cracks and debonds in solid propellant grains will occur, the present paper analyzes the pressure distributions in these flaws during the burning process. In conducting the analyses the wall burning rate is assumed to be of the form $r_b \sim P^n$. A preliminary analysis of fracture propagation is included by which estimates of initial flaw propagation velocity are made. It is shown that varieties of flaws can exist where the pressure loading within the flaw may be sufficient to cause mechanical propagation velocities in excess of the burning rate.

DD FORM 1473
1 NOV 65